Hydrometeorological application of microwave links

Measurement of evaporation and precipitation

Hidde Leijnse

Hydrometeorological application of microwave links

Measurement of evaporation and precipitation

Promotor:
    Prof. dr. ir. R. Uijlenhoet   Hoogleraar Hydrologie en
                                                 Kwantitatief Waterbeheer,
                                                 Wageningen Universiteit

Copromotor:
    Ir. J.N.M. Stricker   Voormalig universitair hoofddocent
                                             bij de leerstoelgroep Hydrologie en
                                               Kwantitatief Waterbeheer,
                                             Wageningen Universiteit

Promotiecommissie:
    Dr. G. Delrieu   LTHE Grenoble, Frankrijk
    Prof. dr. M.B. Parlange   EPF Lausanne, Zwitserland
    Dr. ir. H.W.J. Russchenberg   TU Delft
    Prof. dr. ir. S.E.A.T.M. van der Zee   Wageningen Universiteit

Hydrometeorological application of microwave links

Measurement of evaporation and precipitation

Hidde Leijnse

Abstract

Chapter 1. This thesis deals with the estimation of evaporation and precipitation using microwave links. Measurement of both of these vertical water fluxes at the land-atmosphere interface at regional scales is very important in many disciplines such as hydrology and meteorology. As the scale at which microwave links operate is the scale of interest of many applications, microwave link measurements offer a clear advantage over point-scale measurements. Other instruments have disadvantages that make their measurements potentially less accurate than those from microwave links. However, microwave links are by no means perfect. Therefore microwave links, like all other instruments, will be of most benefit if used in combination with other instruments. There is great potential for the use of microwave links from very dense existing commercial cellular communication networks, especially for the estimation of rainfall, which makes reseach on these instruments highly worthwhile and relevant.

Chapter 2. A method to estimate areal evaporation using a microwave link (radio wave scintillometer) in combination with an energy budget constraint is proposed. This Radio Wave Scintillometry-Energy Budget Method (RWS-EBM) is evaluated for its applicability in different meteorological conditions and for its sensitivity to several variables (the structure parameter of the refractive index of air, the total available energy, the wind velocity, the effective average vegetation height and the correlation coefficient between the temperature and humidity fluctuations). The method is shown to be best suited for use in wet to moderately dry conditions, where the latent heat flux is at least a third of the total available energy (i.e. Bowen ratio ≤ 2). It is important to accurately measure the total available energy and the wind velocity, as the RWS-EBM is most sensitive to these variables. The Flevoland field experiment has provided data, obtained with a 27-GHz microwave link (over 2.2 km), a Large Aperture Scintillometer (LAS, also 2.2 km) and four eddy covariance (EC) systems, which are used to test the RWS-EBM. Comparing 92 daytime measurements (30-minute intervals) of the evaporation estimated us-

ing the RWS-EBM to that determined in alternative manners (eddy covariance and two-wavelength scintillometry) leads to the conclusion that the method provides consistent estimates (coefficient of determination $r^2 = 0.85$ in both cases) under relatively wet conditions.

Chapter 3. The suitability of the same 27-GHz microwave link for measuring path-averaged precipitation is investigated. Theoretical analyses show that the specific attenuation of an electromagnetic signal at this frequency varies nearly linearly with the rainfall intensity, which is ideal for line-integrating instruments. The dependence of this relation on the drop size distribution and on the temperature is small, so that uncertainties in these variables do not play large roles in the estimation of rainfall intensity. Data from an experiment with this microwave link (now spanning 4.89 km) and a line configuration of seven tipping-bucket raingauges are used to test whether this instrument is indeed suitable for the estimation of path-averaged rainfall. Results from this experiment show that the attenuation due to wet antennas can have a significant effect on the retrieved rainfall intensity. However, when a two-parameter wet antenna correction function is applied to the link data, comparisons with the raingauge data show that the instrument is indeed well-suited for the measurement of path-averaged rainfall.

Chapter 4. There is actually an existing network of microwave links over nealy the entire land area of the world. These links are part of commercial cellular communication networks. An analysis of data from two such links (both operating at 38 GHz) collected during eight rainfall events over a two-month period (Oct.–Nov. 2003) during mostly stratiform rainfall in The Netherlands is presented. Comparisons between the time series of rainfall intensities estimated using the microwave links and those measured by a nearby rain gauge and a composite of two C-band weather radars show that the dynamics of the rain events is generally well-captured by the radio links. This shows that such links are potentially a valuable addition to existing methods of rainfall estimation, provided the uncertainties related to the reference signal level, signal level resolution, wet antenna attenuation and temporal sampling can be resolved.

Chapter 5. Besides the use of the specific attenuation of a single signal for the estimation of path-averaged rainfall, the differece in attenuation of two signals with differing frequencies and/or polarizations could also be used. Power-law relations between rainfall intensity and specific or differential attenuation have been computed using (rain)drop size distributions (DSDs) measured in The Netherlands. The optimum settings for single-frequency links in Dutch conditions are a frequency of 35.9 GHz and horizontal polarization. The influence of canting of drops is negligible when specific attenuation is used and it is very small (a few percent) when differential attenuation is used. The effect of temperature is also small for all configurations if the frequency (combination) is chosen correctly. It is shown that the power-law relations used for the estimation of rainfall should be adapted to the climatology under consideration. Link signals have been generated using measured time series of DSDs in combination with wind velocity data. Errors and uncertainties due to the variation in

DSDs are at a minimum at frequencies (and frequency combinations) where the power-law relation for the conversion to rainfall intensity is close to linear, and errors are seen to increase with link length.

Chapter 6. Issues associated with microwave link rainfall estimation such as the effects of spatial and temporal variations in rain, the nonlinearity of $R - k$ relations, temporal sampling, power resolution, and wet antenna attenuation are investigated using more than 1.5 years of data from a high-resolution X-band weather radar. Microwave link signals are generated for different link frequencies and lengths from these radar data, so that retrieved path-averaged rainfall intensities can be compared to true path-averaged values. Results of these simulations can be linked to the space-time structure of rain. A frequency-dependent relation between the rainfall intensity at an antenna and the attenuation caused by its wetting is derived using microwave link and rain gauge data. It is shown that if the correct temporal sampling strategy is chosen, the effects of the degradation of power resolution and of wet antenna attenuation (if a correction is applied) are minor (i.e., mean bias error (MBE) and bias-corrected root mean square error (RMSE) are $> -20\%$ and $< 20\%$ of the mean rainfall intensity, respectively) for link frequencies and lengths above ~ 20 GHz and ~ 2 km, respectively.

Chapter 7. It has been demonstrated that microwave links are highly suitable for the estimation of both evaporation and precipitation. A number of issues with these estimates have been identified and subsequently analyzed. Especially for the estimation of precipitation, links from commercial cellular communication networks offer great potential for operational monitoring of this water flux on a dense grid. Future work includes testing the potential of dual-frequency/polarization links under different climatological conditions, investigating the potential of commercial links for the estimation of evaporation, integrating radar and commercial link measurements to create near real-time maps of precipitation, and analyzing whether it is possible to accurately estimate path-averaged water vapor content using microwave links.

Voorwoord

In maart 2003 ben ik begonnen met mijn promotieonderzoek bij de leerstoel-groep Hydrologie en Kwantitatief Waterbeheer, waarvan Peter Troch toen nog leerstoelhouder was. Het onderzoek werd financieel gesteund door de Nederlandse Organisatie voor Wetenschappelijk Onderzoek (NWO) via de vernieuwingsimpuls beurs (016.021.003) van Remko Uijlenhoet. Zodoende was hij ook mijn directe begeleider. Na het vertrek van Peter naar Tucson is Remko leerstoelhouder geworden, waardoor het voor hem ook mogelijk werd mijn promotor te zijn. Aanvankelijk was het de bedoeling dat ik me zou richten op de de microstructuur van regen door het analyseren van hoge resolutie radar metingen. Maar door de beschikbaarheid van gegevens van microgolf straalverbindingen (Hoofdstukken 2, 3 en 4), en door de publicatie van een artikel in *Science* van Messer et al. heb ik mijn focus verlegd naar dit onderwerp. Door deze verschuiving is Han Stricker meer betrokken geraakt bij mijn begeleiding, en ik ben dan ook blij dat hij als co-promotor wil optreden. Zijn enorme kennis en ervaring, en zijn vriendelijkheid zijn zeer waardevol geweest in deze periode!

Ik heb de begeleiding van Remko als zeer plezierig ervaren. Ik heb steeds voldoende ruimte gekregen om het onderzoek zelf in te vullen, maar hij was altijd bereid om vragen te beantwoorden, mijn probeersels van commentaar te voorzien en me te sturen wanneer dat echt nodig was. Ik heb ontzettend veel van Remko geleerd in deze periode. Naast de formele contacten hecht ik veel waarde aan de persoonlijke vriendschap. Remko, bedankt voor alles!

Het werk dat is beschreven in dit proefschrift had niet gedaan kunnen worden zonder de gegevens die door verschillende mensen zijn verzameld. Het Flevoland experiment, waarvan gegevens zijn gebruikt in Hoofdstuk 2, is uitgevoerd door collega's van de leerstoelgroep Meteorologie en Luchtkwaliteit, inclusief de toenmalige gastmedewerker Wim Kohsiek (KNMI) (gefinancierd door STW, project nummer WMO4133). Met name wil ik Wouter Meijninger bedanken voor de zeer nuttige discussies over deze gegevens, het experiment en de in dit proefschrift voorgestelde methode om verdamping te schatten.

x

Contents

List of Symbols

The symbols used in this thesis are listed in the table below, along with a short description, a value (if it is constant), and units. The symbols c and c_i for $i = 1, 2, 3 \ldots$ are reserved for constants that have definitions that may vary throughout this thesis.

Symbol	Short Description	Value and Units
Γ	Gamma function	-
$\Delta L_{\mathrm{v}} E$	Error in latent heat flux	W m^{-2}
Δk	Differential attenuation	dB km^{-1}
$\Delta k_{\mathrm{X,Y}}$	Differential attenuation for signals with polarizations X and Y	dB km^{-1}
Λ	Reciprocal of mean raindrop diameter	mm^{-1}
Ψ	Businger-Dyer function	-
β	Bowen ratio	-
β_{max}	Maximum Bowen ratio	-
γ	Coefficient of $l - R$ power law	m mm$^{-\delta}$ h$^{\delta}$
δ	Exponent of $l - R$ power law	-
δk	Relative error in specific attenuation if no raindrop canting is assumed	-
κ	Von Kármán constant	0.4
λ	Wavelength	m
μ_{τ}	Mean of characteristic time scale	min
μ_R	Mean of rainfall intensity	mm h^{-1}
μ_k	Mean specific attenuation with varying raindrop canting angles	dB km^{-1}
ρ	Density of moist air	kg m^{-3}

Symbol	Short Description	Value and Units
σ_k^2	Variance of specific attenuation with varying raindrop canting angles	dB km^{-1}
$\sigma_{\ln(I)}^2$	Variance of log-intensity	-
τ	Characteristic time scale	min
θ	Angle with axis of symmetry of raindrop	rad
ξ	Characteristic spatial scale	km
A_T	Sensitivity coefficient of the refractive index of air with respect to temperature	-
A_Q	Sensitivity coefficient of the refractive index of air with respect to humidity	-
A_a	Wet antenna attenuation	dB
A_c	Corrected attenuation	dB
A_m	Measured path-integrated attenuation	dB
CV	Coefficient of variation	-
C_1	Maximum wet antenna attenuation	dB
C_2	Strength of increase of wet antenna attenuation	dB^{-1}
C_3	Antenna drying speed	s^{-1}
C_Q^2	Structure parameter of humidity	kg^2 m$^{-20/3}$
C_T^2	Structure parameter of temperature	K^2 m$^{-2/3}$
C_{TQ}	Cross-structure parameter of temperature and humidity	K kg m$^{-11/3}$
C_n^2	Structure parameter of the refractive index of air	m$^{-2/3}$
$C_{n,\mathrm{min}}^2$	Minimum structure parameter of the refractive index of air	m$^{-2/3}$
$C_{n,\mathrm{max}}^2$	Maximum structure parameter of the refractive index of air	m$^{-2/3}$
D	Raindrop diameter	mm
E	Evaporation	kg m^{-2} s^{-1}
G	Ground heat flux	W m^{-2}
H_s	Sensible heat flux	W m^{-2}
L	Link length	km
L_Ob	Obukhov length	m
L_v	Latent heat of vaporization of water	2.453×10^6 J kg^{-1}
$L_\mathrm{v}E$	Latent heat flux	W m^{-2}

Symbol	Short Description	Value and Units
$L_{\mathrm{v}}E_{\mathrm{EC}}$	Latent heat flux estimated using eddy covariance measurements	W m^{-2}
$L_{\mathrm{v}}E_{\mathrm{RWS-EBM}}$	Latent heat flux estimated using RWS-EBM	W m^{-2}
$L_{\mathrm{v}}E_{\mathrm{RWS-LAS}}$	Latent heat flux estimated using two-wavelength method	W m^{-2}
MBE	Mean bias error of rainfall intensity	mm h^{-1}
N	Raindrop size distribution	mm^{-1} m^{-3}
N_0	Intercept parameter of exponential raindrop size distribution	mm^{-1} m^{-3}
N_{g}	Number of operational gauges	-
N_{s}	Number of samples used to compute errors in rainfall intensity	-
N_{v}	Number of input variables	-
P	Received power	W
P_0	Received power without precipitation	W
Q	Humidity	km m^{-3}
Q_{ext}	Extinction cross-section of raindrop	mm^2
$Q_{\mathrm{ext,X}}$	Extinction cross-section of raindrop for signal with polarizaion X	mm^2
Q_{rel}	Relative humidity	-
R	Rainfall intensity	mm h^{-1}
$\overline{R}$	Path-averaged rainfall intensity	mm h^{-1}
RMSE	Root mean square error of rainfall intensity	mm h^{-1}
R_{c}	Rainfall accumulation	mm
$R_{\mathrm{c,gauges}}$	Rainfall accumulation as measured by gauges	mm
$R_{\mathrm{c,link}}$	Rainfall accumulation as measured by link	mm
R_{d}	Gas constant of dry air	287.04 J kg^{-1} K^{-1}
R_{n}	Net radiation	W m^{-2}
$S_X^{(Y)}$	Sensitivity coefficient of Y with respect to X	-
T	Temperature	K
V	Measured voltage	V
$\overline{V}$	Mean voltage	V
V_Q	Measured voltage corrected for water vapor	V

Symbol	Short Description	Value and Units
V_{QT}	Measured voltage corrected for water vapor and temperature	V
Z	Radar reflectivity factor	$mm^6 \ m^{-3}$
a	Coefficient of $R-k$ power law	$mm \ h^{-1} \ dB^{-b} \ km^b$
a_*	Coefficient of $k-R$ power law	$mm \ h^{-1} \ dB^{-b_*} \ km^{b_*}$
a_Δ	Coefficient of $R-\Delta k$ power law	$mm \ h^{-1} \ dB^{-b_\Delta} \ km^{b_\Delta}$
b	Exponent of $R-k$ power law	-
b_*	Exponent of $k-R$ power law	-
b_Δ	Exponent of $R-\Delta k$ power law	-
c_l	Speed of light in vacuum	$2.99 \times 10^8 \ m \ s^{-1}$
c_p	Specific heat of air at constant pressure	$1005 \ J \ kg^{-1} \ K^{-1}$
d_0	Displacement height	m
d_s	Drop shape function	mm
f	Signal frequency	GHz
f_1	Frequency of first signal	GHz
f_2	Frequency of second signal	GHz
f_{Ob}	Obukhov profile function	-
f_τ	Probability density function of characteristic time scale	min^{-1}
f_ξ	Probability density function of characteristic spatial scale	km^{-1}
f_R	Probability density function of rainfall intensity	$mm^{-1} \ h$
f_V	Probability density function of voltage	V^{-1}
g	Acceleration of gravity	$9.81 \ m \ s^{-2}$
g_R	Integrand for computation of rainfall intensity	m^3
g_k	Integrand for computation of specific attenuation	m^3
h_0	Height of obstacles in terrain	m
j	Imaginary unit	$\sqrt{-1}$
k	Specific attenuation	$dB \ km^{-1}$
$\overline{k}$	Path-averaged specific attenuation	$dB \ km^{-1}$
k_{H_2O}	Specific attenuation by water vapor	$dB \ km^{-1}$
k_X	Specific attenuation for a signal with polarization X	$dB \ km^{-1}$
k_c	Corrected specific attenuation	$dB \ km^{-1}$
k_{nc}	Specific attenuation if no raindrop canting is assumed	-

Symbol	Short Description	Value and Units
l	Thickness of water layer on antenna	m
l_a	Thickness of antenna cover	-
$m_{\mathrm{H_2O}}$	Complex refractive index of water	-
m_air	Complex refractive index of air	-
m_a	Complex refractive index of material of antenna cover	-
n	Refractive index of air	-
p	Air pressure	Pa
r^2	Coefficient of determination	-
$r_\mathrm{x,y}^2$	Squared correlation coefficient between rainfall intensities measured using methods x and y	-
r_{TQ}	Correlation coefficient of temperature and humidity	-
s	Distance along link	km
s_i	Position of gauge i along link	km
s_r	Distance from radar	km
s_rec	Location of the receiver	-
s_tr	Location of the transmitter	-
t	Time	s
t_0	Time at which drying of antennas starts	s
u	Wind velocity	m s^{-1}
u_*	Friction velocity	m s^{-1}
v	Terminal fall velocity of raindrop	m s^{-1}
w_i	Relative weight of measurements by gauge i	-
z_0	Momentum roughness length	m
z_l	Link height	m
z_u	Height of wind velocity measurement	m

CHAPTER 1

Introduction

1.1 Background

Water plays an important role in the climate system of the earth because of its abundance (e.g. *Oki and Kanae*, 2006), its properties related to energy (e.g. *Callen*, 1985), and its role in the transport of matter (e.g. *Dagan*, 1984; *Howard et al.*, 1994). It is also a very important resource (e.g. *Postel et al.*, 1996) and at times a threat (e.g. *Smith et al.*, 1996; *Milly et al.*, 2002; *Delrieu et al.*, 2005) to humans. Therefore, much effort has been put into gaining understanding of the processes that govern the earth's water cycle (e.g. *Brutsaert*, 2005). Theories regarding different aspects of this water cycle have been developed and tested using observations (for a classic example in the field of raindrop size distributions, see *Marshall and Palmer*, 1948). More recently, the availability of computers has made numerical modelling of these aspects and of the entire water cycle possible (e.g. *Manabe and Bryan*, 1969). Many of these numerical models use parameterizations to simplify the description of some processes, in which case the parameters need to be calibrated using observations (e.g. *Beven and Binley*, 1992). In order to initialize and subsequently evaluate these models, it is necessary that observations are available. It is clear that observations of the water cycle are extremely important for both the development of theories and the calibration, initialization and evaluation of numerical models.

One very important aspect of the water cycle that is still poorly understood is the interaction between the atmosphere and the land surface (e.g. *Kochendorfer and Ramírez*, 2005). At the land-atmosphere interface, solar radiation is reflected and absorbed by the soil and vegetation, the ratio of which is determined by the optical properties of the soil and vegetation (e.g. *Bonan et al.*, 1992). The absorbed energy that is not used for photosynthesis by vegeta-

tion is partitioned into different energy fluxes (*Brutsaert*, 1982, 2005), namely long-wave outgoing radiation, soil heat flux, sensible heat flux (i.e. heating of the atmosphere) and latent heat flux (i.e. evaporation and transpiration). This partitioning depends on the properties of the soil and vegetation, on the atmospheric conditions, and on the availability of water for evaporation and/or transpiration (e.g. *Ritchie and Burnett*, 1971; *Shukla and Mintz*, 1982; *Teuling et al.*, 2006b). In order to test theories or to initialize, calibrate and evaluate numerical models of the partitioning of absorbed solar energy, measurements of precipitation and evapotranspiration (i.e. the sum of evaporation and transpiration) are necessary. Evapotranspiration, in turn, is the driving force behind the generation of precipitation so that in order to evaluate theories and numerical models of the occurrence of precipitation, measurements of both of these variables is essential (e.g. *Betts et al.*, 1996).

Relatively accurate measurements of evapotranspiration and precipitation are also needed for short-term operational applications. For instance, prediction of floods (e.g *Smith et al.*, 2001), droughts (e.g. *Stahl and Hisdal*, 2004; *van Lanen et al.*, 2004), and landslides (e.g. *van Asch et al.*, 1999; *Ibsen and Casagli*, 2004; *Talebi et al.*, 2007) depends on these measurements. As it is very difficult to predict exactly when and where precipitation will occur, let alone to predict its intensity, numerical weather prediction models alone will not suffice, especially for flood prediction. Papers in which future directions for the science of hydrology are suggested (*Entekhabi et al.*, 1999; *Kirchner*, 2006) stress the importance of measurements of, among others, precipitation and evapotranspiration.

Both precipitation (e.g. *Uijlenhoet et al.*, 2003) and evapotranspiration (e.g. *Mengelkamp et al.*, 2006; *Teuling et al.*, 2006a) are variable in space and time, over a wide range of scales. Many applications require knowledge of the regional averages of these quantities (e.g. *Parlange et al.*, 1995; *Kirchner*, 2006). This has triggered the development of methods to estimate areal evapotranspiration from point measurements (e.g. *Hupet and Vanclooster*, 2004), and the analysis of the dependence of precipitation on the measurement type for a range of applications (e.g. *Berne et al.*, 2004b; *Kursinski and Zeng*, 2006). Estimation of evapotranspiration at regional scales can be done using a combination of several observations made by different (in situ and remote sensing) instruments (see the review by *Parlange et al.*, 1995), such as sonic anemometers, sodar, and lidar. Areal measurement of precipitation is commonly done using radar. A microwave link is in principle capable of measuring both precipitation (e.g. *Atlas and Ulbrich*, 1977; *Minda and Nakamura*, 2005) and evaporation (*Kohsiek and Herben*, 1983) at regional scales, making it highly suitable for many applications, as will be shown in this thesis.

1.2 Microwave links

A microwave link consists of a transmitter and a receiver, between which an electromagnetic signal propagates. Measurement of precipitation is based on
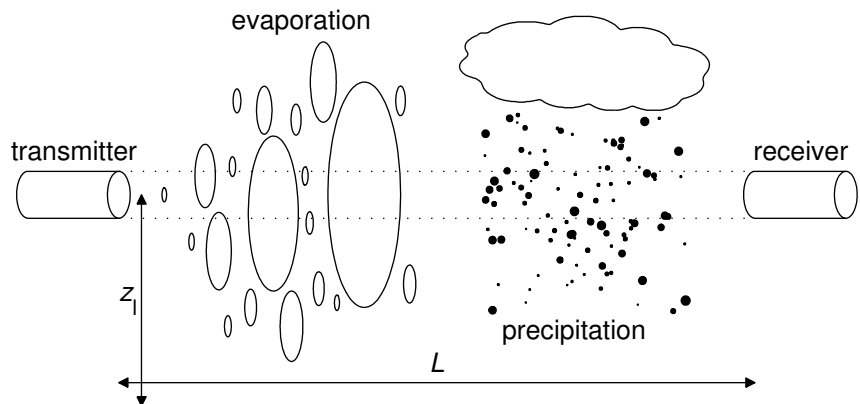
Figure 1.1: The microwave link setup. Turbulent eddies are depicted as ellipses on the left, and precipitation is shown on the right.

the fact that the raindrops in the microwave link path attenuate the signal. Hence, a decrease in received signal level generally indicates an increase of rainfall intensity. Evapotranspiration is derived from measurements of the intensity of fluctuations in the received signal level. These fluctuations are caused by gradients in the refractive index of air due to gradients in water vapor content and temperature of the air in turbulent eddies. The estimation of evapotranspiration from the variation in received signal requires additional knowledge of the turbulent boundary layer, and additional information on either the partitioning of the total available energy between latent and sensible heat fluxes, of the total available energy itself. Therefore assumptions about the turbulent atmospheric boundary layer (see *Wyngaard et al.*, 1971) and additional measurements of atmospheric variables are necessary. The microwave link setup is illustrated in Figure 1.1, where turbulent eddies in the microwave link path are depicted on the left, and raindrops on the right. The link has a length L, and is mounted at a height z_l from the ground.

Microwave links commonly span a few kilometers. Typical dimensions of measurement volumes of ground-based weather radars are somewhat smaller than this. However, radar measurement volumes are often relatively far above the earth's surface (up to a few km), so that vertical heterogeneity in rainfall may cause large errors (see *Berne et al.*, 2004a). This is not a problem for microwave links, as they measure much closer to the earth's surface. Furthermore, the relation between the rainfall intensity and the measured quantity is highly nonlinear for radar measurements (e.g. *Atlas*, 1964), and depends on the distribution of raindrop sizes (e.g. *Uijlenhoet and Stricker*, 1999), which can be highly variable (e.g. *Jameson and Kostinski*, 2002), even within a rain event (e.g. *Uijlenhoet et al.*, 2003; *Testik and Barros*, 2007). This makes radar measurements of rainfall much more prone to errors than microwave link measurements if the frequency of the link is chosen correctly (e.g. *Atlas and Ulbrich*, 1977), so that the relation between the rainfall intensity and the measured

3

quantity is close to linear. The advantage of radars is that their scanning possibilities allow them to measure precipitation over a large area, and at different heights in the atmosphere using a single instrument. In addition to this, most radars are equipped with coherent receivers, so that the Doppler shift of the signal can be used to estimate wind fields and possibly parameters of the raindrop size distribution. Space-borne radar is highly useful in that it can provide global measurements of precipitation, where, especially over oceans, other instruments can't. However, these radars suffer from the same uncertainties as ground-based radars, and additional errors may result from the potentially very strong attenuation at K-band (which is typically used for space-borne radars). The fact that the sampling volume of space-borne radars may be larger than characteristic spatial scales of rainfall, and the sampling interval longer than characteristic timescales of rainfall makes these radars even more prone to errors, as is illustrated by *Steiner et al.* (2003). Beside the sampling uncertainty (point measurements) mentioned above, raingauges suffer from other sources of error (e.g. *Sieck et al.*, 2007). This again illustrates that much is to be gained from using microwave links for the measurement of precipitation.

For the measurement of evapotranspiration, microwave links are used as scintillometers (e.g. *McMillan et al.*, 1983; *Hill et al.*, 1988). The area over which the evapotranspiration is measured depends on the length of the link, its height above the earth's surface and the wind field. However, *Meijninger et al.* (2002a) showed that if the link is long enough and no too far from the ground, the flux footprint (e.g. *Horst and Weil*, 1994) of the link varies only little with respect to its total size. For point measurements (e.g. eddy-covariance methods, profile methods, see *Brutsaert*, 1982) this is not the case (*Horst and Weil*, 1992; *Horst*, 1999), which means that the measured flux may strongly depend on wind direction in heterogeneous terrain. As the footprint of link measurements is much larger than that of point measurements, microwave link measurements of evapotranspiration suffer less from changing wind velocity and direction. On the other hand, the use of point measurements of the total available energy may adversely affect the representativeness of evaporation estimates from scintillometers. Large-scale satellite-based remote sensing of evapotranspiration (e.g. *Su*, 2002; *Bastiaanssen et al.*, 2002) has the same advantages as space-borne radar in the sense that it provides global coverage. However, limiting factors are that its sampling interval is long, it needs relatively clear (i.e. cloudless) conditions, and it is highly dependent on accurate estimates of effective land surface properties through the surface temperature, which introduces additional complications. As microwave links do not suffer from these limitations, it is clear that these instruments would be a welcome addition. Beside microwave scintillometers, visible or infrared (large aperture) scintillometers can also be used to estimate evapotranspiration by estimating the sensible heat flux (e.g. *Meijninger and de Bruin*, 2000) and using the energy balance and measurements of the total available energy, or in combination with a microwave scintillometer (e.g. *Meijninger et al.*, 2002a). In this thesis, the focus will be on the use of a microwave link because of its ability to measure rainfall as well.

4

Finally, it is well known that many microwave links have been installed in the last decade on all continents (except Antarctica) that are operated by cellular communication companies. It has been suggested (*Upton et al.*, 2005) and later shown (see *Messer et al.*, 2006, and Chapter 4 of this thesis) that these links from commercial cellular communication networks can be used to measure rainfall. These existing networks of microwave links offer the exciting possibility to measure rainfall and possibly evapotranspiration over most of the earth's land surface at a high resolution in the near future. This possibility makes it highly worthwhile and relevant to conduct research on the use of microwave links for the measurement of the water flux (both upward and downward) at the land-atmosphere interface.

1.3 Thesis outline

In this thesis, research on the estimation of both evapotranspiration and precipitation is presented. This is done using several data sets, collected in different locations in The Netherlands. Figure 1.2 shows the locations where data were collected. Table 1.1 shows the instruments and their locations that were used to collect the data sets used in different chapters in this thesis.

In Chapters 2 and 3 data from two separate experiments with the same instrument are used to show that it is indeed possible to estimate both of these water fluxes using a single instrument. The first experiment (Chapter 2) was carried out by the Meteorology and Air Quality Group of Wageningen University (see *Meijninger et al.*, 2002a) in the summer of 1998 in Flevoland (see Figure 1.2), where the microwave link was set up as a scintillometer, and eddy covariance measurements at four different locations were taken simultaneously. Other variables that were measured include wind velocity, net radiation, and ground heat flux. The second experiment (Chapter 3) took place a year later near Wageningen (see Figure 1.2), whereby the absolute signal level was stored, and seven raingauges were installed below the microwave link path.

A method to estimate evapotranspiration from microwave link measurements and simultaneous measurements of wind velocity, net radiation, and ground heat flux is presented in Chapter 2. Sensitivity analyses of the result-

Table 1.1: Locations and instruments of data sets used in this thesis, with corresponding chapter numbers

	microwave link	rain gauge	disdrometer	radar
CESAR			5	
De Bilt			3,4,5,6	4
Delft				6
Den Helder				4
Flevoland	2			
Wageningen	3,4	4		

Figure 1.2: Map of The Netherlands with the experimental sites used in this thesis. A list of instruments corresponding to the different locations is given in Table 1.1. Dashed gray lines indicate 50 km ranges from the De Bilt and Den Helder radars, and 15 km range from the Delft radar.

ing evapotranspiration to errors in the various variables required by the method are performed in order to determine the accuracy with which the method can estimate this flux. Limits to the conditions under which the method is applicable are also discussed in this chapter. In the remainder of this thesis, the term evaporation will indicate the sum of evaporation and transpiration (i.e. evapotranspiration).

Chapter 3 deals with the measurement of rainfall. Hence, frozen precipitation is not considered. The principles on which the estimation of rainfall with a microwave link are based are discussed thoroughly in this chapter. Relations between the measured attenuation and the rainfall intensity are derived based on drop size distributions measured by *Wessels* (1972) in De Bilt (see Figure 1.2). Difficulties with the actual estimation of rainfall are identified and discussed.

In Chapter 4 data from microwave links that are part of an operational cellular communication network are used to show that these links can also be

used to measure rainfall. The links that are used for this are also located near Wageningen (see Figure 1.2). Rainfall estimated by these links is compared to that measured by a nearby raingauge and that from the Dutch operational weather radars. The latter is a composite of two C-band weather radars located in De Bilt and in Den Helder (see Figure 1.2), operated by the Royal Netherlands Meteorologial Institute (KNMI). The rain gauge data were collected by the Meteorology and Air Quality Group of Wageningen University. Several limitations of and difficulties with using these commercial links are discussed in this chapter.

Chapters 5 and 6 deal with uncertainties in rainfall estimation using microwave links. In both of these chapters microwave link signals and corresponding "true" path-averaged rainfall intensities are simulated. In Chapter 5, the effect of the microstructure of rain is investigated using two data sets of drop size distributions (DSDs) measured in De Bilt by *Wessels* (1972) and at CESAR (see Figure 1.2), and simulated DSDs based on intense Mediterranean rainfall (*Berne and Uijlenhoet*, 2007). The dependence of microwave link performance on frequency and polarization (combinations) for both single- and dual-frequency links is investigated in this chapter in order to give recommendations on which settings are optimal for rainfall estimation.

In Chapter 6 an extensive (more than 1.5 years) high-resolution radar data set, collected in Delft (see Figure 1.2), is used to investigate the effects of the spatial and temporal macrostructure of rain on single-frequency microwave link rainfall estimates. This data set was collected by the International Research Centre for Telecommunications and Radar (IRCTR) at the Department of Electrical Engineering, Delft University of Technology (TU Delft). The effects of some of the issues raised in Chapters 3 and 4 are analyzed in a simulation framework. For this purpose a semi-empirical relation between rainfall intensity and attenuation caused by wetting of the microwave link antennas is derived.

Conclusions are drawn in Chapter 7. It is clear that the emphasis of this thesis is on rainfall estimation. However, this does not necessarily mean that this is a more important application of microwave links. This is reflceted by the recommendations for future research given in Chapter 7.

Measurement of evaporation

2.1   Introduction

The objective of Chapters 2 and 3 is to show that single-frequency microwave links offer the potential to measure both path-average evaporation and precipitation (see Figure 1.1). In the present chapter, the possibilities and restrictions of microwave links for measuring evaporation are investigated. The measurement of precipitation using microwave links is discussed in Chapter 3.

Areal evaporation is an important component of the exchanges of water and energy between the land surface and the atmosphere. Therefore, accurate knowledge of its spatial and temporal variability is crucial for improving hydrological, meteorological and climate models (e.g. *Parlange et al.*, 1995). Nowadays the estimation of actual evaporation is usually carried out by measuring turbulence statistics at local scales (eddy covariance (EC) method, e.g. *Brutsaert*, 1982), whereas at larger scales highly intermittent, pixel averaged satellite observations (*Bastiaanssen*, 2000; *Bastiaanssen et al.*, 2002; *Su*, 2002) are used. Scintillometers could potentially complement these types of measurements. *Meijninger et al.* (2002b) have shown that scintillometers are relatively insensitive to modest land use heterogeneities. Thus, they provide a greater spatial representation of evaporative flux measurements than point-scale methods like e.g. the EC method. The integrated scales at which scintillometers operate correspond nicely to the grid scales of satelite-based retrieval algorithms of the evaporative flux. As a consequence, scintillometer measurements may

be used as a reference and as validation for these algorithms.

In the recent literature on scintillometry, the emphasis has been on the use of optical or infrared instruments, which, in contrast to microwave scintillometers, measure mainly the sensible heat flux. For example, a recent special issue on scintillometry (see editorial by *de Bruin*, 2002) contains nine papers, of which only one (*Meijninger et al.*, 2002a) deals with microwave scintillometry, in this case in combination with large aperture (optical) scintillometry. A similar combination of scintillometer frequencies was used by *Green et al.* (2000, 2001). Less recently, *Kohsiek and Herben* (1983) have successfully used a stand-alone radio wave scintillometer to estimate the evaporation using several simplifying assumptions. Here, the focus is on a stand-alone radio wave scintillometer because of its potential for measuring precipitation as well (see Chapter 3).

A scintillometer consists of a transmitter and a receiver, typically at a distance of several hundred meters up to a few kilometers, and at a height well inside the surface layer of the atmosphere. The signal propagates through this turbulent atmospheric surface layer, of which the general structure is well-established (e.g. *Pope*, 2000). Local temperature and humidity variations caused by the turbulent eddies produce refractive index fluctuations which in turn cause the electromagnetic signal to scintillate. In Figure 1.1, the refractive index variations in the turbulent eddies are depicted as lenses which cause refraction of the signal. The rain in this figure is shown merely to indicate the potential of the instrument for measuring precipitation. Assuming statistical stationarity, the turbulence intensity averaged over a certain time interval can be described using a so-called structure parameter. The structure parameter of the refractive index of air can be determined by recording the variance of the scintillometer signal at the receiver as will be shown later. Because the refractive index of air is a function of temperature and humidity, the sensible (temperature related) and latent (humidity related) heat fluxes determine the value of this structure parameter. This implies that both heat fluxes can in principle be estimated from the microwave scintillometer signal given an additional constraint. The evaporation E (kg m^{-2} s^{-1}) is directly related to the latent heat flux $L_{\mathrm{v}}E$ (W m^{-2}) through the latent heat of vaporization of water L_{v} ($\approx 2.453 \times 10^6$ J kg^{-1}). *Meijninger et al.* (2002a) obtained good results with a microwave scintillometer using a large aperture (optical) scintillometer (which is mainly sensitive to temperature fluctuations, and thus to the sensible heat flux) to provide the necessary additional constraint. In this work, measurements of the total available energy and the surface energy budget are used to provide this constraint.

In this chapter, a method is presented to estimate the sensible and latent heat fluxes (and hence the evaporation) using microwave links (i.e. radio wave scintillometers) with the surface energy budget constraint. In Section 2.2 this method will be presented, after which its applicability in different conditions will be discussed in Section 2.3. Data obtained with a 27 GHz scintillometer, collected during the Flevoland field experiment (*Meijninger et al.*, 2002b,a), is used to test the method experimentally in Section 2.4, and conclusions will be drawn in Section 2.5.

2.2 The Radio Wave Scintillometry-Energy Budget Method

The quantity that is calculated from the scintillometer signal is the variance of the natural logarithm of the signal intensity at the receiver. This variance is a function of the structure parameter of the refractive index of air C_n^2 (m$^{-2/3}$), which, at radio wave frequencies, depends on the structure parameters of temperature and humidity. These relations will be discussed in Section 2.2.1. The structure parameters of temperature and humidity are in turn related to the sensible and latent heat fluxes through the Monin-Obukhov Similarity Theory (MOST), which will be discussed in Section 2.2.2. The surface energy budget is used to constrain the heat fluxes derived from the scintillometer measurements. This Radio Wave Scintillometry-Energy Budget Method (RWS-EBM) will be presented in Section 2.2.3.

2.2.1 The principle of scintillometry

Tatarskii (1971) has derived a relation between the variance of the natural logarithm of the intensity of a signal with wavelength λ (m) originating from a point source (spherical wave) $\sigma_{\ln(I)}^2$ and the structure parameter of the refractive index of the air between the point source and the receiver

$$C_n^2 = \frac{2^{7/2}\,\Gamma\!\left(\frac{7}{3}\right)\cos\left(\frac{\pi}{12}\right)}{\pi^{8/3}\sqrt{3}\,\Gamma\!\left(\frac{8}{3}\right)}\lambda^{7/6}\left(10^3 L\right)^{-11/6}\sigma_{\ln(I)}^2, \tag{2.1}$$

where $\Gamma()$ is the gamma function and L (km) is the length of the link.

The refractive index of air n (-) is affected by that of dry air, the water vapor present in this air, and the proximity of the signal frequency to an absorption line of water vapor. As a result it is a function of the temperature T (K), the absolute humidity Q (kg m^{-3}) and the pressure p (Pa) of the air. *Hill et al.* (1980) give a relation between the structure parameter of the refractive index of air and the structure parameters of temperature C_T^2 (K^2 m$^{-2/3}$) and moisture C_Q^2 (kg^2 m$^{-20/3}$)

$$C_n^2 = A_T^2 \frac{C_T^2}{T^2} + A_Q^2 \frac{C_Q^2}{Q^2} + 2 A_T A_Q \frac{C_{TQ}}{TQ}, \tag{2.2}$$

where the contribution due to pressure fluctuations is neglected. Following the suggestion by *Kohsiek and Herben* (1983), the cross-structure parameter of temperature and humidity C_{TQ} (K kg m$^{-11/3}$) can be written as $C_{TQ} = r_{TQ} C_T C_Q$, in which r_{TQ} is the correlation coefficient between the temperature and humidity fluctuations. The dimensionless sensitivity coefficients of the refractive index A_T and A_Q at radio wavelengths longer than 3 mm are given

by *Andreas* (1989)

$$A_T = T\frac{\partial n}{\partial T} = -c_1\frac{p}{T} - c_2\frac{Q}{T} \tag{2.3}$$

$$A_Q = Q\frac{\partial n}{\partial Q} = c_2\frac{Q}{T} \tag{2.4}$$

(see also *Hill and Clifford*, 1981), with $c_1 = 0.776 \times 10^{-6}$ K Pa^{-1} and $c_2 = 1.723$ K m^3 kg^{-1}.

2.2.2 Monin-Obukhov similarity theory

The Monin-Obukhov Similarity Theory is valid in the surface layer of the atmosphere, and describes the profiles of momentum and conservative scalars. It is theoretically only valid over homogeneous terrain, but, as stated by *Meijninger et al.* (2002a), the effect of land use heterogeneity is small. MOST can be used to relate the structure parameters C_T^2 and C_Q^2 at a given height in the surface layer to the sensible (H_s) and latent ($L_v E$) heat fluxes (both in W m^{-2})

$$\frac{\rho^2 c_p^2 C_T^2}{H_s^2} = \frac{L_v^2 C_Q^2}{(L_v E)^2} = \frac{1}{u_*^2(z_1 - d_0)^{2/3}} f_{\text{Ob}}\left(\frac{z_1 - d_0}{L_{\text{Ob}}}\right), \tag{2.5}$$

where the specific heat of air at constant pressure is $c_p \approx 1005$ J kg^{-1} K^{-1}, u_* (m s^{-1}) is the friction velocity, z_1 (m) is the height above the terrain, d_0 (m) is the displacement height of the turbulent boundary layer. The Obukhov length L_{Ob} (m) is a measure of the stability of the surface layer, and will be discussed later. The density of moist air ρ (kg m^{-3}) is given by

$$\rho = \frac{p}{R_d T} - 0.61Q \tag{2.6}$$

(e.g. *Brutsaert*, 1982), where R_d (≈ 287.04 J kg^{-1} K^{-1}) is the gas constant of dry air.

The main focus of this chapter will be on estimating evaporation. Because the evaporation is directly related to the latent heat flux, the analyses presented here will concern only the latent heat flux explicitly. The sensible heat flux can easily be computed from this using the surface energy budget. As evaporation occurs predominantly during the daytime, only unstable atmospheric conditions and, correspondingly, only positive (i.e. upward) heat fluxes are considered here.

The shape of f_{Ob} can be derived from the relations given by *Businger et al.* (1971). For unstable conditions ($L_{\text{Ob}} < 0$ m), this function is

$$f_{\text{Ob}}\left(\frac{z_1 - d_0}{L_{\text{Ob}}}\right) = c_1\left(1 - c_2\frac{z_1 - d_0}{L_{\text{Ob}}}\right)^{-2/3}. \tag{2.7}$$

The constants $c_1 = 4.9$ and $c_2 = 7.0$ were empirically derived for C_T^2 profiles by *Wyngaard et al.* (1971). *Andreas* (1988) later corrected the second constant to

be $c_2 = 6.1$ to take into account the new value of the von Kármán constant κ (= 0.4, *Wyngaard et al.* (1971) assumed $\kappa = 0.35$). An alternative expression exists for stable conditions, which is not used here because it falls outside the scope of this thesis. The Obukhov length is given by (e.g. *Brutsaert*, 1982)

$$L_{\mathrm{Ob}} = -\frac{\rho u_*^3}{\kappa g \left(\frac{1}{c_p T} H_{\mathrm{s}} + \frac{0.61}{L_{\mathrm{v}}} L_{\mathrm{v}} E \right)}, \tag{2.8}$$

where g is the acceleration of gravity (≈ 9.81 m s^{-2}) and κ is the von Kármán constant (≈ 0.4). Given a wind velocity u (m s^{-1}) measured at a height above the terrain z_u (m), the friction velocity can be calculated using

$$u_* = \frac{\kappa u}{\ln \left(\frac{z_u - d_0}{z_0} \right) - \Psi \left(\frac{z_u - d_0}{L_{\mathrm{Ob}}} \right) + \Psi \left(\frac{z_0}{L_{\mathrm{Ob}}} \right)} \tag{2.9}$$

(e.g. *Brutsaert*, 1982), where z_0 (m) is the momentum roughness length of the terrain, and Ψ is the Businger-Dyer expression

$$\Psi \left(\frac{z}{L_{\mathrm{Ob}}} \right) = 2 \ln \left(\frac{1 + x}{2} \right) + \ln \left(\frac{1 + x^2}{2} \right) - 2 \arctan(x) + \frac{\pi}{2}, \tag{2.10}$$

with

$$x = \left(1 - 16 \frac{z}{L_{\mathrm{Ob}}} \right)^{1/4}. \tag{2.11}$$

These empirical relations have been shown to be valid in the range $-\frac{z}{L_{\mathrm{Ob}}} \lesssim 2$.

The roughness length z_0 and the displacement height d_0 both depend on the height, the spacing and the shape of upwind obstacles in the field. For non-sparse vegetation, *Brutsaert* (1982) relates these parameters to the average height of the obstacles h_0 (m) according to

$$z_0 = \frac{1}{8} h_0 \tag{2.12}$$

$$d_0 = \frac{2}{3} h_0. \tag{2.13}$$

In an extensive literature review *Wieringa* (1992) has tabulated z_0 as a function of terrain type. Equations (2.12) and (2.13) can be used to compute d_0 from this roughness length. The independent quantity that will be used in the remainder of this chapter will be h_0.

2.2.3 Energy budget constraint

The system of equations presented in Section 2.2.2 can be closed by using the principle of conservation of energy, which requires the sum of the latent and sensible heat fluxes to be equal to the total available energy

$$L_{\mathrm{v}} E + H_{\mathrm{s}} = R_{\mathrm{n}} - G, \tag{2.14}$$
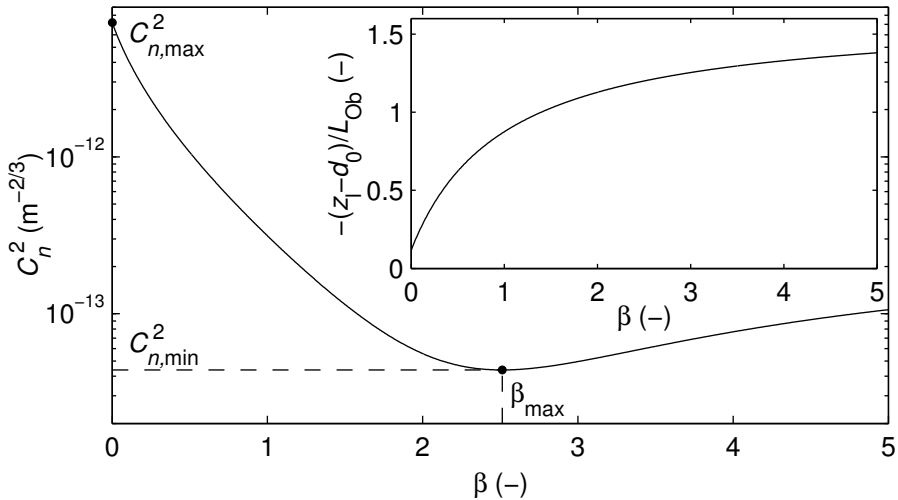
Figure 2.1: C_n^2 and $-\frac{z_1-d_0}{L_{Ob}}$ as functions of β, for $R_n - G = 400$ W m^{-2}, $u = 3.0$ m s^{-1}, $h_0 = 0.5$ m and $r_{TQ} = 0.9$.

where R_n (W m^{-2}) is the net radiation and G (W m^{-2}) is the ground heat flux (both positive when downward). For convenience the Bowen ratio, defined as the ratio of the sensible and latent heat fluxes, is used as the variable to be computed

$$\beta = \frac{H_s}{L_v E}. \tag{2.15}$$

Both heat fluxes can then be computed from β using $R_n - G$ and Eq. (2.14)

$$H_s = \frac{\beta}{1 + \beta}(R_n - G) \tag{2.16}$$

$$L_v E = \frac{1}{1 + \beta}(R_n - G). \tag{2.17}$$

With the energy budget (Eq. (2.14)), the number of equations (four: Eqs. (2.2), (2.5) and (2.14), where Eq. (2.5) represents two equations) equals the number of unknowns (four: C_T^2, C_Q^2, H_s and $L_v E$) so that the Bowen ratio (and hence the turbulent fluxes) can in principle be solved, albeit implicitly. As an example, Figure 2.1 shows the $C_n^2(\beta)$ relation for $R_n - G = 400$ W m^{-2}, $u = 3.0$ m s^{-1}, $h_0 = 0.5$ m and $r_{TQ} = 0.9$. The pressure, temperature and humidity are taken as constants here and in Section 2.3 ($p = 101.3$ kPa, $T = 288.15$ K, $Q = 0.015$ kg m^{-3}), as changes in these variables do not greatly affect results. The height of the scintillometer and the height of the wind velocity measurements are also constant in the remainder of this chapter. Their values ($z_1 = 10.9$ m and $z_u = 3.9$ m) correspond to those of the experimental setup

described in Section 2.4. Figure 2.1 also shows that the values of $-\frac{z_1-d_0}{L_{\mathrm{Ob}}}$ are within the range of validity of the relations used in Section 2.2.2 (i.e. $\lesssim 2$).

2.3 Applicability

As can be seen from Figure 2.1, the solution of the system of equations presented in the previous section does not exist for all values of C_n^2, and is not unique in the range where it does exist. This will be discussed in Section 2.3.1. It can also be seen from Figure 2.1 that the solution is much more sensitive to changes (or errors) in C_n^2 for higher values of β (dry conditions) than for low values of β (wet conditions). An analysis of the sensitivity of the method to different variables will be given in Section 2.3.2. Factors that may introduce errors in the estimated evaporative flux are discussed in Section 2.3.3.

2.3.1 Region of validity

For a certain range of values of C_n^2, the system of equations presented in Section 2.2 has multiple solutions. As radio wave scintillometers are influenced more by humidity fluctuations (related to the latent heat flux) than by temperature fluctuations (associated with the sensible heat flux), this type of instrument is best suited for wet to moderately dry conditions. Therefore only the solution in the region $\beta < \beta_{\max}$ is considered (see Figure 2.1).

Figure 2.1 shows that $\frac{\partial C_n^2}{\partial \beta}$ is negative in the region $\beta < \beta_{\max}$. This means there is a physical constraint on the value of C_n^2 (which has a maximum at $\beta = 0$). When β approaches 0, $L_{\mathrm{v}}E$ approaches $R_{\mathrm{n}} - G$ and C_n^2 approaches $\frac{A_Q^2}{Q^2}C_Q^2$, which implies (see Eq. (2.5))

$$C_n^2 \le C_{n,\max}^2 = \frac{c_1(R_{\mathrm{n}}-G)^2 A_Q^2}{L_{\mathrm{v}}^2 u_*^2 (z_1-d_0)^{2/3} Q^2}\left(1 - c_2\frac{z_1-d_0}{L_{\mathrm{Ob}}}\right)^{-2/3}, \qquad (2.18)$$

where L_{Ob} (see Eq. (2.8)) now reduces to

$$\lim_{\beta \to 0} L_{\mathrm{Ob}} = -\frac{\rho L_{\mathrm{v}} u_*^3}{0.61\kappa g(R_{\mathrm{n}}-G)}. \qquad (2.19)$$

Unfortunately, there is no simple analytical expression for $\beta_{\max}$ or $C_{n,\min}^2$ for arbitrary values of r_{TQ}. However, when $r_{TQ} = \pm 1$, Eq. (2.2) can be rewritten using Eq. (2.5):

$$C_n^2 = \left(\frac{A_T}{T}C_T + r_{TQ}\frac{A_Q}{Q}C_Q\right)^2 = \left(\frac{A_T}{T}\frac{L_{\mathrm{v}}}{\rho c_p}\beta + r_{TQ}\frac{A_Q}{Q}\right)^2 C_Q^2.$$

Hence the zero in $\frac{\partial C_n^2}{\partial \beta}$ now coincides with $C_n^2 = 0$ m$^{-2/3}$ so that $C_{n,\min}^2 = 0$ m$^{-2/3}$. The corresponding $\beta_{\max}$ only depends on p, Q and T. Deviations of r_{TQ} from ± 1 result in $C_{n,\min}^2 > 0$ m$^{-2/3}$ (see Figure 2.1) and higher values

15

of $\beta_{\max}$, so that the safest estimate of the maximum Bowen ratio is that for $r_{TQ} = \pm 1$. For common atmospheric conditions in temperate climates, $\beta_{\max} \geq 2.5$.

If the measured value of C_n^2 is not between $C_{n,\min}^2$ and $C_{n,\max}^2$, it can be concluded that the measurements are not consistent with the inversion model assumptions. This implies that either the assumptions in RWS-EBM are not valid under the given circumstances and/or the measured value of C_n^2 is affected by factors other than the turbulent fluxes (see also Section 2.3.3).

2.3.2 Sensitivity

In the remainder of this chapter, the latent heat flux will be treated as the resulting variable of the RWS-EBM, as this variable is directly related to the evaporation, which is the main focus of this chapter. Apart from $R_{\mathrm{n}} - G$, the RWS-EBM is sensitive to C_n^2 and the meteorological variables u and r_{TQ}. Because the effective roughness length z_0 can usually only be roughly estimated, it is important to quantify the effect of uncertainties in h_0 (which is directly linked to z_0 and d_0 through Eqs (2.12) and (2.13), respectively). The method is relatively insensitive to T, Q and p under commonly occurring atmospheric conditions, so that these variables will not be considered here. The degree to which C_n^2, u, $R_{\mathrm{n}} - G$, h_0 and r_{TQ} affect the resulting latent heat flux is analyzed here. The larger the effect, the more important it is to accurately measure or estimate the particular variable.

The sensitivity analysis will be carried out similarly to that of *Andreas* (2000), where the relative change in the resulting variable is expressed in terms of a linear combination of the relative changes in the input variables. If Y is the resulting variable, and X_i $(i = 1, 2, \ldots N_{\mathrm{v}})$ are the N_{v} input variables, the relative change in Y can be expressed as

$$\frac{\mathrm{d}Y}{Y} = \sum_{i=1}^{N_{\mathrm{v}}} S_{X_i}^{(Y)} \cdot \frac{\mathrm{d}X_i}{X_i}, \tag{2.20}$$

where

$$S_{X_i}^{(Y)} = \frac{X_i}{Y} \left(\frac{\partial Y}{\partial X_i} \right) \tag{2.21}$$

is defined as the sensitivity coefficient of Y to X_i. Of course, these sensitivity coefficients only relate the relative changes if the changes themselves are small, or if the relation between X_i and Y is linear (otherwise the value of $\frac{\partial Y}{\partial X}$ may change significantly).

The sensitivity coefficients of $L_{\mathrm{v}}E$ to C_n^2, $R_{\mathrm{n}} - G$, u, h_0 and r_{TQ} have been computed for different values of C_n^2, $R_{\mathrm{n}} - G$, u, h_0 and r_{TQ}, all within a range that is commonly observed. Because the graphs are relatively similar for these different values, Figure 2.2, which only shows the sensitivity coefficients as a function of C_n^2 with $R_{\mathrm{n}} - G = 400$ W m^{-2}, $u = 3.0$ m s^{-1}, $h_0 = 0.5$ m and $r_{TQ} = 1$, may be considered to be illustrative for the entire range of commonly observed values of these variables. The superscript in $S_X^{(L_{\mathrm{v}}E)}$ (Eq. 2.21) is
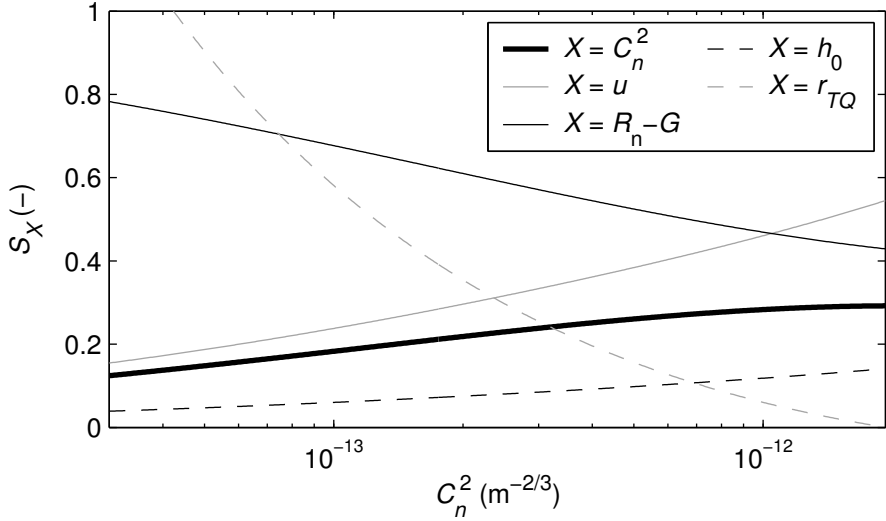
Figure 2.2: Sensitivity coefficients of L_vE as a function of C_n^2, with $R_n - G = 400$ W m^{-2}, $u = 3.0$ m s^{-1}, $h_0 = 0.5$ m and $r_{TQ} = 1$.

omitted for clarity of notation. The latent heat flux is most sensitive to the total available energy, which is to be expected because L_vE is directly related to $R_n - G$ (see Eqs (2.14) and (2.15)). This indicates that the RWS-EBM relies heavily on accurate measurements or estimates of $R_n - G$. The other central variable of the RWS-EBM, C_n^2, is also shown to strongly affect L_vE, especially for higher values of C_n^2 (i.e. under relatively wet conditions). This is essential, as the RWS-EBM has been developed based on this sensitivity. The sensitivity of the latent heat flux to the wind velocity u becomes larger as C_n^2 increases, so that it is also important to accurately measure the wind velocity. Because h_0 affects L_vE much less than the other variables, a rough estimate is usually good enough for the RWS-EBM. For high values of C_n^2, the sensitivity of the latent heat flux estimate to r_{TQ} is relatively small, which means that errors in the estimate of this variable will not be very important in this range. This sensitivity becomes much larger for low values of C_n^2, although this is partly caused by the lower values of the resulting L_vE, which is the denominator of $S_{X_i}^{(Y)}$ in Eq. (2.21). Therefore, correctly estimating r_{TQ} becomes more important during dry conditions (small C_n^2). The effect of errors in r_{TQ} is further discussed in Section 2.3.3.

2.3.3 Sources of error

Because there are usually no measurements of r_{TQ} available, it is assumed that $r_{TQ} = 1$ in the remainder of this chapter. *Katul et al.* (1995), using eddy correlation measurements over different terrain types (natural uneven-age forest, uniform bare soil and grass-covered pine forest), show that for unstable
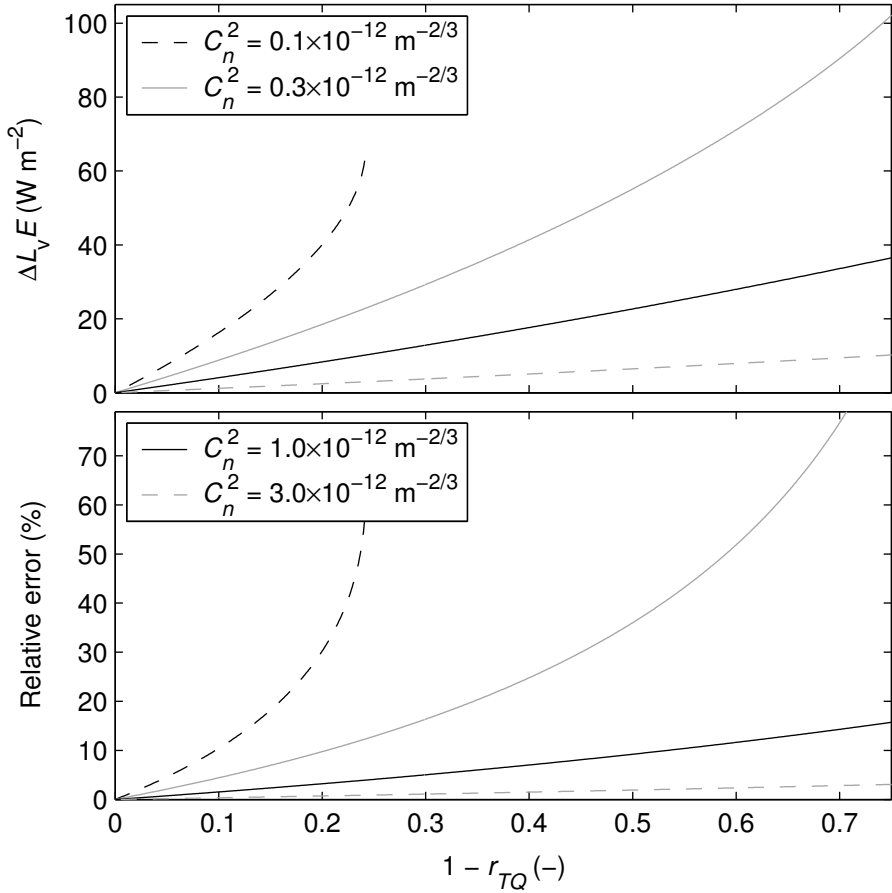
Figure 2.3: The error in $L_{\mathrm{v}}E$ resulting from a deviation of the actual r_{TQ} from the assumed value of 1, for different values of C_n^2, with $R_{\mathrm{n}} - G = 400$ W m^{-2}, $u = 3.0$ m s^{-1}, and $h_0 = 0.5$ m. The line for $C_n^2 = 0.1 \times 10^{-12}$ does not go beyond $1 - r_{TQ} = 0.24$ (where $\Delta L_{\mathrm{v}}E = 62.8$ W m^{-2}) because otherwise $C_n^2 < C_{n,\mathrm{min}}^2$.

conditions ($-\frac{z}{L_{\mathrm{Ob}}} \leq 1$) values of r_{TQ} increase with increasing $-\frac{z}{L_{\mathrm{Ob}}}$ and are typically between 0.4 and 1. Figure 2.3 shows the absolute ($\Delta L_{\mathrm{v}}E$) and relative errors in the latent heat flux resulting from erroneously assuming $r_{TQ} = 1$ as a function of the actual value of r_{TQ}, for different values of C_n^2. The other variables are held constant at $R_{\mathrm{n}} - G = 400$ W m^{-2}, $u = 3.0$ m s^{-1} and $h_0 = 0.5$ m. An overestimation of r_{TQ} will always lead to an overestimation of $L_{\mathrm{v}}E$, which can also be seen in Figure 2.2, where $S_{r_{TQ}} > 0$. As was concluded in Section 2.3.2, the error resulting from an error in r_{TQ} is lower for high values of C_n^2. Even for significant overestimates of r_{TQ}, the error in the latent heat flux is not extremely large at moderate to large values of C_n^2 (i.e. under relatively

wet conditions).

A major source of error in the use of radio wave scintillometers lies in the fact that they are highly sensitive to mechanical oscillations. This means that if either the transmitter or the receiver (or both) is mounted on a structure that vibrates in the wind, the derived C_n^2 values will likely be overestimated (see e.g. *Meijninger et al.*, 2002a). The fluctuations in the signal caused by fluctuations in the path-integrated absorption by atmospheric constituents (which are relatively slow compared to the turbulence-induced scintillations) can also contribute considerably to the derived C_n^2 (*Green et al.*, 2001). Moving scatterers such as trees close to the signal path can scatter part of the beam towards the receiver, in which case the signal fluctuations are again enhanced. Careful positioning of the instrument is therefore very important.

The error in C_n^2 due to these effects is generally positive, so that the latent heat flux will be overestimated using the proposed method. Generally, if such errors occur, this can be noticed by the fact that the measured C_n^2 may exceed $C_{n,\mathrm{max}}^2$, especially under relatively wet conditions.

2.4   Experimental verification

The RWS-EBM will be tested using data collected in the Flevoland field experiment, which will be described in Section 2.4.1. The results will be compared to eddy covariance (EC) measurements and to latent heat fluxes derived from a combination of a RWS and a Large Aperture Scintillometer (LAS) in Section 2.4.2.

2.4.1   The Flevoland field experiment

The processed data set from the Flevoland field experiment as described by *Meijninger et al.* (2002b,a) is used in this chapter. This experiment was carried out in the southern part of Flevoland, The Netherlands (see Figure 1.2), between July 18 and August 20, 1998. This was a wet period, in which the evaporation was close to potential most of the time. A 27-GHz scintillometer system with 0.6-m diameter antennas, manufactured at the Eindhoven University of Technology and on loan from the Horticultural Research Institute of New Zealand (*Green et al.*, 2000, 2001) was used for this experiment. It was mounted on two wind turbines, placed 2.2 km apart, at a height of 10.9 m (both the transmitter and the receiver). The intensity of the receiver signal was band-pass filtered between 0.03 Hz and 20 Hz, and sampled at a rate of 10 Hz. Of this sampled signal, the variance was taken over 30-minute periods and recorded. All other measured variables were averaged over the same 30-minute periods in this experiment. Because the terrain around the scintillometer is completely flat, the height of the scintillometer above the terrain z_l is constant. For further details concerning this experiment, the reader is referred to the work by *Meijninger et al.* (2002a,b).
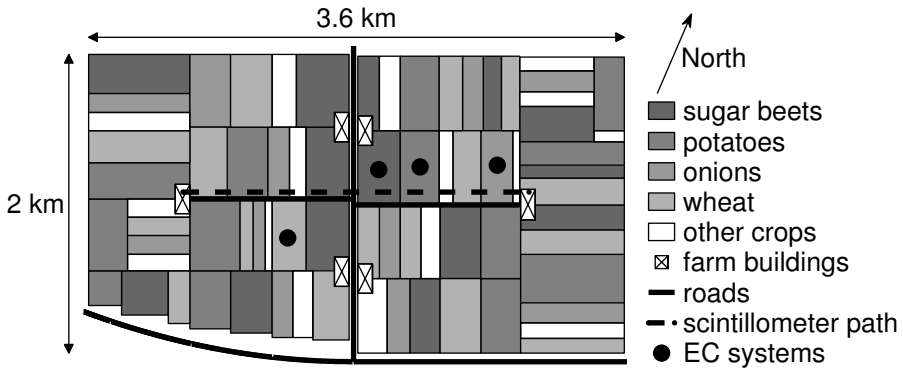
Figure 2.4: Land use map of the study area (after *Meijninger et al.*, 2002b).

The heat fluxes that affect the scintillometer signal originate from rectangular plots with dimensions of approximately 0.5 km, where potatoes, sugar beets, wheat and onions are grown. Figure 2.4 shows that the spatial distribution of these plots is roughly isotropic (which makes the source distribution roughly independent of the wind direction), and each of the four crop types covers approximately 25% of the total area around the scintillometer. The effective roughness length z_0 was estimated by *Meijninger et al.* (2002b) to be relatively uniform at 0.06 m (so that $h_0 = 0.48$ m, see Eq. (2.12)) over the entire area.

In four of the plots (each with a different crop type), eddy covariance (EC) systems were installed (see Figure 2.4) to independently measure the heat and momentum fluxes and the correlation coefficient between the temperature and humidity fluctuations. These EC systems were mounted on masts at 4.8 m above the terrain in the sugar beet field, at 3.5 m in the wheat and potato fields, and at 2.8 m in the onion field. Footprint analyses have been conducted by *Meijninger et al.* (2002a) to verify whether the fluxes measured by the EC systems were indeed those originating from the respective fields. In addition to these EC measurements, net radiation and ground heat flux were measured at each site. For the energy fluxes measured by the EC systems ($L_v E$ and H_s), the uncertainty is defined as the 95% confidence interval as determined in Appendix A of *Meijninger et al.* (2002b). The measurement uncertainty in the other heat fluxes (R_n and G) is taken as the 95% confidence interval as given by the manufacturer of the instruments. Weights are assigned to the fluxes measured by the EC systems according to the wind direction and a footprint analysis (*Meijninger et al.*, 2002b). A weighted average of the latent heat fluxes measured by the EC systems, which differs only slightly from the unweighted average, is used here to compare to the results of the RWS-EBM.

The wind velocity u used in this section was measured at $z_u = 3.9$ m, and the temperature T and humidity Q were measured at 3.1 m at the sugar beet site. Because there will usually be only one point at which meteorological

variables are measured in an operational setting with a stand-alone radio wave scintillometer, the total available energy $(R_n - G)$ used in this study is also the one that has been measured at the sugar beet site. The mean value of the spatial standard deviation of $R_n - G$ normalized by its spatial mean is only 6.6%. Therefore, the use of only one point measurement will not introduce major errors. The atmospheric pressure was not measured during the Flevoland experiment. It is assumed to be constant at a value of $p = 101.3$ kPa.

In addition to the radio wave scintillometer, a large aperture infrared $(\lambda = 930$ nm) scintillometer (LAS) was mounted on the same wind turbines at a height of 11.6 m by *Meijninger et al.* (2002a,b). Heat fluxes can be estimated by combining the C_n^2 estimates from the two scintillometers using the so-called two-wavelength method (*Andreas*, 1989). In this method, Eq. (2.2) is used twice (with different values of C_n^2, A_T and A_Q for the two wavelengths) in combination with Eq. (2.5) (again representing two equations) to solve the four unknowns (C_T^2, C_Q^2, H_s and L_vE). Hence, the RWS-LAS method is independent of the measured total available energy. The latent heat flux resulting from the RWS-EBM will be compared to this RWS-LAS two-wavelength heat flux as well.

2.4.2   Results

The scintillometer data used in the comparison are those recorded during daytime (between 9:00 and 18:00) for which measurements of u, R_n, G, T and Q are available at the sugar beet site. *Meijninger et al.* (2002a) have made an additional selection based on visual inspection of the time series of their resulting values of L_vE compared to those measured by the EC systems. Unrealistically high values were found to be caused by mechanical oscillations of the microwave link system setup (which was physically connected to wind turbines) due to wind, and have been discarded. This additional selection indeed removes most of the occurrences of measured C_n^2 values exceeding $C_{n,\max}^2$. Therefore, the data points that were used by *Meijninger et al.* (2002a) are employed in the current analysis as well. The resulting dataset consists of 92 30-minute intervals.

Figure 2.5 shows the comparison of the latent heat fluxes derived from the RWS-EBM with $r_{TQ} = 1$ ($L_vE_{\mathrm{RWS-EBM}}$) to the weighted EC measurements (L_vE_{EC}), the RWS-LAS two-wavelength method ($L_vE_{\mathrm{RWS-LAS}}$), and the RWS-EBM with measured values of r_{TQ}. In this last analysis, over 90% of the values of r_{TQ} exceed 0.5, and approximately 67% are greater than 0.75. The lower values of r_{TQ} occur at low values of $R_n - G$, so that the absolute error in L_vE caused by assuming $r_{TQ} = 1$ is smaller than expected from Figure 2.3. The error bars in the RWS-EBM results are solely caused by errors in $R_n - G$, as no error estimates for C_n^2 and the other variables were available. This is also the reason why no error bars are shown for the RWS-LAS analysis. A linear regression has been performed for each of the flux comparisons, and the resulting slopes c and coefficients of determination r^2 are given in the graphs.

The RWS-EBM seems to overestimate the latent heat flux when compared

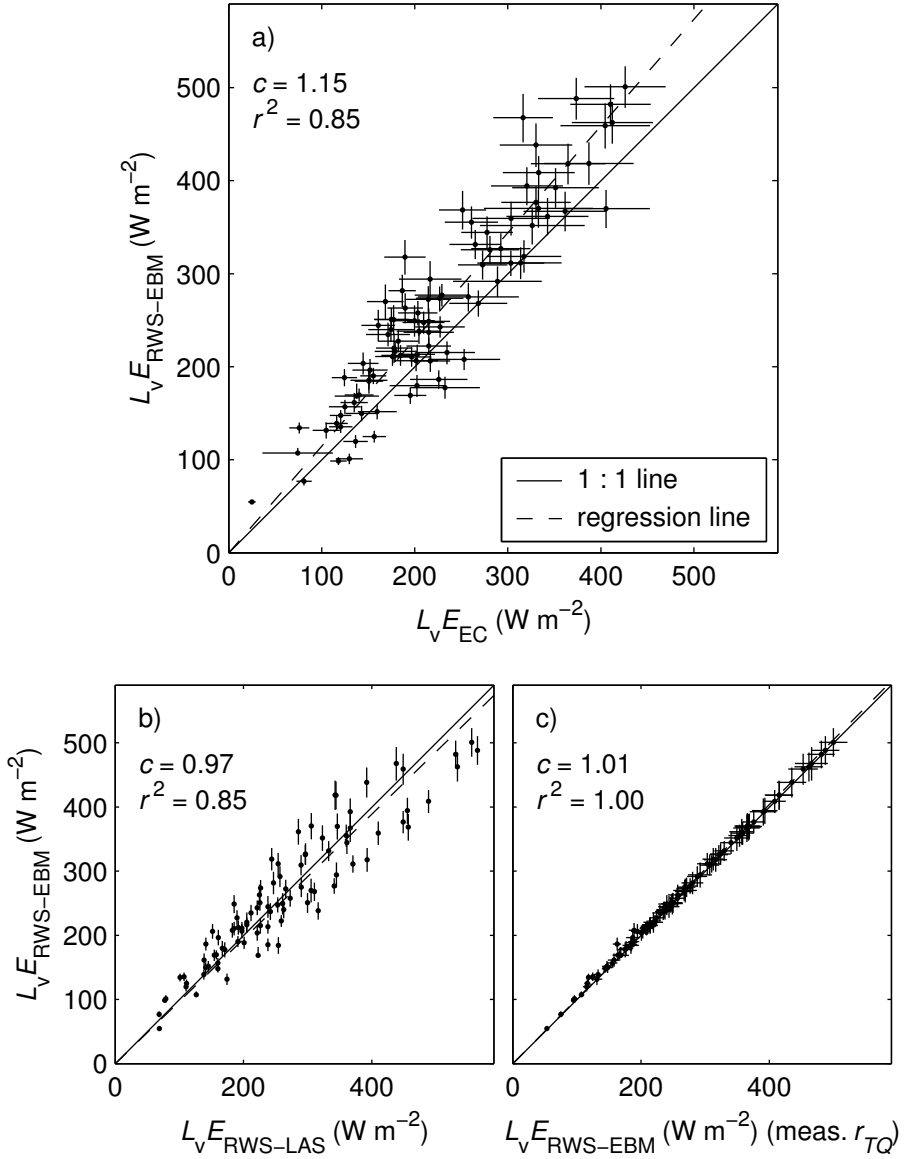**Figure 2.5:** Comparison of the latent heat flux estimated using the RWS-EBM and that estimated using a) weighted EC measurements; b) combined RWS and LAS measurements (the two-wavelength method); c) the RWS-EBM with r_{TQ} values measured by the EC systems. The slopes of the linear regression lines c and their coefficients of determination r^2 are shown in the top-left corners of the graphs.
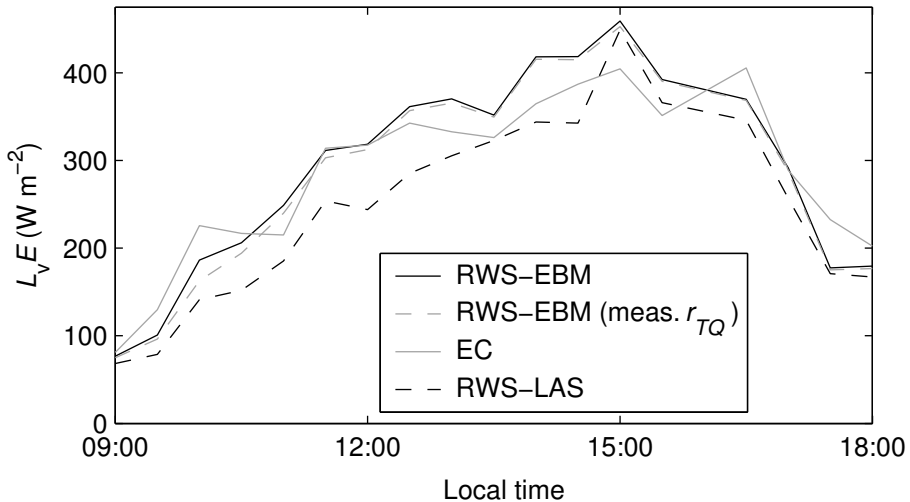
Figure 2.6: Time series of the latent heat fluxes determined using different methods on July 27, 1998.

to the latent heat flux measured by the EC systems ($c = 1.15$). However, the sum of the sensible and latent heat fluxes measured by the EC systems does not close the energy budget, whereas the RWS-EBM closes the energy budget by definition. Least-squares estimation of c in $R_{\mathrm{n}} - G = c(L_{\mathrm{v}}E + H_{\mathrm{s}})$ using the fluxes measured by the EC systems gives $c = 1.13$, with a coefficient of determination $r^2 = 0.90$. This non-closure of the EC-derived energy budget explains the apparent overestimation by the RWS-EBM. The high coefficient of determination ($r^2 = 0.85$) indicates that the RWS-EBM captures the dynamics correctly (85% of the variance explained). The comparison of the RWS-EBM to the RWS-LAS two-wavelength method, with $c = 0.97$ and $r^2 = 0.85$ leads to the same conclusion, although this evidence is less strong as the two methods are not independent. The major advantage of the RWS-EBM over RWS-LAS is that only one scintillometer is needed in the former (with additional measurements of $R_{\mathrm{n}} - G$), whereas two are needed in the latter. The third comparison is not meant as a verification of the method but more as an analysis of the effect of the assumption that $r_{TQ} = 1$ for real data. It is clear from this comparison that the effect of $r_{TQ} < 1$ is very small compared to the size of the error bars (which are solely caused by errors in $R_{\mathrm{n}} - G$).

Figure 2.6 shows the evolution of the latent heat fluxes of Figure 2.5 on July 27, 1998. This day was chosen because it was the only day for which data were continuously available. It can be seen that the latent heat fluxes estimated using the different methods are similar, which again leads to conclusion that the RWS-EBM reasonably captures the evaporation dynamics during the Flevoland experiment.

2.5 Conclusions

A method has been presented that uses radio wave scintillometer measurements in combination with measurements of the total available energy to estimate the latent heat flux, and hence the evaporation: the Radio Wave Scintillometry-Energy Budget Method (RWS-EBM). It has been demonstrated that given the meteorological conditions and assuming the Monin-Obukhov similarity theory to be valid, the range of physically possible values of C_n^2 is limited. Measured values that exceed $C_{n,\mathrm{max}}^2$ may indicate measurement errors. The method is best suited for relatively wet conditions, as the RWS is most sensitive to humidity fluctuations. If conditions become too dry, the non-uniqueness of the solution of the system of equations may become important, so that an incorrect flux may be estimated.

Sensitivity analyses indicate that it is important to accurately measure or estimate the total available energy $R_\mathrm{n} - G$ and the wind velocity u in order to obtain reliable estimates of the latent heat flux. The fact that r_{TQ} is often unknown in an operational setting is found to be unimportant in wet conditions, although uncertainties in r_{TQ} can cause larger errors in the resulting latent heat flux during dry conditions. This is a second reason why this method (and the use of RWS in general) is most suitable for use in relatively wet conditions, up to Bowen ratio values of $\beta \approx 2$.

The application of RWS-EBM to experimental data collected in southern Flevoland, the Netherlands in the summer of 1998 yields good results when compared to independent EC measurements of the latent heat flux and to results of the RWS-LAS two-wavelength method. The errors caused by the assumption that $r_{TQ} = 1$ are shown to be very small for these data. It can be concluded from these experimental results that the proposed method works well, at least for relatively wet conditions. More experimental research needs to be done to investigate the performance of the RWS-EBM under drier conditions.

Measurement of rain

3.1 Introduction

The potential of microwave links to estimate path-averaged evaporation has been discussed in Chapter 2. The present chapter deals with the estimation of path-averaged precipitation using the same instrument. This combination makes this type of instrument potentially highly suitable for both hydrological and meteorological applications.

Measurement of rainfall on several spatial and temporal scales is extremely important in hydrology, especially in urban settings (e.g. *Smith et al.*, 2002; *Leijnse et al.*, 2002; *Berne et al.*, 2004b) where processes on the scale of neighborhoods can be very important. *Upton et al.* (2005) propose that microwave links are ideal for measurement of rainfall for hydrological applications in urban settings (see also *Grum et al.*, 2005). In addition to this, rainfall estimated from microwave links could be used for calibration and verification of ground-based or space-borne radar measurements (*Rahimi et al.*, 2004; *Krämer et al.*, 2005) and for hydrologic or climate models. As such, microwave links may serve to bridge the scale gap between the traditional instruments used to measure rainfall (i.e. weather radar and raingauges). Because of their integrating character, microwave links will suffer less from sampling errors and can measure at higher temporal resolution than raingauges, especially at low rainfall intensities. Much can be gained from line measurements of the rainfall intensity in

addition to point (raingauges) and areal (radar) measurements.

Most recent studies on rainfall estimation using microwave links focus on either dual-polarization (*Ruf et al.*, 1996) or dual-frequency (*Rincon and Lang*, 2002; *Rahimi et al.*, 2003) techniques, both yielding very promising results. In a comparison between single-frequency and dual-frequency microwave links, *Holt et al.* (2003) conclude that the suitability of single-frequency links for measuring path-averaged rainfall approaches that of dual-frequency links only at frequencies around 24 GHz owing to the fact that the relation between signal attenuation and rainfall intensity is nearly linear and relatively insensitive to variability in drop size distribution climatology and rain temperature at this frequency. The 27-GHz microwave link used in this study operates relatively close to this frequency and is therefore expected to perform reasonably well. Use of this frequency was also suggested by *Atlas and Ulbrich* (1977). In a recent study, *Minda and Nakamura* (2005) have shown that with a 50-GHz microwave link, operating far outside the suitability range proposed by *Holt et al.* (2003), path-averaged rainfall intensity can still be estimated with reasonable accuracy.

A detailed description of a microwave link (or radio wave scintillometer) can be found in Chapter 2. The electromagnetic waves propagating between the transmitter and receiver of the link are affected by raindrops. A portion of the energy in these waves is absorbed or scattered by the raindrops. The sum of this absorption and scattering is what causes the receiver to detect less radiative energy than would be the case if no rain were present. The relative decrease of the power (in dB) of the propagating signal per unit distance, the specific attenuation k (dB km^{-1}), can be used to estimate path-averaged rainfall.

The method by which rainfall intensity is estimated from the specific attenuation measured by the microwave link is described in Section 3.2. The method is verified experimentally using data collected in an experiment described in Section 3.3. Conclusions will be drawn in Section 3.4.

3.2   Method

The microwave link signal is attenuated by raindrops in its path. Each raindrop interacts with the electromagnetic signal because its dielectric properties differ from those of the surrounding air. Because both the rainfall intensity R (mm h^{-1}) and the signal attenuation k (dB km^{-1}) depend on the number concentration and sizes of the raindrops, the two quantities can be related.

3.2.1   Theory

The relative decrease in power between the source of an electromagnetic signal (the transmitter) and a point in space (at a distance L from this source) due to attenuation by rainfall is given by (e.g. *Battan*, 1973)

$$\frac{P(L)}{P_0(L)} = \exp\left(-\frac{\ln(10)}{10} \int_0^L k(s)\mathrm{d}s\right), \tag{3.1}$$

where P_0 is the signal power without attenuation by rain. Measuring the signal power using a receiver at a distance L, the path-integrated attenuation $A_{\mathrm{m}} = \int_0^L k(s)\mathrm{d}s$ (in dB) can be derived. The objective is now to estimate path-averaged rainfall intensity $\overline{R}$ from the measured path-averaged specific attenuation $\overline{k}$, using a relation between k and R.

The specific attenuation and the rainfall intensity can both be computed by integrating the drop size distribution (DSD) $N(D)$ (m^{-3} mm^{-1}), weighted by appropriate functions (e.g. *Atlas and Ulbrich*, 1977)

$$k = \frac{10^{-2}}{\ln(10)} \int_0^\infty Q_{\mathrm{ext}}(D)N(D)\mathrm{d}D \qquad (3.2)$$

$$R = 6\times10^{-4}\pi \int_0^\infty D^3 v(D)N(D)\mathrm{d}D, \qquad (3.3)$$

where the prefactors are related to the conversion of units, $Q_{\mathrm{ext}}(D)$ (mm^2) is the extinction cross section of a drop with volume-equivalent diameter D (mm) and $v(D)$ ($\mathrm{m\ s}^{-1}$) is its terminal fall velocity. The $v(D)$ relation used in this thesis will be that of *Beard* (1976), which is considered to be the most accurate parameterization of raindrop terminal fall velocity in still air available to date. For a 27 GHz signal, the wavelength ($\lambda \approx 11$ mm) is of the same order of magnitude as the size of the scattering particles (raindrops). Therefore Mie scattering theory (e.g. *van de Hulst*, 1957) must be used to compute $Q_{\mathrm{ext}}(D)$, which also depends on the rain temperature and the frequency of the signal. Although the T-matrix method by *Mishchenko and Travis* (1994) is the most comprehensive for the calculation of electromagnetic scattering by particles of arbitrary shape, this computationally intensive technique is not used here. Instead, for simplicity, the Mie series expansion for purely spherical particles is used. This assumption is justified because raindrop shapes deviate little from pure spheres when their volumes are small (*Pruppacher and Klett*, 1997), which is the case for drops occurring in moderate events in temperate climatic regions. The T-matrix method does become relevant when polarimetric measurements are considered, as the difference between the horizontally and vertically polarized received signals is due to the non-sphericity (oblateness) of the drops.

3.2.2 $k - R$ relation

As has been shown by many in the past (e.g. *Atlas and Ulbrich*, 1977; *Olsen et al.*, 1978), the $k - R$ relation can be approximated by a power law

$$k = a_* R^{b_*}. \qquad (3.4)$$

Figure 3.1 shows the k and R values calculated for a rain temperature of $T = 288.15$ K and at a frequency of 27 GHz using the 446 drop size distributions (where $R > 0.1$ mm h^{-1}) measured by *Wessels* (1972) in the period between January 3, 1968 and March 13, 1969 in De Bilt, The Netherlands. Two power laws are also shown in Figure 3.1, one resulting from the linear fit of $\ln(k)$ to
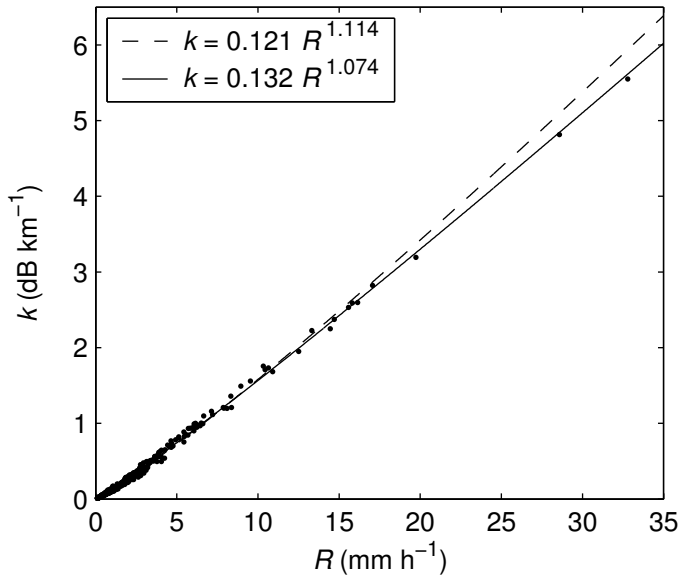
Figure 3.1: Specific attenuation as a function of rainfall intensity for the drop size data collected by *Wessels* (1972) for $T = 288.15$ K and a signal frequency of 27 GHz. Power law fits (dashed line: linear fit of the logarithms; solid line: nonlinear fit) to these data are also shown.

$\ln(R)$, and the other resulting from a non-linear power law fit of k to R. Both regressions were based on a least-squares criterium. It can be seen that the relation between k and R is nearly linear for these data, and that in any case the exponent of this power law relation is significantly closer to one than those of power law relations used for remote sensing of rainfall using weather radar (*Smith and Krajewski*, 1993). In the remainder of this chapter only non-linear least square fits will be used as these assign more weight to the higher rainfall intensities.

Olsen et al. (1978) list the coefficients and exponents of power law approximations of the relations between specific attenuation and rainfall intensity for different frequencies, temperatures and classically used drop size distribution climatologies. Table 3.1 gives the results of linearly interpolating the listed values of the coefficients and exponents for 25 GHz and 30 GHz, at rain temperatures of 263 K, 273 K and 293 K. The exponents in Table 3.1 are all relatively close to 1, also indicating a nearly linear $k - R$ relation.

The near-linearity of the $k - R$ relation for different drop size distributions is the result of the fact that the integrands of Eqs (3.2) and (3.3) have similar shapes. This implies that the $k - R$ relation should be nearly independent of the DSD. To demonstrate this, Figure 3.2 shows graphs of $g_k(D)$ and $g_R(D)$,

which are normalized versions of the integrands of Eqs (3.2) and (3.3)

$$g_k(D) = \frac{10^{-2}}{k \ln(10)} Q_{\text{ext}}(D) \tag{3.5}$$

$$g_R(D) = \frac{6 \times 10^{-4} \pi}{R} D^3 v(D). \tag{3.6}$$

Note that the shapes of these lines are independent of the DSD, as $N(D)$ is only used in the normalization. As a measure of the relative importance of the different regions of diameters, Figure 3.2 also shows the exponential drop size distribution

$$N(D) = N_0 e^{-\Lambda D}, \tag{3.7}$$

with $N_0 = 8000\,\text{m}^{-3}\,\text{mm}^{-1}$ (see *Marshall and Palmer*, 1948) and $\Lambda = 2.0\,\text{mm}^{-1}$ (corresponding to a rainfall intensity of $R = 34.2$ mm h^{-1}). This DSD has also been used to compute k in Eq. (3.5) and R in Eq. (3.6) for Figure 3.2.

From Figure 3.2, the conclusion can be drawn that the integrands are indeed similar for k and R for raindrop diameters between 0.1 and 4.0 mm, and that the region of drop sizes where they start to deviate is a region where $N(D)$ is negligible. This is the reason for the near-linearity of the $k - R$ relation. It can also be seen that the $Q_{\text{ext}}(D)$ and the $v(D)$ relations can be approximated by power laws (the graphs on log-log scales are nearly linear), and that the difference between the exponents of these power laws is approximately 3 (the slopes in the log-log graphs are nearly equal, see also Eqs (3.2) and (3.3)). *Atlas*

Table 3.1: Coefficients a_* and exponents b_* for different power-law relations between specific attenuation k (dB km^{-1}) and rainfall intensity R (mm h^{-1}) at 27 GHz (interpolated from *Olsen et al.*, 1978), for different rain temperatures and for different drop size distribution climatologies. LP$_L$: *Laws and Parsons* (1943) distribution for low rainfall intensities (1.27-50.8 mm h^{-1}); LP$_H$: *Laws and Parsons* (1943) distribution for high rainfall intensities (25.4-152.4 mm h^{-1}); MP: *Marshall and Palmer* (1948) distribution; J-T: *Joss et al.* (1968) distribution for thunderstorms; J-D: *Joss et al.* (1968) distribution for drizzle. Also shown are values of a_* and b_* calculated using the drop size distributions measured in De Bilt, The Netherlands by *Wessels* (1972) (W).

	$T = 263$ K		$T = 273$ K		$T = 293$ K	
	a_*	b_*	a_*	b_*	a_*	b_*
LP$_L$	0.132	1.078	0.128	1.081	0.135	1.063
LP$_H$	0.168	1.010	0.170	1.003	0.177	0.986
MP	0.153	1.054	0.147	1.062	0.153	1.051
J-T	0.215	0.863	0.213	0.860	0.218	0.847
J-D	0.116	0.994	0.103	1.037	0.094	1.117
W	0.125	1.104	0.126	1.097	0.135	1.066
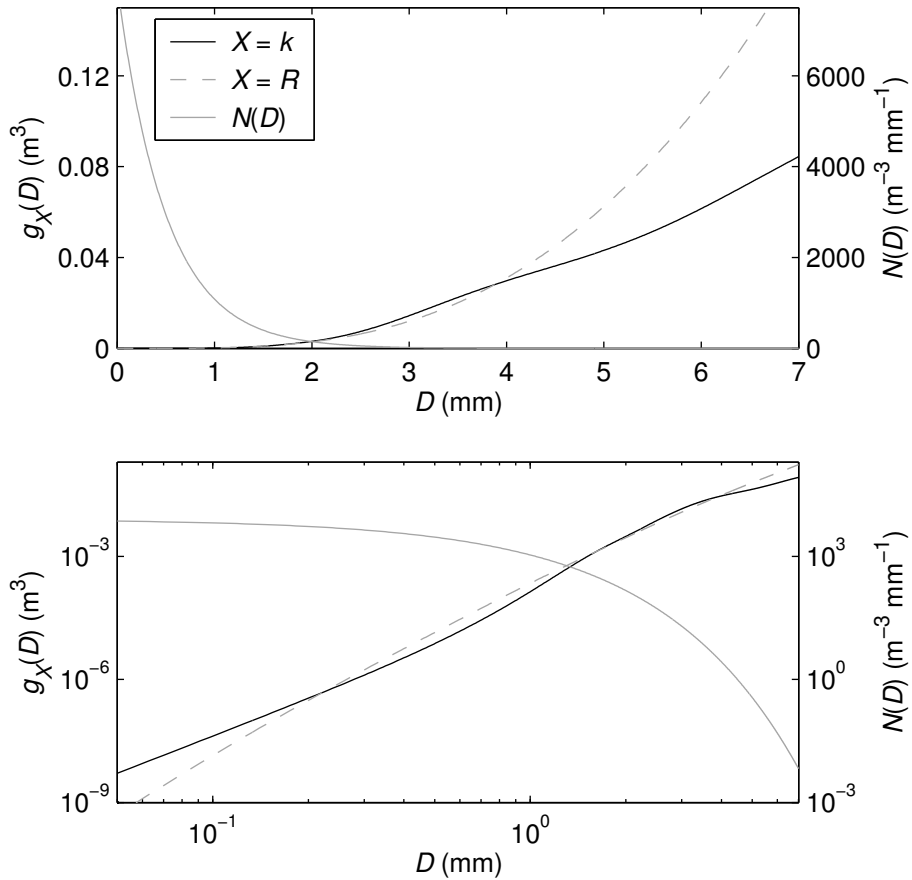
Figure 3.2: The normalized DSD-independent parts of the integrands of the integrals used to compute the specific attenuation and the rainfall intensity, on linear (top) and logarithmic (bottom) scales. Also shown in both graphs is the exponential DSD (with $N_0 = 8000$ and $\Lambda = 2.0$ mm^{-1}).

and Ulbrich (1977) based their conclusion that the $k-R$ relation is nearly linear on similar observations.

Because the extinction cross-section is temperature dependent, the analysis of Figure 3.1 can be repeated for different rain temperatures. The coefficients and exponents of the power law fits to the data of *Wessels* (1972) are plotted as a function of the temperature T in Figure 3.3. It can be seen that the ranges of values of both a_* and b_* are limited in the wide range of rain temperatures (263.15 K $\leq T \leq$ 313.15 K) shown here. Comparing the range of values of a_* and b_* to those listed in Table 3.1 leads to the conclusion that the temperature is not a very important factor in this analysis as compared to the DSD climatology. Furthermore, the exponent b_* is close to 1, so that the $k-R$ relation is
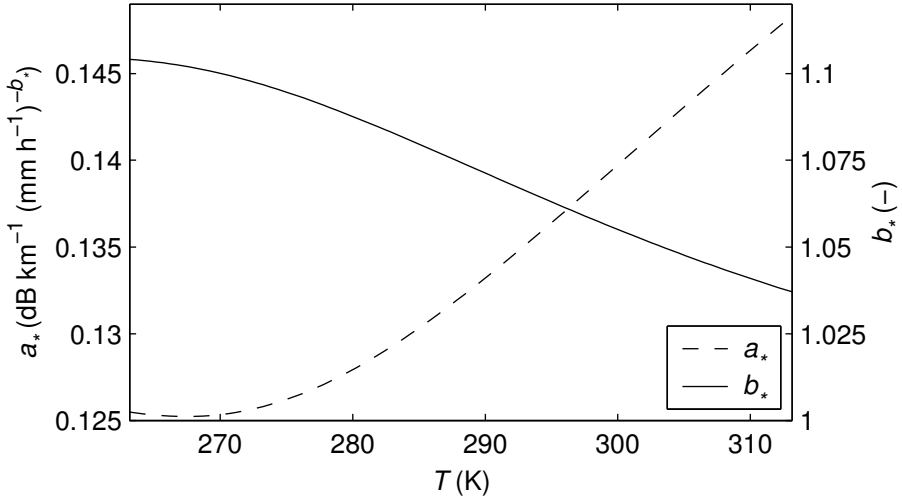
Figure 3.3: Temperature dependence of the coefficient a_* and exponent b_* of the power-law approximation of the $k - R$ relation for the drop size distributions measured by *Wessels* (1972).

nearly linear over this range of temperatures. It must be noted, however, that when the rain temperature drops below 273.15 K, the precipitation may be partly frozen, considerably changing the extinction coefficient $Q_{\text{ext}}(D)$. Frozen precipitation is outside the scope of this thesis, but it is important to realize that it can occur and significantly affect the $k - R$ relation.

An important result of the near-linearity of the $k - R$ relation ($k \approx cR$) is that the path-integrated attenuation A_{m} can be directly related to the path-averaged rainfall intensity $\overline{R}$ (see Eq. (3.1))

$$A_{\text{m}} = \int_0^L k(s)\mathrm{d}s \approx c \int_0^L R(s)\mathrm{d}s = cL\overline{R}.$$

In the remainder of this chapter, the $k - R$ relation based on the DSDs measured by *Wessels* (1972) (see Figure 3.1) will be used. This is done because it is assumed to be representative of the DSDs occurring in the Netherlands, where the experimental verification (see Section 3.3) was carried out. However, because the dependence of the $k - R$ relation at 27 GHz on the DSD is limited, this choice should not greatly influence the results.

3.3   Experimental verification

The same microwave instrument as the one used to verify the estimation of evaporation (see Chapter 2) was used in an experiment a year later to test its potential to estimate precipitation. The results of this experiment will be

presented in this section. The bars over $\overline{R}$ and $\overline{k}$ to denote path averages will be dropped in this section for simplicity of notation.

3.3.1 Experimental setup

An experiment with a 27-GHz microwave link was conducted between the towns of Rhenen and Wageningen (4890 m), The Netherlands (see Figures 1.2 and 3.4). In the period in which the experiment took place, from May 28, 1999 to July 23, 1999, over 120 hours of rainfall occurred in 25 separate events.

The microwave link was manufactured by the Eindhoven University of Technology, and on loan from the Horticultural Research Institute of New Zealand (*Green et al.*, 2000). The antennas of the system both have diameters of 0.6 m, and were mounted 46 m (transmitter) and 19 m (receiver) above the terrain. The received signal is fed through a logarithmic amplifier, after which it is low-pass filtered with a cutoff frequency of 10 Hz. The resulting signal is sampled at a rate of approximately 18 Hz. Hourly averages of meteorological variables like temperature and humidity were measured at the meteorological station of Wageningen University, operated by the Meteorology and Air Quality Group (see Figure 3.4).

A line configuration of seven tipping-bucket rain gauges was used to independently estimate path-averaged rainfall intenstiy. The manufacturer-supplied nominal tipping volume of the gauges is approximately 0.2 mm, which was verified by dynamic calibration after the experiment. Figure 3.4 shows the locations of these gauges relative to the microwave link signal path. The rainfall intensity measured by the gauges is averaged according to their distance to the nearest working neighbors or to the transmitter or receiver (see Table 3.2)

$$R = \sum_{i=1}^{N_{\mathrm{g}}} w_i R_i, \tag{3.8}$$

where R_i is the rainfall intensity measured by gauge i and N_{g} is the number of

Table 3.2: Period during which data are used and distance from the transmitter along the microwave link signal path s of the seven gauges (see Figure 3.4).

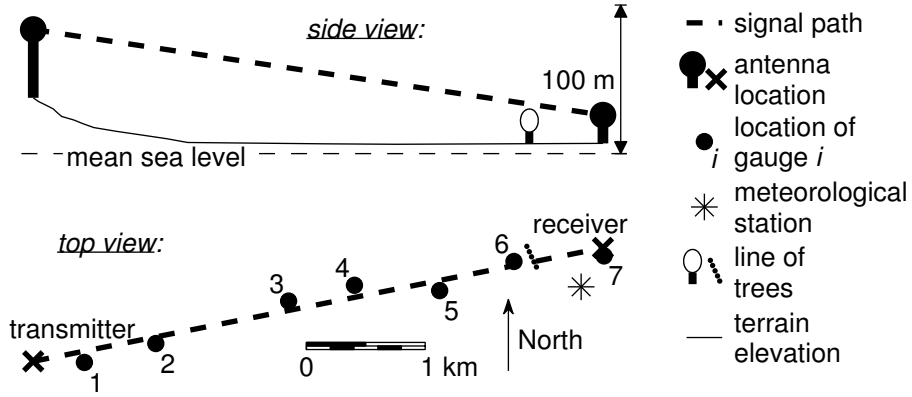| gauge	operational period	s (km)
1	29 May 1999 – 24 July 1999	0.43
2	29 May 1999 – 12 June 1999	1.03
3	none (vandalism)	2.20
4	29 May 1999 – 20 June 1999	2.73
5	18 June 1999 – 24 July 1999	3.46
6	24 June 1999 – 24 July 1999	4.14
7	29 May 1999 – 24 July 1999	4.89

Figure 3.4: Top- and a side view of the study area.

operational gauges. The weights of each of the operating gauges w_i is given by

$$w_i = \frac{1}{2L}\left(s_{i+1} - s_{i-1}\right), \tag{3.9}$$

where s_i is the position of gauge i, $s_0 = 2s_{\mathrm{tr}} - s_1$ (s_{tr} is the location of the transmitter), $s_{N_g+1} = 2s_{\mathrm{rec}} - s_7$ (s_{rec} is the location of the receiver) and L is the link length (note that $s_{\mathrm{tr}} = 0$ m and $s_{\mathrm{rec}} = L$). This average is assumed to be representative for the path-averaged rainfall intensity.

Figure 3.4 shows that a line of trees is located close to the signal path. This caused the signal to fluctuate due to reflections of the signal off the leaves and branches moving in the wind, masking the signal fluctuations caused by turbulent eddies moving through the signal path. Therefore, unfortunately, the data obtained in this experiment could not be used to estimate evaporation (see Chapter 2). Because the tops of the trees are just outside the frist Fresnel zone of the link, they do not affect the mean level of the signal and the experimental data can still be used for testing the potential of a microwave link for the estimation of precipitation.

3.3.2 Rain gauge measurements

The internal clocks of the different gauges were observed to be a little slow, so that precise timing of the onset of the rainfall events is not possible. However, the time signature of the events that occurred during the measurement period is not much affected by this. The gauge clocks are corrected manually by comparing the time indicated by the gauge to the actual time when the gauges were checked in the field during the experiment. It is assumed that the clock speed has not changed between these checks, so that the correction can be carried out by linear interpolation. The gauge results are then checked for each rainfall event against the other gauges and against the microwave link signal. If this timing adjustment is judged not to be accurate for a particular
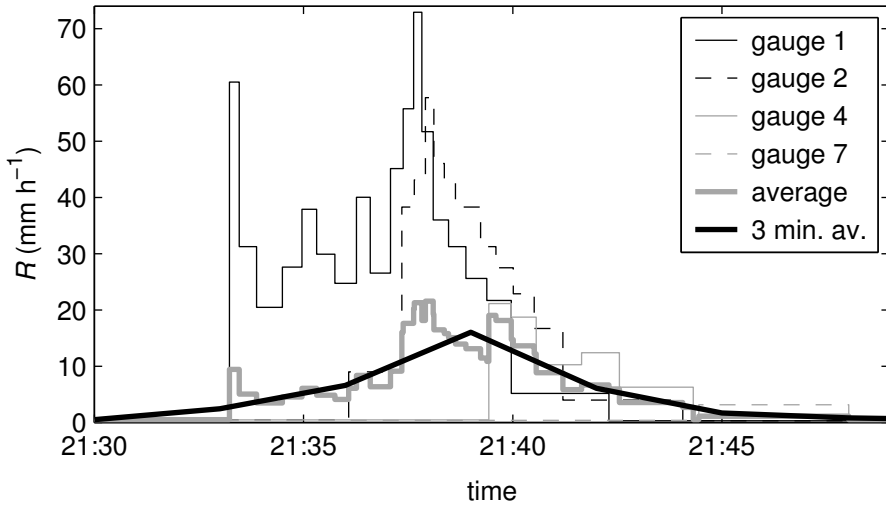
Figure 3.5: Time series of the rainfall intensities recorded by the gauges
operating on May 29, 1999. Also shown are the resulting weighted averages
and 3-minute averages of rainfall intensities.

gauge, the data of this gauge is disregarded for the event. Table 3.2 shows
the periods during which the data has been used for each of the gauges, along
with information of their positions along the signal path of the microwave link.
The uncertainty in the timing of the resulting averaged rainfall intensity is
estimated to be approximately 90 s, based on the typical magnitude of the
deviations between gauge clocks and the actual time at checks in the field.

Because of the uncertainty in the timing of the gauges, both the rainfall
intensity measured by the gauges and the signal attenuation measured by the
microwave link are averaged over 180 s (3 minutes). Figure 3.5 shows the time
series of the rainfall intensity of the individual gauges, the resulting weighted
averages and the 3-minute averages of rainfall intensities for a portion of one
particular event. It can be seen from this figure that the spatial and temporal
variability of the rainfall can be significant. Therefore, the average of the point
measurements of the gauges may not always represent the true path average of
the rainfall intensity.

3.3.3 Microwave link measurements

The absorption by atmospheric constituents is neglected here except for that
caused by water vapor. The signal is corrected for this using the relation given
by *Ulaby et al.* (1981, Ch. 5). The attenuation by water vapor k_{H_2O} is calculated
using hourly averaged values of atmospheric variables (linearly interpolated in
time) measured at the meteorological station (see Figure 3.4). The voltage

34

measured by the receiver V (V) is then corrected according to

$$V_Q = V - k_{\mathrm{H_2O}} L \left(\frac{\partial V}{\partial A_\mathrm{m}} \right), \qquad (3.10)$$

where $\frac{\partial V}{\partial A_\mathrm{m}} = -0.0573$ V dB^{-1} (A_m is the path-integrated attenuation) was obtained by laboratory calibration of the instrument. The subscript Q denotes that the voltage has been corrected for water vapor.

Other effects due to slowly varying atmospheric variables include anomalous propagation, multipath propagation, convergence/divergence of the beam, and reflection of the signal off discontinuities in the temperature or humidity profile or the terrain below the link (*Herben*, 1984). However, no profiles of the atmosphere were measured during the experiment, so that correcting this is not possible. *Herben* (1984) has shown that the effects of these phenomena are only important if the heights of the transmitter and receiver are nearly equal, so that this will not play a major role in this experiment. *Ruf et al.* (1996) show that the advantage of using the difference between the attenuation of signals at two different polarizations is that each signal propagates through the same atmosphere, and therefore the difference is not affected by factors other than rain itself.

Because the microwave instrument was manufactured as a scintillometer (see Chapter 2), no particular attention was paid to keeping the power of the signal stable over longer periods of time. This means, for example, that the gain of the amplifiers used may be temperature dependent. *Ruf et al.* (1996) argue that using a single location for the transmitter and the receiver with a corner reflector removes this problem, as the electronics used are all exposed to the same outside conditions. However, in this case, a temperature correction to the signal (derived during dry weather) for the amplifier gain had to be applied. The magnitude of this correction is determined using a linear regression on the hourly averaged corrected output voltage V_Q (V) measured during dry periods (i.e. at least one hour removed from any rainfall measured by the gauges). Figure 3.6 shows the result of the linear regressions on all data and on the data for which the hourly averaged relative humidity Q_rel (-) was smaller than 90%. The reason for this distinction is the fact that fog and wet antennas, which only occur at high relative humidity, may cause additional attenuation. It can be seen from Figure 3.6 that the results of both linear regression analyses are very similar, and that the scatter is significant (coefficients of determination r^2 are relatively small). The regression results for $Q_\mathrm{rel} < 0.9$ are used here for the temperature correction of the signal

$$V_{QT} = V_Q - c_1 - c_2 T, \qquad (3.11)$$

with $c_1 = -0.517$ V and $c_2 = 0.0101$ V K^{-1} (see Figure 3.6).

The results of these corrections to the signal in dry periods can be seen in Figure 3.7, where the probability density functions $f_V(V)$ of $V - \overline{V}$, $V_Q - \overline{V_Q}$ and V_{QT} have been drawn ($\overline{V}$ denotes the mean of V). It can be seen that the effect of the temperature correction is much more significant than that of
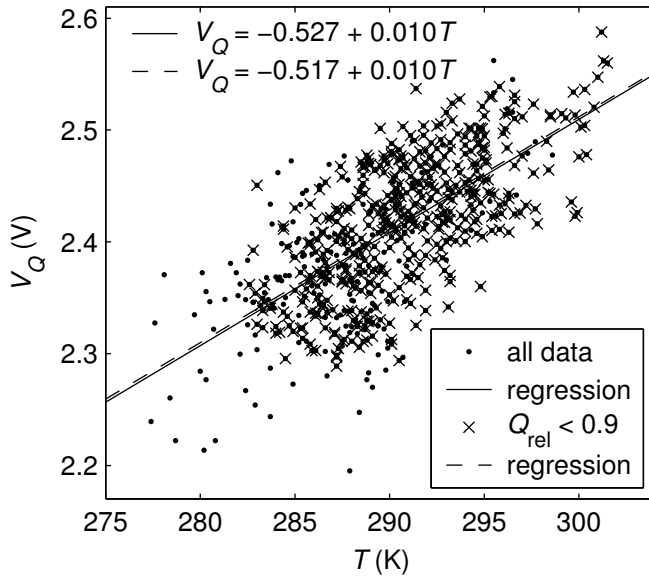
Figure 3.6: The hourly averaged humidity corrected output voltage V_Q measured during dry periods plotted against the hourly averaged temperature T. Regression ($V_Q = c_1 + c_2 T$) analyses shown are for all data (611 points): $c_1 = -0.527$ V, $c_2 = 0.0101$ V K^{-1}, $r^2 = 0.46$; and for the hours with $Q_{\mathrm{rel}} < 0.9$ (434 points): $c_1 = -0.517$ V, $c_2 = 0.0101$ V K^{-1}, $r^2 = 0.44$.

the water vapor attenuation correction. The specific attenuation k is estimated using this corrected voltage V_{QT} according to

$$k = \frac{V_{QT}}{L \left(\frac{\partial V}{\partial A_{\mathrm{m}}} \right)}. \tag{3.12}$$

3.3.4 Link-gauges comparison

The raingauge and microwave link data are divided into 25 separate events, starting 1 hour before and ending 1 hour after a rainfall event measured by any of the operating gauges. When 3 minute averages are taken, this yields 165 hours and 30 minutes (3310 points) of data, of which 119 hours and 54 minutes (2398 points) contain rainfall. Figure 3.8 shows the 3-minute averaged specific attenuation k as a function of the 3-minute averaged rainfall intensity R, with the power law estimated from Figure 3.1 ($a_* = 0.132$ dB km^{-1} (mm h^{-1})$^{-b_*}$, $b_* = 1.074$). It can be seen that the specific attenuation is larger than expected at low rainfall intensities. This may be explained by the fact that the water films on the antennas cause additional attenuation when they become wet, which has been shown by *Kharadly and Ross* (2001) to be a significant effect.
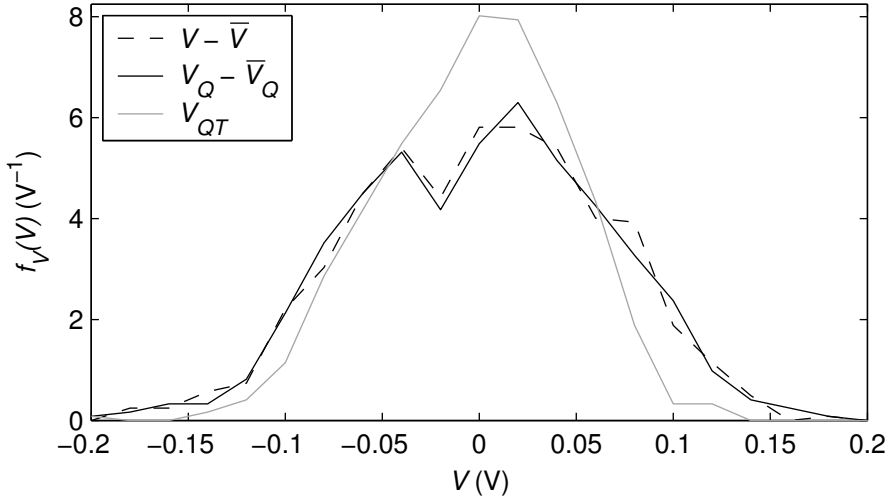
Figure 3.7: Empirical probability density functions $f_V(V)$ of the raw voltage V, the water-vapor attenuation corrected voltage V_Q and the temperature corrected voltage V_{QT}, where the first two are shifted by their respective means.

Wet antenna correction algorithms like that described by *Kharadly and Ross* (2001) and extended by *Minda and Nakamura* (2005) for slow drying of antennas can only be applied here by using the raingauge data because the antennas were not calibrated for water film attenuation. The attenuation caused by the wet antennas A_a (dB) as a function of the measured attenuation A_m (dB) and time is expressed by *Minda and Nakamura* (2005) as

$$A_a(t) = \max \left\{ \begin{array}{c} \min \left\{ \begin{array}{c} C_1(1 - \mathrm{e}^{-C_2 A_m(t)}) \\ A_{m(t)} \end{array} \right\} \\ A_a(t_0)\mathrm{e}^{-C_3(t-t_0)} \\ 0 \end{array} \right\}, \quad (3.13)$$

where t_0 (s) satisfies

$$\min \left\{ \begin{array}{c} C_1(1 - \mathrm{e}^{-C_2 A_m(t)}) \\ A_{m(t)} \end{array} \right\} < A_a(t_0)\mathrm{e}^{-C_3(t-t_0)}.$$

The first (top) part of the wet antenna attenuation function is the attenuation caused by the water films on the antennas during rainfall, and the second part (involving C_3) is that after or in decreasing rain due to the time it takes for the water films to disappear from the antennas. Least-squares fitting Eq. (3.13) to the residual $(k - a_* R^{b_*})L$, where $k \geq 0$, using the data of all the events, leads to such a high value of C_3 that the exponential decay in time does not play a role in practice given the 3-minute time step. This means that the wet antenna
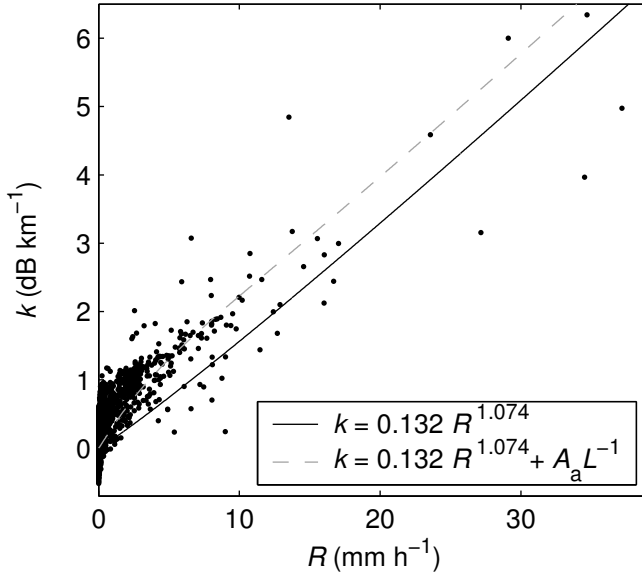
Figure 3.8: Comparison of the rainfall intensity measured by the gauges and the specific attenuation measured by the microwave link. Also shown are the power law obtained from Figure 3.1 and the result of the regression analysis of the wet antenna correction function (see Eq. (3.13)).

attenuation is independent of time, so that it can be plotted in Figure 3.8. The values of the other coefficients are $C_1 = 3.32$ dB and $C_2 = 0.48$ dB^{-1}, with a coefficient of determination for the regression of $r^2 = 0.65$ (values given by *Minda and Nakamura* (2005) are $C_1 = 5.0$ dB, $C_2 = 0.125$ dB^{-1} and $C_3 = 0.009$ s^{-1}, *Kharadly and Ross* (2001) give $C_1 = 8.0$ dB and $C_2 = 0.125$ dB^{-1}, and state that these values depend on the type of antenna). The resulting maximum wet antenna attenuation is 3.32 dB (i.e. limit for $A_m \to \infty$ in Eq. (3.13)). The maximum overestimation of the rainfall intensity can be computed by implicitly solving

$$\frac{d}{dR}\left(\left(R^{b_*} + \frac{A_a}{a_* L}\right)^{1/b_*} - R\right) = 0$$

using Eqs (3.4) and (3.13). This yields an overestimation of 3.9 mm h^{-1}, which occurs at $R = 11.6$ mm h^{-1}) if no wet antenna correction is applied. The measured attenuation can be corrected for the wet antenna attenuation using

$$A_c = \max\left\{\begin{array}{c} A_m - A_a \\ 0 \end{array}\right\}, \tag{3.14}$$

from which the corrected specific attenuation $k_c = A_c L^{-1}$ can be computed.

Figures 3.9 and 3.10 show time series of the attenuation, rainfall intensity

Figure 3.9: Measured attenuation (A_m), rainfall intensity and cumulative rainfall estimated from the link, compared to the rainfall measured by the gauges in the two bottom panels. Also shown is the wet antenna attenuation (A_a), and its correction (A_c), on May 29, 1999.

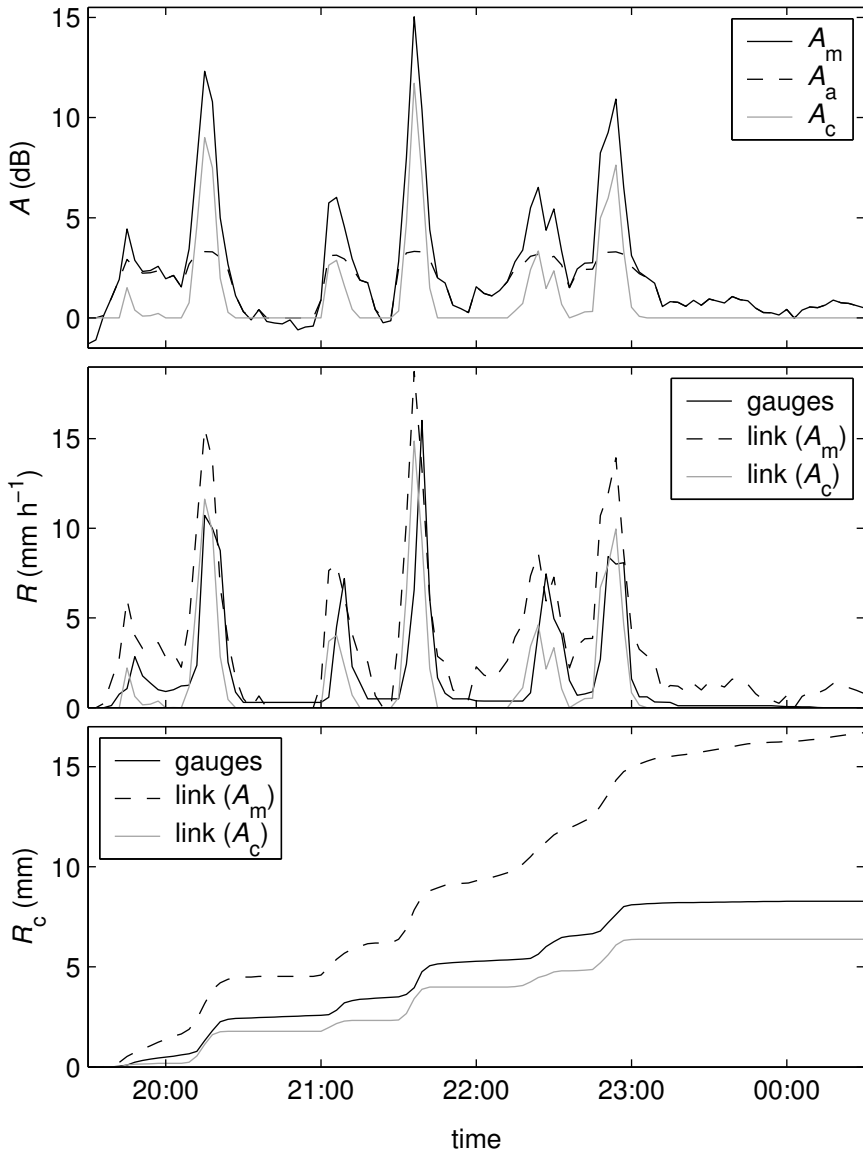**Figure 3.10:** Measured attenuation (A_m), rainfall intensity and cumulative rainfall estimated from the link, compared to the rainfall measured by the gauges in the two bottom panels. Also shown is the wet antenna attenuation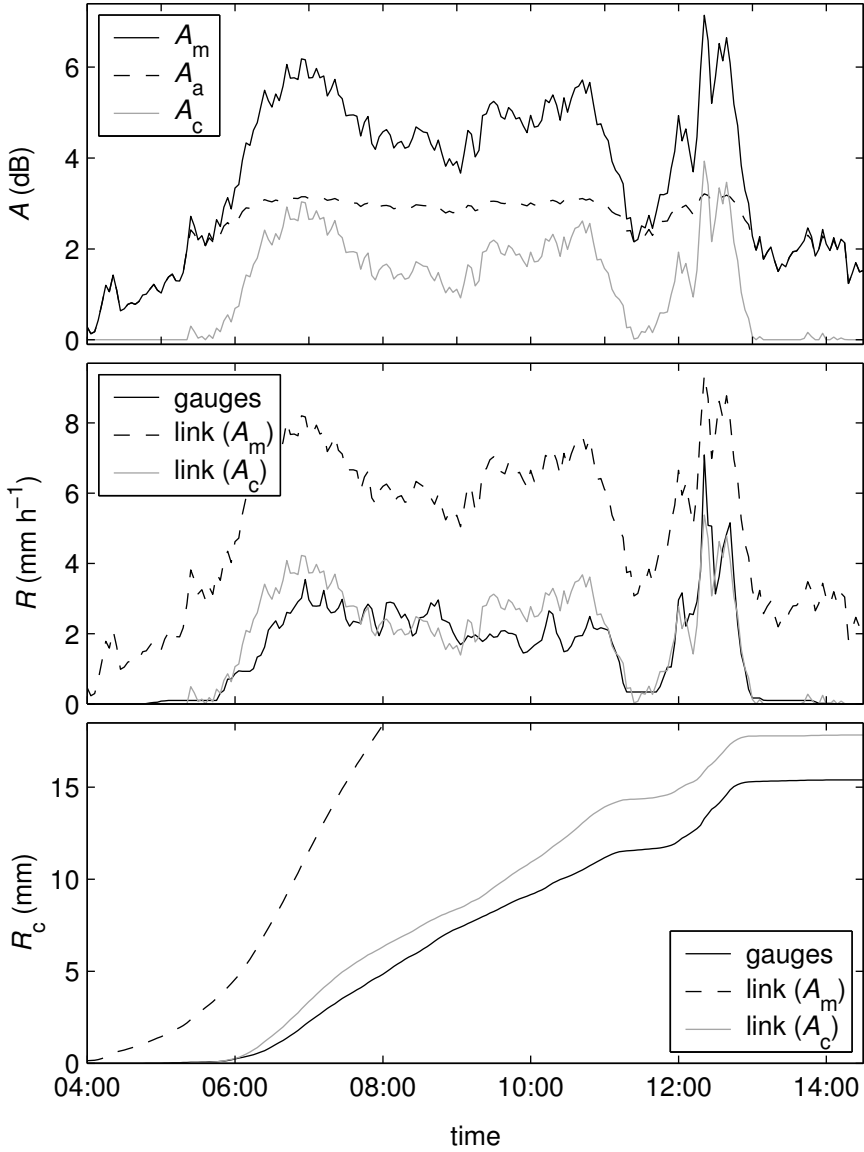 (A_a) and its correction (A_c), on June 5, 1999. The cumulative rainfall graph is truncated at 18.5 mm because the value for the uncorrected link rainfall at 14:30 is $R_c = 52.8$ mm.
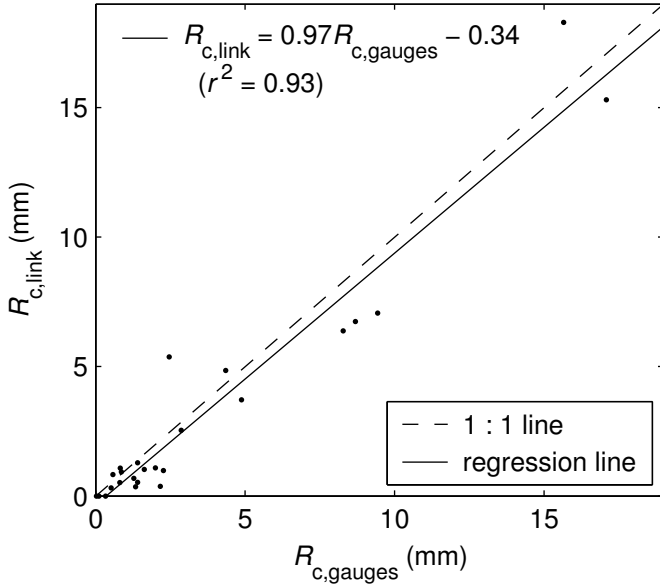
Figure 3.11: Comparison of the path-averaged cumulative rainfall for all 25 events estimated by the gauges $R_{c,gauges}$ and that estimated using the wet antenna-corrected microwave link signal $R_{c,link}$.

and cumulative rainfall R_c $(= \int R\mathrm{d}t)$ for two selected events, on May 29, 1999 and on June 5, 1999. The measured attenuation is shown along with the estimated wet antenna attenuation and the corrected attenuation to give an idea of the magnitude of this correction. For the two rainfall variables (bottom two panels in Figures 3.9 and 3.10), the microwave link estimate of the rainfall intensity with and without the wet antenna correction is compared to the gauges-estimated rainfall. It can be seen that the cumulative rainfall estimated by the link without taking into account the wet antenna attenuation is dramatically larger than that estimated by the gauges, especially for an event like that of June 5, 1999, where there is a long period of low-intensity rainfall (and hence a long period where the antennas are wet). Application of the wet antenna correction yields far better results. Because this wet antenna correction depends on the raingauge measurements, it could be argued that the rainfall intensity estimated using k_c and that estimated from the gauges are not independent. However, considering the fact that the wet antenna correction is based on only two parameters (C_3 does not play a role), fitted for the entire data set, the comparison does provide a good basis on which to test the potential of the instrument to measure precipitation. The dynamics of the rainfall intensity estimated by the gauges and by the link are seen to be very similar for these two events. Hence, it can be concluded that if the base level of the microwave link signal is known, the microwave link can estimate path-averaged rainfall at

a high temporal resolution relatively accurately. As mentioned before, the use of dual-frequency and/or dual-polarization links could significantly reduce the effect of the issue of variable signal base level.

Figure 3.11 shows the comparison of the total cumulative rainfall for all 25 events measured by the gauges and that estimated from the microwave link, in which the wet antenna attenuation correction was applied. The comparison is seen to be quite good (slope of the linear regression is 0.97, and coefficient of determination $r^2 = 0.93$), especially for higher accumulations. This again shows that a microwave link is well suited for measuring the path-integrated rainfall, in this case integrated over entire events.

3.4 Conclusions

The potential for a single-frequency, single polarization microwave link to measure path-averaged precipitation has been investigated. As shown by others in the past, the relation between the attenuation measured by the microwave link system and the rainfall intensity is seen to be nearly linear and nearly independent of the drop size distribution and the rain temperature at 27 GHz. A power law $k-R$ relation with coefficient $a_* = 0.132$ dB km^{-1} (mm h^{-1})$^{-b_*}$ and exponent $b_* = 1.074$ has been derived from more than a year of measurements of DSDs in The Netherlands, and has been used in this chapter.

Results of an experiment carried out in the summer of 1999 in the center of The Netherlands have been used to test whether a microwave link can be used to estimate precipitation. Analyses of data recorded by a microwave link system and a line configuration of seven raingauges show that it is extremely important to keep the electronics of both the transmitter and the receiver stable, and to either calibrate the antennas for wet antenna attenuation or (preferably) to avoid wetting of the antennas in the first place e.g. by using a roof.

The antennas have been calibrated for wet antenna attenuation using a relation from the literature and data recorded by the raingauges. The path-averaged rainfall intensity estimated using the resulting corrected specific attenuation is shown to represent that estimated by the gauges well, both in magnitude and in dynamics. From these results, it can be concluded that a microwave link can be used to measure precipitation if it is installed correctly. Combining this with the conclusions from Chapter 2, it can be stated that microwave links have great potential for measuring both evaporation and precipitation.

CHAPTER 4

Rainfall estimation using cellphone links

4.1   Introduction

Digital fixed radio systems, the type of wireless communication networks employed by commercial cellular communication companies, have recently been proposed as a cost-effective means for regional rainfall monitoring, complementing existing monitoring systems such as rain gauge networks and weather radars (*Messer et al.*, 2006). The number of links in commercial networks in The Netherlands ($\sim 35,000$ km^2) is approximately 12,000, with an average length of the links comprising these networks between 3 and 4 km, resulting in a density of approximately 1 km km^{-2}. This very high density offers great potential for the use of these systems in combination with the network of operational weather radars.

The fact that the propagation of radio waves in the atmosphere is hampered by rainfall along the signal propagation path has been known for a long time. Telecommunication engineers have studied the physical relation between radio wave attenuation and rainfall intensity since the 1960s (e.g. *Hogg*, 1968; *Semplak and Turrin*, 1969; *Crane*, 1971; *Olsen et al.*, 1978). Their objective was to establish statistical relations between the probability distribution of rainfall and that of attenuation for different climatologies and radio wave frequencies, in order to be able to predict the desired attenuation statistics from the relatively abundant rainfall statistics.

However, what is *noise* in telecommunication engineering can be considered

signal in the geophysical sciences. The idea of using the attenuation of radio waves to estimate rainfall intensities is certainly not new (e.g. *Atlas and Ulbrich*, 1977; *Jameson*, 1991; *Giuli et al.*, 1991; *Minda and Nakamura*, 2005). The employed rainfall retrieval method is based on measurements of the received signal level, estimation of the rain-induced attenuation, and the application of a power-law relation between attenuation and rain rate to estimate path-average rain rate (e.g. *Olsen et al.*, 1978). Recently, the development of dual-frequency radio links has given a boost to research in this area (e.g. *Rincon and Lang*, 2002; *Rahimi et al.*, 2003). Rainfall estimation based on microwave attenuation is also used in space-borne radar retrieval algorithms (e.g. *Meneghini et al.*, 1992). More recently, radio links have been suggested as tools to estimate both path-average precipitation and evaporation (see Chapters 2 and 3). The main objective of this chapter is to demonstrate the potential and discuss the limitations of *commercial* cellular communication links for rainfall monitoring (contrary to Chapter 3, where a research microwave link was used).

4.2 Methods and materials

4.2.1 Physical basis

Assuming the effects of multiple scattering to be negligible, the relative decrease in power between the source of a radio signal and a point in space (at a distance L from this source) due to attenuation by rainfall is given by (e.g. *Battan*, 1973)

$$\frac{P(L)}{P_0(L)} = \exp\left(-\frac{\ln(10)}{10} \int_0^L k(s)\mathrm{d}s\right), \tag{4.1}$$

where $P_0(L)$ is the received power without attenuation by rainfall, $P(L)$ is the received power and $k(s)$ (dB km^{-1}) is the specific attenuation due to rainfall as a function of the distance along the link s (km). $P_0(L)$ depends on the antenna size and radiation pattern, the transmit power and it decreases as L^{-2}. Measuring the signal power using a receiver at a distance L, the path-integrated attenuation (in dB) can be derived. The objective is now to estimate the average rainfall intensity over the total path of the link from the measured attenuation, using a relation between k and the rainfall intensity R (mm h^{-1}).

The specific attenuation k is a function of the extinction cross-section of the drops (and hence of the drop diameter) for the given frequency (see Eq. (3.2)), whereas R is a function of the drop volumes and velocities (see Eq. (3.3)). Through these size dependencies, both R and k depend on the drop size distribution in rain. At radio frequencies, scattering of electromagnetic waves off spherical raindrops can be computed using Mie theory (*van de Hulst*, 1957). If drop shapes deviate from spheres, the polarization of the electromagnetic signal becomes relevant. However, as this is a minor issue for small drops, which are most abundant (*Pruppacher and Klett*, 1997), it is assumed here that the drops are spherical. For the frequency employed in this chapter (38.530 GHz,
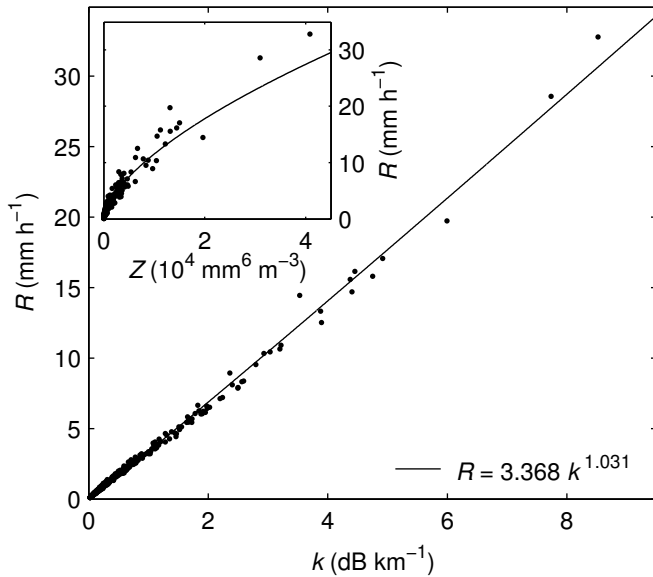
Figure 4.1: Non-linear fit of a power-law $R - k$ relation using the drop size data of *Wessels* (1972). The inset shows the relation between Z at C-band (5.6 GHz, the KNMI radar frequency) and R using the same drop size data, along with the power-law $R - Z$ relation used by KNMI.

see Section 4.2.2), 446 drop size distributions measured by *Wessels* (1972) during more than one year in The Netherlands (see also Chapter 3) have been used to fit a climatological power-law relation between k and R for Dutch conditions.

Figure 4.1 shows these data and a power-law $R-k$ relation obtained through non-linear fitting. The limited scatter of the data points around this power law shows that the coefficient of the power law $R = ak^b$ is relatively insensitive to the type of rainfall and the associated drop size distributions for Dutch circumstances. This is confirmed by the low value of the coefficient of variation (the ratio of the standard deviation and the mean) of a (assuming $b = 1.031$), $\mathrm{CV}_a = 0.15$, which is reduced to $\mathrm{CV}_a = 0.06$ if only those points with $R \geq 2$ mm h^{-1} are considered. Similar conclusions about the insensitivity to the drop size distribution have been drawn by e.g. *Atlas and Ulbrich* (1977) and *Olsen et al.* (1978). The scatter around the power-law relation between the radar reflectivity factor Z (mm^6 m^{-3}) and the rainfall intensity commonly used in radar rainfall estimation (inset in Figure 4.1) is much larger (a CV of the coefficient of 0.27 for all R and 0.23 for $R \geq 2$ mm h^{-1}, assuming a fixed exponent of 1.6) than that for the $R - k$ relation (see also *Battan*, 1973, table 7.1, pp. 90-92). In addition, the non-linearity of the point-scale $R - Z$ relation may cause considerable errors if it is used to estimate volume-averaged rainfall intensities, especially in variable rain. The fact that the $R - k$ power
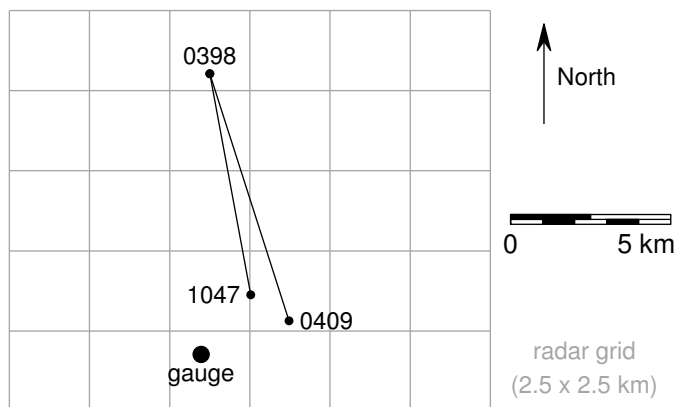
Figure 4.2: Locations of the antennas of the cellular communication links used (0398, 0409 and 1047) and the rain gauge.

law has an exponent that is very close to 1 justifies the use of this point-scale relation to compute line-averaged values of R from path-integrated values of k (see Eq. (4.1)).

Note that in this Chapter the fit of the $R - k$ power law was performed with k as the independent variable, as opposed to Chapter 3, where k was the dependent variable. In both cases (here and in Chapter 3), this makes little difference because the scatter of the data points is limited. However, in the remainder of this thesis, fits will be carried out with k as the independent variable, as this is the variable that is actually measured.

4.2.2 Cellular communication links

A set of two nearly parallel operational cellular communication links is located between the towns of Ede and Wageningen, The Netherlands. The signal levels of the receivers of these links have been recorded so that rainfall may be estimated from the signal attenuation. The two cellular communication links have one common antenna location (location 0398, see Figure 4.2), at which the signals are received. The other two antennas transmit at a frequency of 38.530 GHz and are located 7.75 km (antenna 0409) and 6.72 km (antenna 1047) to the south. Instantaneous values of the received signal level are recorded at irregular time intervals and only once or twice every 15 minutes. The power resolution is 1 dB, which may lead to significant rounding errors in low-intensity events. The transmit powers and radiation patterns of the antennas are not known, and therefore, an arbitrary reference level must be chosen. This is done objectively based on the mode of the histogram of the signal power over the full data set (including dry periods). The maximum value that the measured attenuation can attain, and hence the rainfall intensity, depends on the dynamic range of the receiver, the transmit power, the antenna pattern and

the length of the link (it decreases as $-20 \log_{10}(L)$ when given in dB). In this case the maximum measurable values of attenuation are 44 dB (link 0409-0398) and 41 dB (link 1047-0398), resulting in maximum measurable path-averaged rainfall intensities of 19.1 mm h^{-1} and 20.5 mm h^{-1}, respectively.

Data have been collected intermittently in the period between September 1, 2003 and December 7, 2003. Unfortunately, no data have been recorded during the most intense events. However, there are several events in the data set suitable for analysis, of which the eight most intense have been selected based on rain gauge and radar measurements.

4.2.3   Rain gauge and KNMI radars

Rainfall intensities estimated from the link data are compared to those measured by a nearby rain gauge and a composite of two C-band weather radars. The locations of the links and gauge are shown in Figure 4.2, and the locations of the radars can be seen in Figure 1.2. The rain gauge located near the two links measures the accumulated rainfall every 10 minutes by determining the water level in a vessel that is fed by a funnel with an orifice area of 400 cm^2. The accuracy of the gauge is reported to be better than 0.03 mm.

The two C-band (5.6 GHz) weather radars are operated by the Royal Netherlands Meteorological Institute (KNMI). They are located in De Bilt and in Den Helder (see Figure 1.2), covering nearly all of The Netherlands. Every 5 minutes, a map of radar reflectivity factors (Z) is constructed on a 2.5 km by 2.5 km grid. The relation employed to convert Z to R is the one used operationally by KNMI, $R = 0.0365 Z^{0.625}$ (i.e. $Z = 200 R^{1.6}$, *Marshall et al.*, 1955).

4.3   Results and discussion

Rainfall intensities that are representative for the two different links are computed from the radar map by weighted averaging of the pixels over the links. The weights are proportional to the distance of a link through the respective radar pixels. Figure 4.3 shows the comparison of the rainfall intensities measured by the gauge, the radars and those estimated from the signals of both links for the eight events considered. The radar-measured rainfall intensity in this figure is the average of the representative rainfall intensity for both links (rl, see the caption of Table 4.1). The order of magnitude and the dynamics (i.e. the variation with time) of the links, the radars, and the gauge are similar, which is a promising result.

4.3.1   Statistical analysis

Table 4.1 shows the squared correlation coefficients $r^2_{x,y}$ between the rainfall intensities estimated using the different methods (x and y) for each of the events. The $r^2_{x,y}$ values are calculated only with those points where at least one
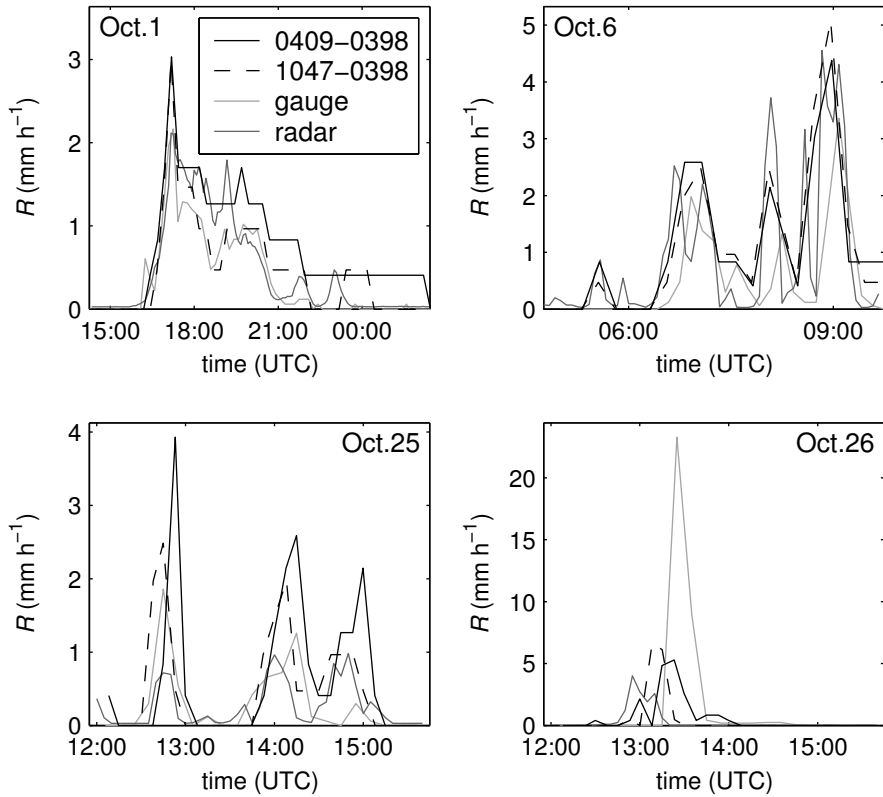
Figure 4.3: Time series of rainfall intensities estimated by the two links 0409-0398 (solid line) and 1047-0398 (dashed line) and that measured by the rain gauge (light gray line) and the radars (rl, see caption of Table 4.1, dark gray line) for the 8 selected events (continued on p. 49).

of the variables satisfies $R > 0.0$ mm h^{-1}. It should be noted that when the rain is highly variable in time, slight differences in timing can destroy correlations among signals.

Low values of $r^2_{\mathrm{rg,rl}}$ for the comparison of the radar rainfall estimates above the gauge and above the links are indicative of large spatial variations in the rain. Hence, in Table 4.1 the events are sorted according to increasing spatial variation. An important observation that can be made from Table 4.1 is that the values of $r^2_{\mathrm{rg,g}}$ for the comparison between radar and gauge are lower than those for other comparisons for several events, which may be explained by the large difference in sampling volume, and the significant height of the radar volume above the gauge. This discrepancy can be seen to become larger as the rain becomes more variable. When the spatial variation in rain is small, the links compare better to the gauge, whereas the comparison between the
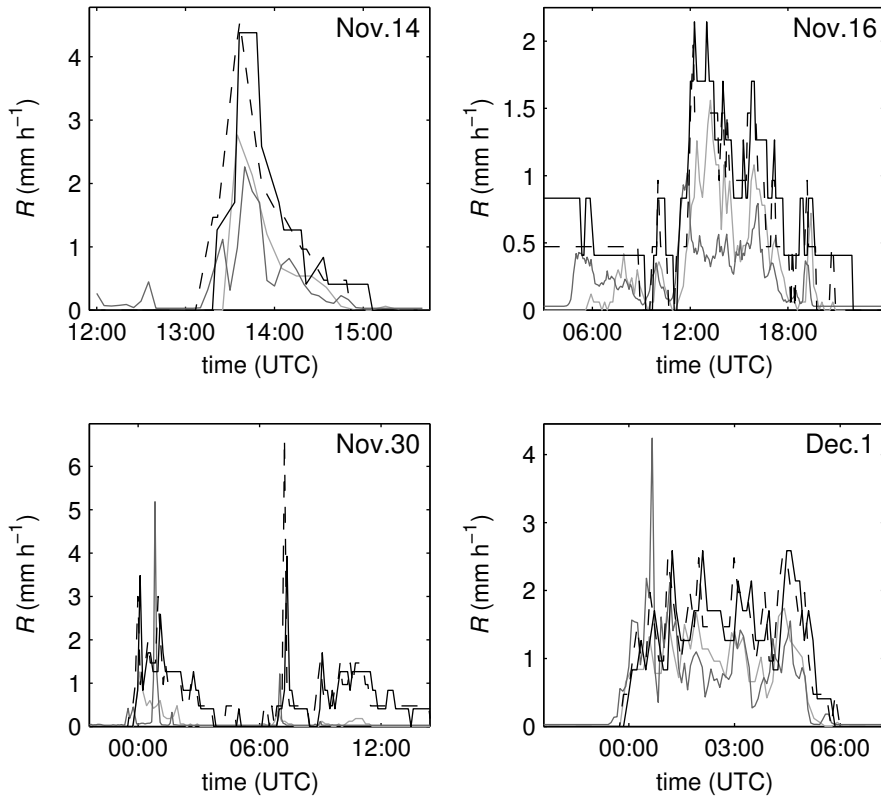
Figure 4.3: Continued from p. 48.

links and the radar is better when the rain is more variable. This is because in variable rain the weighted average of the radar pixels above the link provides a better representation of the path-averaged rainfall intensity than the point-scale gauge measurement. The high correlation coefficients of the comparisons between the links and the other instruments for relatively uniform events shows that the dynamics of the rain events is well represented by the links.

The rainfall intensities measured by the two near-parallel links are well-correlated, which is to be expected as the measurement principles are the same and their separation in space (antenna locations 0409 and 1047 are 1.44 km apart and the angle between the two links is 7.3°, see also Figure 4.2) is limited (limiting the differences due to variation in rain). Small differences (up to $\sim$0.5 mm h^{-1}) between the rainfall intensities estimated by the two links may be completely masked by the low (1 dB) resolution of the measurements. The relatively high values of r^2 for the comparisons of the links to other instruments for all of the events except the highly variable event of October 26 shows that cellular communication links are potentially useful for rainfall monitoring.

The event on October 26, 2003 shows large differences between the rainfall intensities measured by the different instruments, both in timing and in magnitude. This event was a convective event, which can generally be characterized by short-duration, high-intensity, and spatially highly variable rainfall. The explanation for the fact that the rain gauge measures much more rainfall than the links can be seen in Figure 4.4, which shows a map of radar reflectivities measured at the time of the peak of the rain gauge signal (13:20 UTC). The raingauge, located south of the paths between transmitters and receivers of the links, happened to be right in the trajectory of the small but intense rainfall peak.

The fact that the cellular communication links provide relatively direct (due to the near-linear relation) path-averaged estimates of rainfall intensities means that they are much less sensitive to the exact track of the storms than a rain gauge when it comes to providing a representative estimate of the rain rate. This is a major advantage of radio links over rain gauges. On the other hand, the low sampling frequency and the limited dynamic range of the commercial links under consideration in this chapter can cause link-estimates of rain accumulation to be less representative for these types of events. For example, a microwave link could miss the most intense part of a convective cell, as the duration of such events is typically much shorter than the sampling interval used with these links, or the attenuation is so high that the receiver cannot detect the signal. Convective events are the events where radar and link measurements may benefit most from one another. Radar has the advantage of

Table 4.1: Squared correlation coefficients $(r_{x,y}^2)$ of comparisons between different methods of rainfall intensity estimation for the 8 events (see Figure 4.3) sorted according to decreasing values of $r_{rg,rl}^2$, for all the events taken together (total), and for all events except October 26 (total*). The different methods of rainfall estimation x and y are: radar pixel above the gauge (rg), weighted average of radar pixels above link 0409-0398 and above link 1047-0398 (rl1, rl2, respectively), the average of rl1 and rl2 (rl), gauge (g), link 0409-0398 (l1) and link 1047-0398 (l2).

Event	$r_{rg,rl}^2$	$r_{rg,g}^2$	$r_{rl1,l1}^2$	$r_{rl2,l2}^2$	$r_{g,l1}^2$	$r_{g,l2}^2$	$r_{l1,l2}^2$
Nov. 14	0.75	0.79	0.52	0.67	0.78	0.83	0.96
Oct. 1	0.70	0.80	0.82	0.66	0.87	0.84	0.88
Nov. 16	0.63	0.43	0.44	0.30	0.64	0.72	0.75
Oct. 6	0.46	0.22	0.56	0.55	0.32	0.33	0.94
Dec. 1	0.23	0.18	0.25	0.29	0.73	0.71	0.90
Nov. 30	0.19	0.02	0.02	0.02	0.27	0.19	0.77
Oct. 25	0.09	0.29	0.67	0.55	0.52	0.46	0.75
Oct. 26	0.00	0.00	0.35	0.00	0.02	0.01	0.87
total	0.26	0.04	0.37	0.23	0.09	0.03	0.82
total*	0.50	0.35	0.37	0.32	0.57	0.48	0.82
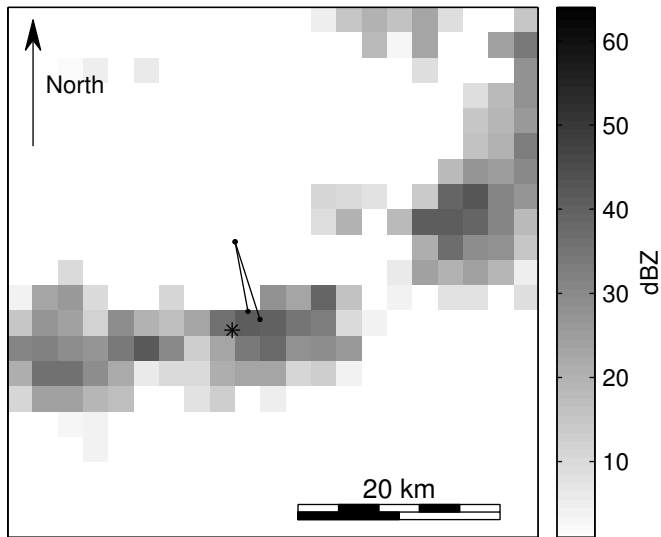
Figure 4.4: Areal representation of the radar reflectivity factor dBZ (= $10 \log_{10}(Z)$) measured by the KNMI radars on October 26, 2003 at 13:20 UTC, with the locations of the links and the rain gauge (see Figure 4.2).

higher spatial resolution, and the links have the advantage of more accurate measurement. In this sense link measurements could provide the correction for radars that rain gauges cannot provide due to their limited sampling area and their sparse density.

4.3.2 Limitations

It is apparent from Figure 4.3 that the links overestimate the rainfall intensities in most cases. This may be partly due to the uncertainty in the reference signal level, but is most likely the result of extra attenuation caused by the wetting of the antennas, which can cause several dBs of additional attenuation (see e.g. *Kharadly and Ross*, 2001, and Chapter 3). A correction can be applied when the antennas have been calibrated for this phenomenon (*Minda and Nakamura*, 2005), or if link and gauge or radar data with a sufficient dynamic range are available to calibrate an empirical correction algorithm, as was used in Chapter 3. Unfortunately, neither is the case, so that wet antenna attenuation correction is not possible here.

The effect of the uncertain reference signal level and the rounding error when using a power resolution of only 1 dB can be seen in Figure 4.5, which shows the effect of shifting the reference signal level by 0.5 or 1 dB (up or down) on the rainfall accumulation for the event of December 1, 2003. The rainfall intensity was set to zero if the estimated attenuation was negative in case of the negative shift of the attenuation. The effect of the shift in the reference
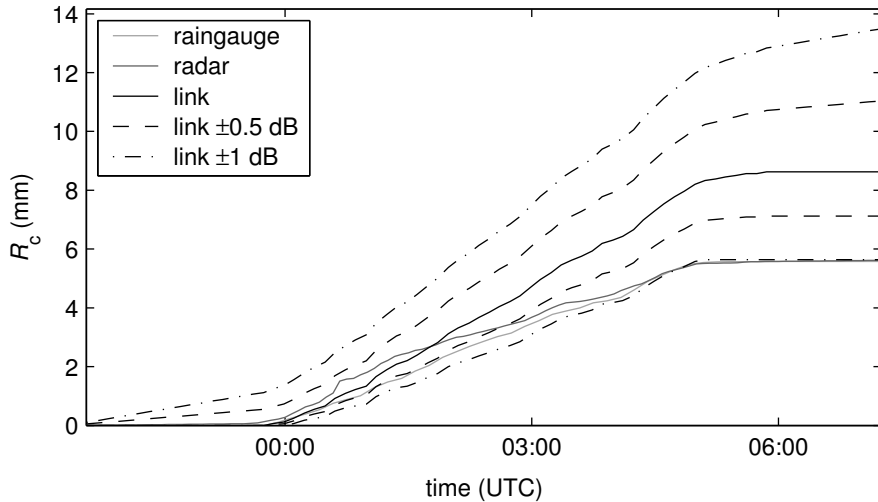
Figure 4.5: Time series of rainfall accumulation estimated from the link 1047-0398, with offsets in the reference signal level of 0 dB, ± 0.5 dB and ± 1 dB and that measured by the rain gauge (light gray line) and by the radars (dark gray line) for the event on December 1, 2003 (see also Figure 4.3).

signal level is seen to be major, especially for a long-lasting and low-intensity event like the one under consideration. Had the reference signal level been estimated to be 1 dB higher, the comparison of the link to the gauge and the radars would have been nearly perfect (Figure 4.5, lower dash-dotted line) in this particular case. Figure 4.6 shows that the total rainfall accumulations for most of the events considered in this chapter computed from the links with a negative offset correspond best to those measured by other instruments. This figure also shows the large errors in total accumulation that can occur because of a bias in the received signal level during long events. The consistently better results of the links with a negative offset suggest that there is an additional source of attenuation in rain, most likely wet antennas.

4.4 Conclusions

Microwave links such as those employed in cellular communication can potentially be used for the estimation of rainfall. The high density of these links in large parts of the world offers great potential for improving measurements of terrestrial rainfall. Two major reasons why radio links are a useful addition to weather radars for regional rainfall monitoring are (1) that they operate much closer to the ground (tens of meters as opposed to hundreds of meters to kilometers) and (2) that the relation between the observed quantity (rain-induced
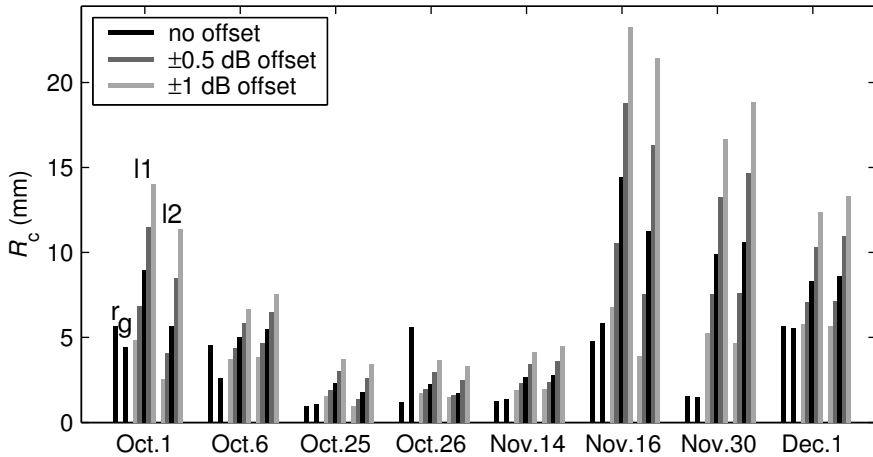
Figure 4.6: Total rainfall accumulations determined using different methods of rainfall intensity estimation for the 8 events (see Figure 4.3 and Table 4.1). The different methods of rainfall estimation are weighted average of radar pixels above both links (r), gauge (g), link 0409-0398 (l1) and link 1047-0398 (l2), both with offsets of 0 dB, ±0.5 dB and ±1 dB.

attenuation) and rain rate shows less scatter and is nearly linear for the employed radio frequencies (in contrast to the highly nonlinear radar reflectivity – rain rate relations). This near-linearity allows for upscaling of point-scale relations without serious problems.

Measurements made in the fall of 2003 with two radio links operated by a cellular communication company have been converted to rainfall intensities using relations derived from electromagnetic scattering laws and drop size distributions that are characteristic for The Netherlands. Comparisons of these rainfall intensities to those measured by a nearby rain gauge and by two C-band weather radars have yielded promising results. A statistical analysis shows that in relatively uniform rain, the links compare better to the gauge, whereas in variable rain the comparison between the links and the radar is better.

Before signals measured by cellular communication links can be used to estimate rainfall operationally, several improvements need to be implemented. The reference signal level needs to be known, so that the attenuation can be determined from the deviation of the signal from this level. The very coarse power resolution of the signals that have been used in this chapter (similar to that in *Messer et al.*, 2006) may cause large rounding errors, especially in long and low-intensity events. Sampling errors in events that are highly variable in time can easily be overcome by increasing the temporal sampling rate of the links. Finally, the antennas either need to be calibrated for wet antenna attenuation or they need to be shielded from rain.

Effects of the microstructure of rain

5.1 Introduction

Microwave links have been shown to be highly suitable for estimating path-averaged rainfall intensity (*Ruf et al.*, 1996; *Rincon and Lang*, 2002; *Holt et al.*, 2003; *Rahimi et al.*, 2003, 2004; *Minda and Nakamura*, 2005; *Krämer et al.*, 2005; *Upton et al.*, 2005; *Grum et al.*, 2005; *Messer et al.*, 2006, and Chapters 3 and 4). This is due to the near-linearity of the relationship between the variable measured by the link (the path-integrated attenuation A) and the rainfall intensity at certain link frequencies. The proximity of the measurements to the ground is an additional advantage with respect to other remote sensing techniques (e.g. weather radar). The availability of dense networks of such links used for cellular communication (Chapter 4 and *Messer et al.*, 2006) over most of the earth's land surface could potentially be used to greatly improve global rainfall estimation. The fields of hydrology and meteorology as well as agriculture, traffic management and climate modelling could benefit greatly from this improvement.

Rainfall attenuates electromagnetic signals travelling through the atmosphere. The magnitude of this attenuation varies with the rainfall intensity, which makes it a suitable quantity for rainfall estimation. Differences between two signals (with differing frequencies and/or polarizations) travelling through the same rain can also be used for this purpose, as long as the attenuations

experienced are significantly different. In this chapter both single- and dual-frequency links, with configurations involving both horizontal and vertical polarizations are studied numerically.

In order to be able to use microwave links for the estimation of rainfall, a number of issues such as wet antenna attenuation, temporal sampling, power resolution, and DSD variability need to be resolved (see Chapters 3 and 4). A research microwave link can be used to study these issues. One of the goals of this chapter is to study which frequency or combination of frequencies and what polarization configuration is optimal for this purpose. It is also important to characterize errors and uncertainties associated with many aspects of microwave link rainfall estimation. This is the second goal of this chapter. Errors and uncertainties related to canting angles of drops, rain temperature and the variation in drop size distributions (DSDs) are studied. The effect of different climatologies on the optimal frequency and/or polarization (combination) and on the errors and uncertainties caused by rainfall variability is investigated in this chapter by using DSDs from simulations based on intense Mediterranean rainfall.

Previous work on determining relations between rainfall intensity and specific (or differential) attenuation includes that of *Atlas and Ulbrich* (1977), who proposed the use of power laws between the two variables. *Olsen et al.* (1978) have provided tables of coefficients and exponents of these power laws for a range of different frequencies and three different temperatures. Different methods for rainfall estimation using microwave links (i.e., specific attenuation, polarimetric differential attenuation, dual-frequency differential attenuation and differential phase shift) have been studied by *Jameson* (1991) for a few frequencies or combinations of frequencies. *Holt et al.* (2003) have studied power-law relations for dual-frequency links, where a DSD parameter, the temperature and the drop shape were varied to investigate which frequency (combination) would be optimal for the estimation of rain. All of these studies have been done using parameterizations of DSDs.

Actually measured DSDs have been used by *Hendrantoro and Zawadzki* (2003) to compute power-law relations between specific attenuation and rainfall intensity. The present study presents more extensive analyses of the power-law relations between specific or differential attenuation, and is based on measured drop size data. The effects of drop canting angles, rain temperature and variations in DSDs are investigated separately so that the relative effect of each can be assessed. The dependence of link-estimated rainfall intensities on the interplay of variations in DSDs and the length of the link has been investigated by *Berne and Uijlenhoet* (2007). They only considered single-frequency single-polarization links, and the variation of DSDs was simulated (based on measured DSDs).

First, the method to compute specific attenuation and rainfall intensity from a DSD will be described in Section 5.2. Then, in Section 5.3, the employed drop size distribution data sets will be described. In Section 5.4, power-law relations will be derived for single- and dual-frequency links, for a range of frequencies and combinations thereof. The dependence of the specific attenuation on rain-

drop canting angles is also investigated, as is the dependence of the estimated rainfall intensity on the rain temperature. Measured time series of drop size distributions are used in Section 5.5 to investigate the effect of intra- and inter-storm variations of the microstructure of rainfall on microwave link-estimated rainfall intensities. In Section 5.6 some of the previous analyses are repeated using DSDs based on measurements of intense Mediterranean rainfall. Finally, the conclusions of this chapter are presented in Section 5.7.

5.2 Theory

An electromagnetic signal traveling through rain is attenuated by raindrops in its path. Neglecting the effect of multiple scattering, the total attenuation (in dB) of the signal due to rain is the sum of all of the attenuations caused by the individual raindrops, which depends on their extinction cross-sections. The extinction cross-section of a raindrop depends on its size, shape, orientation and temperature, and on the wavelength and polarization of the signal. Rainfall intensities, which depend on the sizes and fall velocities of the rain-drops, can be derived from measurements of the total attenuation A_{m} (dB) using semi-empirical relations between rainfall intensity R (mm h^{-1}) and specific attenuation k (dB km^{-1}) or differential attenuation Δk (dB km^{-1}) (e.g. *Atlas and Ulbrich*, 1977; *Olsen et al.*, 1978).

5.2.1 Electromagnetic scattering

Computations of scattering of electromagnetic waves by particles of arbitrary shapes are carried out here by using Waterman's T-matrix method (e.g *Waterman*, 1965; *Mishchenko et al.*, 1996). This method has been numerically implemented by *Mishchenko* (2000), whose code is freely available on the web[1]. From the elements on the diagonal of the amplitude scattering matrix produced by this code, the extinction cross-section Q_{ext} (mm^2) (e.g. *van de Hulst*, 1957) of a particle for both horizontally and vertically polarized waves can be computed. The frequency- and temperature-dependent complex refractive index of water that is needed for these computations is calculated using the relation given by *Liebe et al.* (1991).

The extinction cross-section is computed for particles that have generalized Chebyshev shapes. This shape is rotationally symmetrical about the vertical axis, and the distance from the center of the body to its edge a function of the angle θ with this axis of symmetry

$$d_{\mathrm{s}}(\theta) = \frac{1}{2}D \left[1 + \sum_{i=0}^{10} c_i \cos(i\theta) \right], \tag{5.1}$$

where D (mm) is the volume-equivalent drop diameter. The values of c_i have been obtained by interpolating the values given by *Chuang and Beard* (1990,

---

[1]http://www.giss.nasa.gov/~crmim/t_matrix.html

Table 1), who give these values as a function of the volume-equivalent drop diameter, with 0.5 mm intervals. As a comparison, oblate spheroidal shapes with axis ratios corresponding to those of the generalized Chebyshev particles described above have also been used. The particles can be canted and rotated so that the particles may be arbitrarily oriented.

5.2.2 Relation between R and k or Δk

Using knowledge about the relation between the size of a raindrop, its extinction cross section and its fall velocity, relations between the rainfall intensity R and the specific attenuation k or differential attenuation Δk can be derived. The specific attenuation will be referred to as $k_X(f)$, and the difference in specific attenuations for two different link settings (differential attenuation) will be called $\Delta k_{XY}(f_1, f_2)$. In these notations, which will be used throughout this chapter, X and Y indicate the polarization of the signal, which can either be H (horizontal) or V (vertical). The differential attenuation is given by

$$\Delta k_{XY}(f_1, f_2) = k_X(f_1) - k_Y(f_2) \tag{5.2}$$

Hence, to compute the differential attenuation, only two values of the specific attenuation are needed. Therefore, in the remainder of this section, only the specific attenuation will be considered.

For the computation of k_X and R it is of course necessary to have information about the distribution of drop sizes and the concentration of drops in the air, which can be described by a so-called drop size distribution (DSD) $N(D)$ (mm^{-1} m^{-3}). The specific attenuation and the rainfall intensity corresponding to this DSD can be computed (e.g. *Atlas and Ulbrich*, 1977) by

$$k_X = \frac{10^{-2}}{\ln(10)} \int_0^\infty Q_{\text{ext,X}}(D)N(D)\mathrm{d}D \tag{5.3}$$

$$R = 6\times10^{-4}\pi \int_0^\infty v(D)D^3N(D)\mathrm{d}D, \tag{5.4}$$

where $v(D)$ (m s^{-1}) is the terminal fall velocity of a raindrop as a function of its diameter. Using these two relations with a $Q_{\text{ext,X}}(D)$ (X again indicates the polarization) relation derived in Section 5.2.1, the $v(D)$ relation given by *Beard* (1976), and information about drop size distributions, relations between R and k or Δk can be obtained. *Atlas and Ulbrich* (1977) have suggested that relations between R and k_X should be power laws, which has been verified by many others (e.g. *Olsen et al.*, 1978, and Chapters 3 and 4). The same holds for relations between R and Δk_{XY} (e.g. *Holt et al.*, 2003). Here, such power-law relations will be used to derive (path-averaged) R from path-integrated k_X and Δk_{XY} as well.

5.3 Drop size data

Drop size distributions are commonly measured by disdrometers, which record the sizes (and sometimes fall velocities and drop shapes) of raindrops arriving on a horizontal plane in a given time interval. This may be done by e.g. measuring stains on filter paper (e.g. *Marshall and Palmer*, 1948), measuring the impact of drops on a surface (e.g. *Joss and Waldvogel*, 1967), measuring the magnitude and duration of the extinction of light caused by a raindrop (e.g. *Illingworth and Stevens*, 1987), measuring the position of the extinction of light with an array of cameras (e.g. *Schönhuber et al.*, 1994), or using the Doppler shift in an electromagnetic signal caused by falling raindrops (e.g. *Sheppard*, 1990). There may be large differences between DSDs measured by all of these disdrometers, which are caused by differences in measurement principles and/or different sampling areas or volumes. Another issue that is usually associated with disdrometers is sampling uncertainty. Because of the (usually) limited sampling area or volume, obtaining statistically robust measurements of DSDs is a challenge (e.g. *Tokay et al.*, 2005; *Uijlenhoet et al.*, 2006). Despite these limitations, measurements made by disdrometers are still valuable, and will be used here. Two types of disdrometers will be used in this study, one based on the filter paper technique (see Section 5.3.1) and one based on the extinction of light (see Section 5.3.2). A third data set consists of simulated DSDs (see Section 5.3.3).

5.3.1 De Bilt data

During more than a year (1968 and the first few months of 1969), drop size distributions have been collected by *Wessels* (1972) in De Bilt, The Netherlands (see Figure 1.2). This has been done using an instrument based on the filter paper technique for the measurement of drop sizes. By transporting filter paper under an exposure slit with an area of 20 cm^2, arrival times and drop sizes have been derived using the sizes of the stains left behind by the raindrops on the filter paper. Drop size distributions have been derived from these data by taking time periods in which *Wessels* (1972) judged the properties (e.g., intensity, drop size distribution) of the rain to be relatively constant, leading to time intervals between 1 and 50 min, with a mean of 8 min and a median of 5 min.

In this manner, 446 drop size distributions with rainfall intensities above 0.1 mm h^{-1} have been recorded in this period. Because the instrument was not designed to be outside continuously, it has only been operated when rain was expected or just after the start of an event. This may slightly influence the statistics of the measured DSDs. However, *Uijlenhoet* (1999) has shown that the distribution of rainfall intensities derived from the disdrometer closely follows the climatological distribution for The Netherlands. The small sampling area (20 cm^2) may also influence these statistics, as the measurement time interval should be rather large in order to collect enough drops. The resulting mean number of drops per DSD is approximately 850. As a consistency check,

the rainfall intensity computed using the derived DSDs has been compared to that measured by a nearby raingauge, yielding positive results. The distribution of rainfall intensities for these drop size data is shown in Figure 5.1. In the remainder of this chapter, this data set will be referred to as the De Bilt data set.

5.3.2   The BBC2 measurement campaign

The other data set used in this chapter has been collected during the BBC2 (second BALTEX BRIDGE Campaign, see e.g. *Crewell et al.*, 2004; *Simmer et al.*, 2004) measurement campaign. This campaign took place in May 2003 at the CESAR (Cabauw Experimental Site for Atmospheric Research) site in The Netherlands (see Figure 1.2). Drop size data have been collected using a 2D Video Disdrometer (2DVD, *Schönhuber et al.*, 1994), and additional wind data were collected as 10-minute averages at 20 m above the terrain.

The 2DVD estimates drop sizes, fall velocities and shapes through measurement of the extinction of light. Two sheets of light, located at a slight vertical distance, are emitted horizontally and then both sampled with two line-configurations of CCD sensors. The shapes (and hence sizes) of the particles falling throught the 100-cm^2 planes constructed in this way can then be determined by the number of CCD sensors that register a decrease in signal. The vertical velocity of the drop can be determined by the delay in signal between the two lines of CCD sensors. For additional details regarding the measurement principle of the 2DVD, the reader is referred to *Schönhuber et al.* (1994).

In principle, the 2DVD is able to measure drop shapes. However, because the 2DVD was not calibrated well enough to accurately measure drop axis ratios, this information has not been used in this study. Instead, the generalized Chebyshev approximation as described in Section 5.2.1 is used. Because some mismatching between the drop size and drop velocity measurements may occur (i.e., the velocity of one drop is assigned to another and vice versa), only those drops that have diameters and velocities that fall within a ± 40 % band of a theoretical $v(D)$ relation are used, as was suggested by *Thurai and Bringi* (2005). Again (as in Section 5.2.2 and Chapters 3 and 4), the $v(D)$ relation given by *Beard* (1976) is used for this purpose.

Because this disdrometer has a larger sampling area than that used in De Bilt (100 cm^2 versus 20 cm^2), the time over which DSDs can be computed can be smaller. However, the difference in sampling areas will introduce some difference in derived DSDs, as the effect of sampling is different in space than it is in time. Thorough discussion of this difference is outside the scope of this thesis, but it may play a role in the analyses carried out with these data. The sampling interval that has been used to derive point-scale relations between rainfall intensity and specific and differential attenuation is 30 s, where only those DSDs have been used where 50 or more drops have been measured. The resulting data set consists of 3139 DSDs, corresponding to more than 26 hours of rain. In the remainder of this chapter, this data set will be referred to as
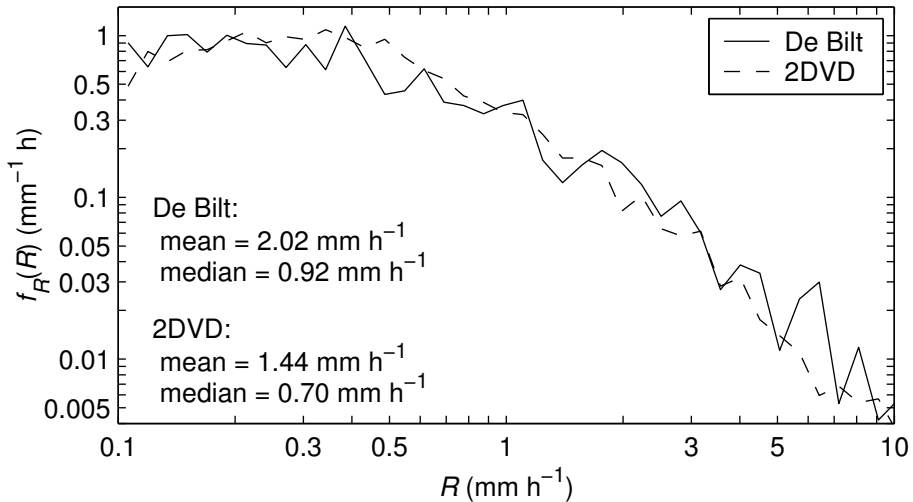
60

Figure 5.1: Probability density functions $f_R(R)$ of the occurrence of rainfall intensities R for the two DSD data sets. The R-axis is cut off at 10 mm h^{-1}.

the 2DVD data set.

Figure 5.1 shows the distributions of the rainfall intensities R for the two data sets. The two distributions seem to be similar, but there is a significant difference in mean, median and 90% quantile (4.69 mm h^{-1} for De Bilt and 3.19 mm h^{-1} for 2DVD) rainfall intensities. This difference is due to the different nature of the two instruments, and to the different measurement periods.

5.3.3 HIRE data

In order to have a preliminary look at the influence of the prevailing climatic conditions on the results described in the following sections, DSD data from the Mediterranean coast of France have been used. The DSD measurements have been collected during the Hydromet Integrated Radar Experiment (HIRE) that took place in the fall of 1998 in Marseille, France (*Uijlenhoet et al.*, 1999). In the Mediterraenan region, late summer/early fall is characterized by intense precipitation resulting from the interaction between the warm air from sea at low altitudes, the rugged topography of the coastal area and cold air in the upper troposphere (e.g., *Delrieu et al.*, 2005). In particular, the most intense part of the rain event of the 7 September 1998 is considered here. During this 45-min period, the mean rain rate was about 40 mm h^{-1} and the amount of rain was about 31.5 mm. DSD spectra have been measured by an optical spectropluviometer (*Salles et al.*, 1998) with a sampling area of 50 cm^2.

Using the DSD model proposed by *Berne and Uijlenhoet* (2005), 25-km long profiles of the two parameters of exponential DSDs (*Marshall and Palmer*,

1948) have been generated at 250-m resolution. These profiles are statistically homogeneous and correspond to the intense Mediterranean precipitation described above. First, 1000 profiles with no spatial autocorrelation have been generated in order to estimate the coefficients and exponents of the climatological point-scale power-law relations. Then 1000 profiles with the autocorrelation fitted on DSD data have been generated to investigate the influence of the variability of the DSD along the link. This data set will be referred to as the Marseille DSD simulations in the remainder of this chapter.

5.4   Point-scale relations

The relation between specific or differential attenuation and rainfall intensity depends on the frequency and polarization used, the temperature, the drop size distribution, the velocities of the drops, and the shapes of the drops. In this section the extent to which a power-law relation between these two variables exists in different settings is investigated, as well as the sensitivity of the coefficient and exponent of such a power law to assumed drop velocity and shape, to the temperature and to the frequency and polarization that is used. Using this information, the optimal settings for a microwave link operating under given conditions can be determined. These analyses are somewhat similar to those presented by *Holt et al.* (2003), but they are more general and analyze the effects of each of the parameters (e.g. temperature) separately. An important difference with regard to *Holt et al.* (2003) is that only measured drop size distributions are considered here. Drop size distributions presented in Section 5.3 will be used for these analyses, in particular those measured in De Bilt (Section 5.3.1).

The specific attenuation at horizontal and vertical polarization is computed using the T-matrix code as described in Section 5.2. As a comparison, the Mie series expansion (e.g. *van de Hulst*, 1957) has been used to compute specific attenuation for spherical drops. Power-law relations

$$R = ak^b \tag{5.5}$$

$$R = a_\Delta \left(\Delta k\right)^{b_\Delta} \tag{5.6}$$

have been fitted to these data using a least squares criterium. Unlike many cases of power-law fits, this fit has not been carried out in logarithmic space, as this type of fit would place an undesirable emphasis on smaller values, but rather in linear space.

For the estimation of path-averaged rainfall intensities using measurements of path-integrated attenuation, two criteria for the values of a, a_Δ, b, and b_Δ can be stated. For the relation to hold at multiple scales, it is desirable that the relation is close to linear. This is because it is derived using point scale drop size measurements, and applied for line-integrated attenuation measurements. This means that the exponent b or b_Δ should be close to 1. It is also desirable that the method is sensitive to the rainfall intensity (i.e. if R changes, k or Δk

should also change noticably). This means that the coefficient a or a_Δ should be small. However, if a becomes too small, the signal may become so weak in rain that it cannot be detected by the receiver. Because values of a and a_Δ that are close to 0 are of interest here, a^{-1} and a_Δ^{-1} will be displayed in graphs in the remainder of this section.

Before coefficients and exponents of power laws are computed, the effect of canting of raindrops on $k_X(f)$ and $\Delta k_{HV}(f, f)$ will be investigated.

5.4.1 Effect of canting angle distribution

Drops are not all oriented with their axis of symmetry vertically. The angle over which they are canted depends mostly on the vertical gradient of the horizontal wind velocity and on the intensity of the turbulence. Here, it is assumed that the canting angle is normally distributed (*Russchenberg*, 1992) with a mean of $5°$ and a standard deviation of $10°$. The mean and variance of the extinction cross-section of each drop are computed from 500 random samples of the canting angle drawn from this normal distribution. This analysis is done twice, once for drops canted perpendicular to the propagation direction and once for drops canted parallel to the propagation direction. Differences in results should give an indication of the uncertainties related to the canting angles of the drops.

The results obtained from these computations (i.e., 500 realizations per DSD) have been used to calculate means (μ_{k_H}, μ_{k_V}) and variances ($\sigma^2_{k_H}$, $\sigma^2_{k_V}$, $\sigma^2_{(\Delta k_{HV})}$) of the specific and differential attenuation for each of the 446 drop size distributions measured in De Bilt (see Section 5.3.1). Using these results, the uncertainty related to the distribution of canting angles and the error committed if it is assumed that drops are not canted are analyzed. For this purpose, the means and 10% and 90% quantiles are computed of (1) the coefficient of variation

$$CV = \frac{\sigma}{\mu} \tag{5.7}$$

and (2) of the relative difference between the mean specific attenuation and that assuming no canting ($k_{H,nc}$, $k_{V,nc}$, $\Delta k_{HV,nc}$)

$$\delta k = 1 - \frac{k_{nc}}{\mu_k}. \tag{5.8}$$

The 90% quantiles of the coefficients of variation where a single polarization has been used (CV_{k_H}, CV_{k_V}) are all well below 0.25%. The absolute values of the means and 10% and 90% quantiles of δk_H and δk_V are all below 0.1%. Hence, when a single polarization is used, uncertainties and errors due to canting angles are negligible. However, when using the differential attenuation, this may not be the case. Values of $\delta \Delta k_{HV}$ are nearly constant with frequency and nearly independent of the DSD (mean and the two quantiles are very close). For canting parallel to the propagation direction, $\delta \Delta k_{HV} \approx -0.6\%$, and for canting perpendicular to the propagation direction $\delta \Delta k_{HV} \approx -1.1\%$. These systematic errors are somewhat more serious than for single polarization, but are still limited. The uncertainty related to the canting angle distribution for
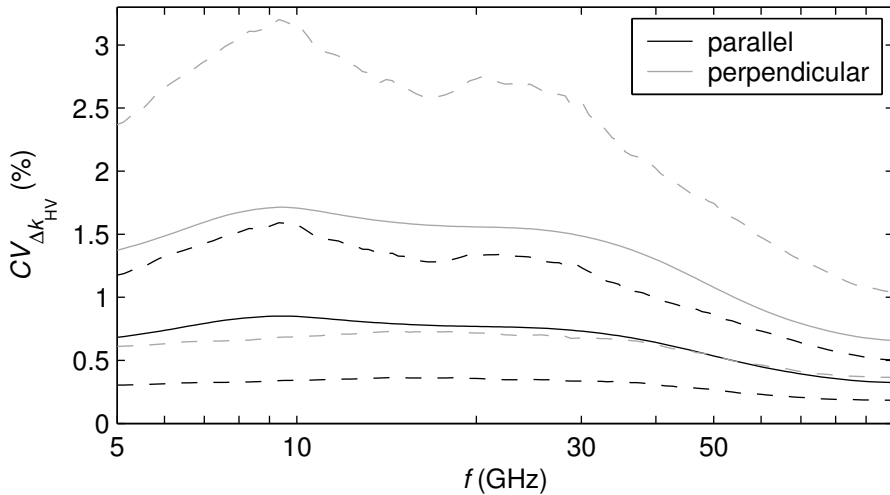
Figure 5.2: Mean (solid lines) and 10% and 90% quantiles (dashed lines) of $CV_{\Delta k_{HV}}$ as a function of frequency. Effects of canting parallel (black) and perpendicular (gray) to the propagation direction are shown.

dual polarization measurements (i.e., $CV_{\Delta k_{HV}}$) for the two canting directions is shown in Figure 5.2. It can be seen from this figure that the uncertainty can be a few percent, depending on the frequency and the DSD. In conclusion, the uncertainties and errors related to the canting of raindrops are small, and will be neglected in the remainder of this chapter.

5.4.2 Single-frequency links

The power-law coefficients and exponents of the fitted relations between the rainfall intensity and the specific attenuation at horizontal and vertical polarizations for both the De Bilt and the 2DVD data, as well as those resulting from Mie calculations and those given by *ITU-R P.838-3* (2005), are shown as a function of the signal frequency in Figure 5.3 (left). The coefficients and exponents of the power-law relations between R and $\Delta k_{HV}(f, f)$ are also shown in this figure (right).

Analyses show that for single polarization, the difference between the power-law constants for oblate spheroids and those for generalized Chebyshev raindrops is negligible. This was also concluded by *Czekala et al.* (1999). Therefore the results for oblate spheroids are not shown. The right part of Figure 5.3 shows that this difference is also small for dual-polarization differential attenuation, especially at low frequencies. This is probably due to the fact that small drops dominate in Dutch climate, and the deviation between oblate spheroids and Chebyshev particles is very small for such drops.

It can be seen from Figure 5.3 that the differences between the values of a
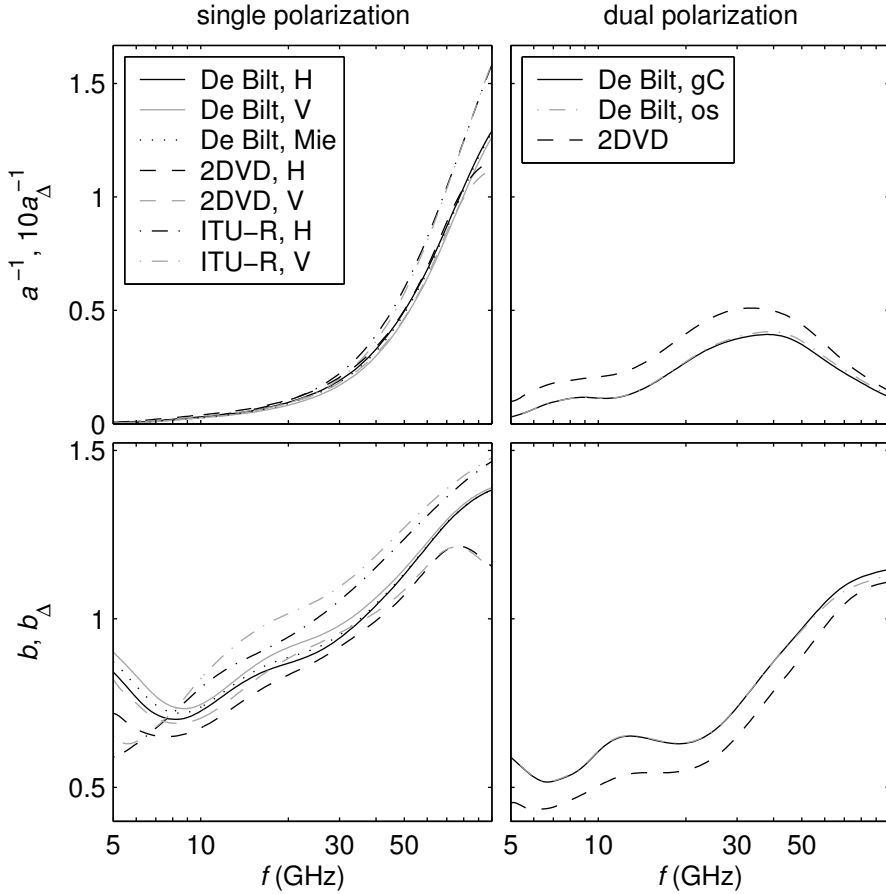
Figure 5.3: Results of fitting $R - k_{\mathrm{X}}$ (left) and $R - \Delta k_{\mathrm{HV}}$ (right) power-law relations for single-frequency links, for two Dutch data sets (De Bilt and 2DVD). Values of a and b (single polarization only) recommended by *ITU-R P.838-3* (2005) are also shown. Note that the legends of the top graphs also apply to those below. For dual-polarization measurements, results for oblate spheroidal (os) and generalized Chebyshev (gC) shaped drops are shown.

and b computed from the De Bilt and 2DVD data sets and those given by *ITU-R P.838-3* (2005) are quite large, larger even than the differences between horizontal and vertical polarizations. This difference may be due to several factors (e.g., different DSD climatologies, different fitting criteria, etc.), which cannot be determined as the methods used to determine values of a and b are not given by *ITU-R P.838-3* (2005). The difference in a and b between the two Dutch data sets is much smaller, except at very high frequencies ($f > 70$ GHz).

This deviation at high frequencies may be due to the fact that the 2DVD data set has more large drops for events with large R. These large drops are approximately the same size as the wavelength at these high frequencies, so that resonance effects may play a role here.

The values of a^{-1} can be seen to monotonically increase (i.e., a decreases) with frequency in the range under consideration, which is to be expected as it is widely known that radio signals suffer more from attenuation in rain as their frequency increases. In this frequency range, values of b are relatively close to 1, especially between 15 and 40 GHz.

For differential attenuation, there is a clear difference between the results obtained using the two different data sets, but the trends are similar. There is a peak in sensitivity (a_Δ^{-1} has a maximum) around 40 GHz. This may be due to resonance effects for larger drops, which dominate the differential attenuation (due to their relatively large deviation from spherical shapes). This peak in sensitivities nearly coincides with the occurrences of $b_\Delta = 1$ (between 50 and 60 GHz), which means that both a_Δ and b_Δ are approximately optimal at similar frequencies. The low sensitivity for differential attenuation (a_Δ^{-1} is small compared to the values of a^{-1} for specific attenuation) make this method potentially less useful, as was also noted by *Jameson* (1991). However, *Ruf et al.* (1996) note that because two signals (with equal frequencies) will suffer from the same atmospheric noise and wet antenna attenuation these sources of error do not affect the difference of the two signals, which is a great advantage. If the criterium that b or b_Δ should be as close to 1 as possible is used, the optimal frequencies are given in Table 5.1 for the data considered in Figure 5.3.

In order to analyse the quality of the fitted power-law relations, mean bias errors (MBE) and bias-corrected root mean square errors (RMSE) are com-

Table 5.1: Optimum frequencies and their corresponding values of a (mm h^{-1} dB^{-b} km^{b}) or a_Δ (mm h^{-1} dB$^{-b_\Delta}$ km$^{b_\Delta}$) for single-frequency links.

	f (GHz)	a or a_Δ	norm. MBE (%)	norm. RMSE (%)
De Bilt, H	35.9	3.74	3.2	10.8
De Bilt, V	32.5	5.03	2.7	9.3
De Bilt, Mie	35.3	4.00	3.0	10.3
De Bilt, HV	53.5	30.74	6.6	17.0
2DVD, H	40.6	2.88	0.5	23.1
2DVD, V	36.7	3.80	0.5	20.0
2DVD, HV	63.0	30.55	4.3	28.2
ITU-R, H	24.9	6.42	N/A	N/A
ITU-R, V	18.3	12.60	N/A	N/A

puted

$$\text{MBE} = \frac{1}{N_\text{s}} \sum_{i=1}^{N_\text{s}} \left(a k_i^b - R_i \right) \tag{5.9}$$

$$\text{RMSE} = \sqrt{\frac{1}{N_\text{s}} \sum_{i=1}^{N_\text{s}} \left(a k_i^b - R_i - \text{MBE} \right)^2}, \tag{5.10}$$

where N_s is the total number of DSDs used. In later sections in this chapter $a k^b$ may be replaced by $a_\Delta (\Delta k)^{b_\Delta}$, depending on the method used (single or dual polarization/frequency). Figure 5.4 shows the mean bias errors (MBE) and bias-corrected root mean square errors (RMSE), both normalized by the average rainfall intensity (i.e. $\frac{1}{N_\text{s}} \sum_{i=1}^{N_\text{s}} R_i$). The temperature in these analyses was taken to be 288.15 K (15°C). The MBE is an indicator of systematic under- or overestimations of rainfall intensities at the point scale, and the RMSE indicates the uncertainty related to variability in the shape of DSDs and to the use of deterministic power-law $R - k$ and $R - \Delta k$ relations. Values of normalized MBE and RMSE are also given for the optimal frequencies in Table 5.1. Note that because the sum of squared differences was minimized to fit the $R - k$ power laws, the mean bias error is not automatically zero (i.e., the MBE is not the variable that is minimized).

The differences in errors (MBE) and uncertainties (RMSE) between the two data sets is probably due to the differences in sampling between the two instruments. The consistently larger RMSE in the results using the 2DVD data is likely due to the shorter sampling interval that is used. For single polarization, the errors and uncertainties can be seen to be small at the frequencies where b is close to 1. This means that this frequency range meets all criteria for optimality for single-frequency single-polarization links.

For dual-polarization links, there is a significant underestimation (i.e., the MBE is significantly smaller than 0) in the range of frequencies where b_Δ is close to 1. The sensitivity to DSD variability (i.e., the uncertainty) is limited at these frequencies.

5.4.3 Dual-frequency links

Dual-frequency links act like single-frequency links when the two frequencies are very far apart, as the sensitivity of one signal to rain is much larger than that of the other (see Section 5.4.2), and hence the insensitive signal contributes negligibly to the differential attenuation. On the other hand, if the frequencies are too close to each other, differential attenuation may become too small to accurately estimate rainfall intensity, especially for equally polarized signals (equal frequencies and different polarization links have been discussed in Section 5.4.2).
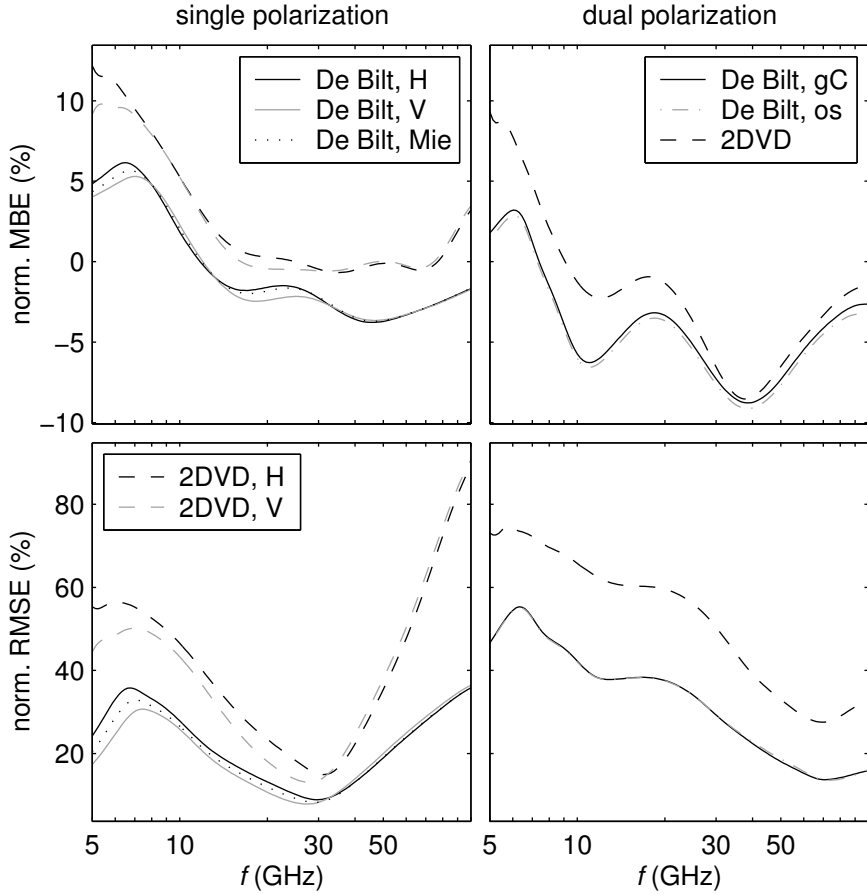
Figure 5.4: Normalized MBE and RMSE for point-scale retrieval of R from k_X (left) and Δk_{HV} (right) for single-frequency links. Note that all legends in the left (right) graphs apply to all graphs on the left (right). For dual-polarization measurements, results for oblate spheroidal (os) and generalized Chebyshev (gC) shaped drops are shown.

The analyses presented in this section are similar to those of Section 5.4.2, but apply to dual-frequency links. Figure 5.5 shows the reciprocal of the coefficients a_Δ^{-1} and exponents b_Δ of the power-law relations between R and $\Delta k_{XY}(f_1, f_2)$, and the normalized MBE and RMSE are shown in Figure 5.6. Only the values resulting from using DSDs measured in De Bilt (see Section 5.3.1) have been shown here, as they differ little with respect to those resulting from the 2DVD data (analyses not shown here).

Values of a_Δ and b_Δ have only been computed if the differential attenuation has the same sign for all DSDs. The white areas in the graphs indicate where
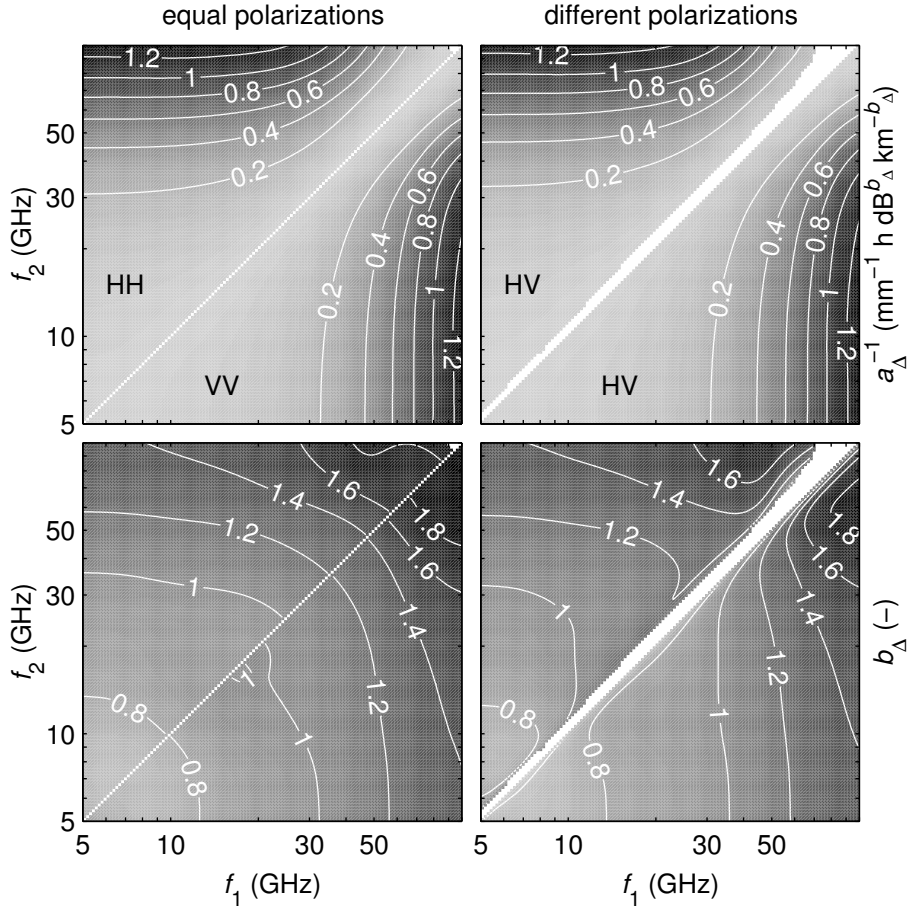
Figure 5.5: Results of fitting $R - \Delta k_{\mathrm{XY}}(f_1, f_2)$ power-law relations. Polarization combinations XY are indicated in the top panels, and apply to both the upper and the lower graphs. White areas indicate inconsistent signs of the differential attenuations for at least one DSD.

this is not the case. If for at least one of the DSDs the sign of the differential attenuation is different from that for other DSDs, the information contained in this differential attenuation is judged to be inappropriate for estimating the rainfall intensity using $R - \Delta k$ power laws. The parts of the graphs in Figures 5.5 and 5.6 to the left and above the white areas have been generated by using $-\Delta k_{\mathrm{XY}}(f_1, f_2)$, so that all differential attenuations are positive. Hence, the right panels of Figures 5.5 and 5.6 are the result of using $\Delta k_{\mathrm{HV}}(f_1, f_2)$ (bottom right) and $\Delta k_{\mathrm{VH}}(f_2, f_1)$ (top left).

The sensitivities (a_Δ^{-1}) are approximately equal regardless of the combination of polarizations (equal or orthogonal) used. The value of a_Δ^{-1} increases as
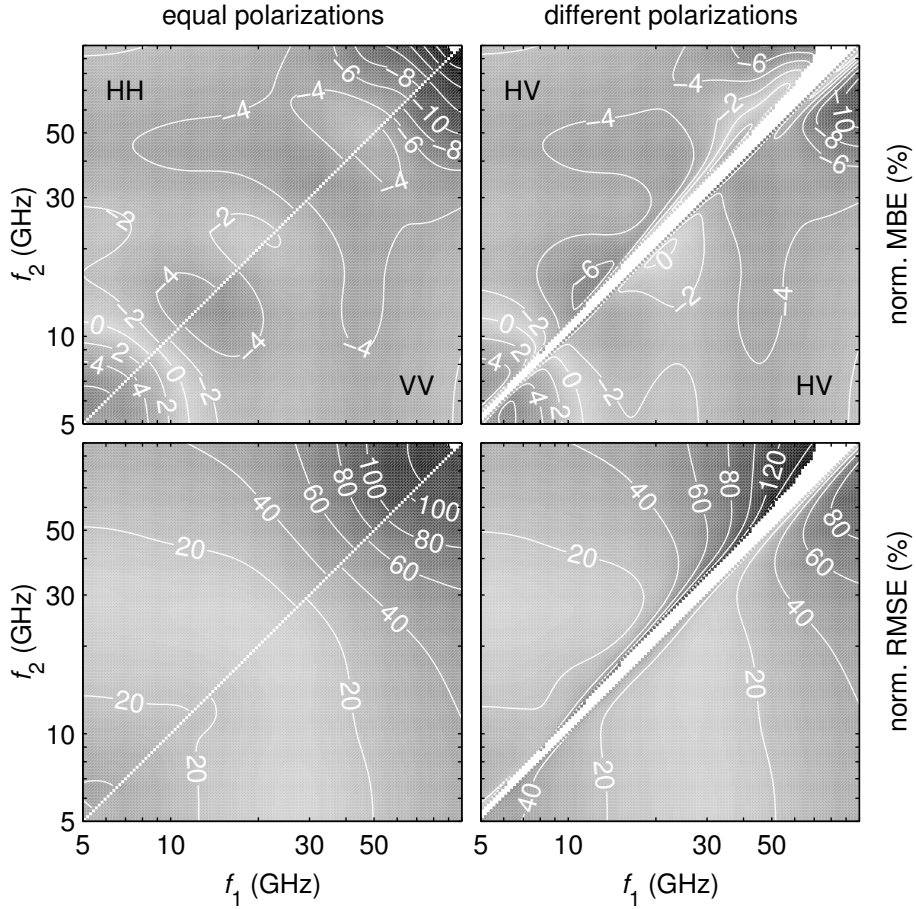
Figure 5.6: Normalized MBE and RMSE for point-scale retrieval of R from $\Delta k_{\mathrm{XY}}(f_1, f_2)$ for dual-frequency links. Polarization combinations XY are indicated in the top panels, and apply to both the upper and the lower graphs. White areas indicate inconsistent signs of the differential attenuations for at least one DSD.

the difference in frequency increases, which is to be expected. The low values of the sensitivities at low frequencies are caused by the insensitivity of k to R at low frequencies (see the top-left panel of Figure 5.3). The exponents of the derived power laws (b_Δ) are also nearly independent of the combination of polarizations used, except in regions where the two frequencies are similar. At these combinations of frequencies, the effect of the difference in frequencies is small relative to the effect of the polarization of the signal, whereas this latter effect is negligible at larger separations of the two frequencies.

It can be seen from Figure 5.6 that biases in the point-scale retrieved rainfall intensity are of the same order of magnitude as for single-frequency links, and

are smallest in regions where $b_\Delta \approx 1$. These regions also coincide with the smallest values of RMSE. Both the MBE and RMSE are seen to become quite large in regions where both frequencies are very low or very high. These regions also have the largest deviations of b_Δ from 1. Based on Figures 5.5 and 5.6 (i.e. results from point-scale measurements), it can be concluded that under Dutch climatic conditions, the optimal dual-frequency microwave link operates at approximately 30 GHz $< f_1 <$ 40 GHz and 15 GHz $< f_2 <$ 20 GHz (arbitrary combination of polarizations).

As the optimal single-frequency link appears to be the horizontally polarized 35.9-GHz link (see Table 5.1 and Section 5.4.2), part of the analyses concerning dual-frequency links in the remainder of this chapter will focus on those links with one signal fixed at these settings. The reason for this is that if one were to be able to choose link frequencies, it would be beneficial to choose one such that it could be used as a single-frequency link. There is no clear optimum for the other frequency, regardless of the polarization. The only criterium that can be given is that it should neither be too close to nor too far from the first frequency. If they are too close, the sensitivity becomes very low, and if they are too far apart, the additional information from the lowest frequency is negligible as the specific attenuation experienced by the signal of the highest frequency is much larger than that experienced by the low-frequency signal. Other dual-frequency link analyses will focus on frequency and polarization combinations found in the literature (see Tables 5.2 and 5.3 on p. 78 and p. 79, respectively): (b) *Rincon and Lang* (2002) (25.4 GHz and 38.0 GHz, both H), (c) *Holt et al.* (2003); *Rahimi et al.* (2003) (12.8 GHz and 17.6 GHz, both V), (d) *Rahimi et al.* (2003, 2004); *Upton et al.* (2005) (13.9 GHz and 22.9 GHz, both H), and (f) *Krämer et al.* (2005) (10.5 GHz and 17.5 GHz, both V). In the remainder of this chapter, these will be denoted by these parenthesized letters (see also Tables 5.2 and 5.3).

5.4.4   Temperature dependence

The results presented in the previous two sections depend on the temperature, as the complex refractive index of water (*Liebe et al.*, 1991) and the terminal fall velocities of raindrops (*Beard*, 1976) are functions of the rain temperature. *Delrieu et al.* (1991) have shown that temperature may play a significant role in attenuation at typical ground-based radar frequencies. So far, a temperature of 288.15 K (i.e., 15 °C) has been assumed. Figures 5.7 and 5.8 show the error (MBE) and the variation from DSD to DSD (RMSE) of the estimated rainfall intensity as a function of the rain temperature and signal frequency resulting from the (erroneous) assumption of $T = 288.15$ K. Note that values at $T = 288.15$ K (15 °C) correspond to those in Figures 5.4 and 5.6, respectively.

For single-frequency links, Figure 5.7 shows that there is litte temperature dependence (both MBE and RMSE stay relatively constant with temperature) if the signal frequency is sufficiently high. For frequencies below 10 GHz, in particular the MBE is sensitive to temperature, as was noted earlier by *Delrieu*

Figure 5.7: Normalized MBE (top) and RMSE (bottom) of the retrieved rainfall intensity from single-frequency links resulting from using a (or a_Δ) and b (or b_Δ) derived for $T = 288.15$ K as a function of frequency and temperature. Results are shown for horizontal (left), vertical (center) and differential (right) polarizations.

et al. (1991). For dual-polarization measurements, there is some temperature dependence at higher frequencies (where the optimum is, see Table 5.1), especially at low temperatures. However, the effect is not severe.

The results of dual-frequency links are also somewhat temperature dependent, as is shown in Figure 5.8. For the dual-frequency links with one signal fixed at 35.9 GHz (left and center panels), this dependence is limited, but for the two low-frequency combinations from the literature ((c) and (f)), this can be a problem. Hence, from this perspective it is wise to choose the highest frequency of dual-frequency links above at least 20 GHz.

5.5 Errors and uncertainties related to variations in DSDs

In the previous section, only point-scale relations were considered. Here, the effects of variations in the microstructure of rain on the retrieved path-average rainfall intensity are investigated as a function of link length. These analyses complement those presented by *Berne and Uijlenhoet* (2007), who limited their analysis of link length-dependent power law $R - k$ relations to single-frequency
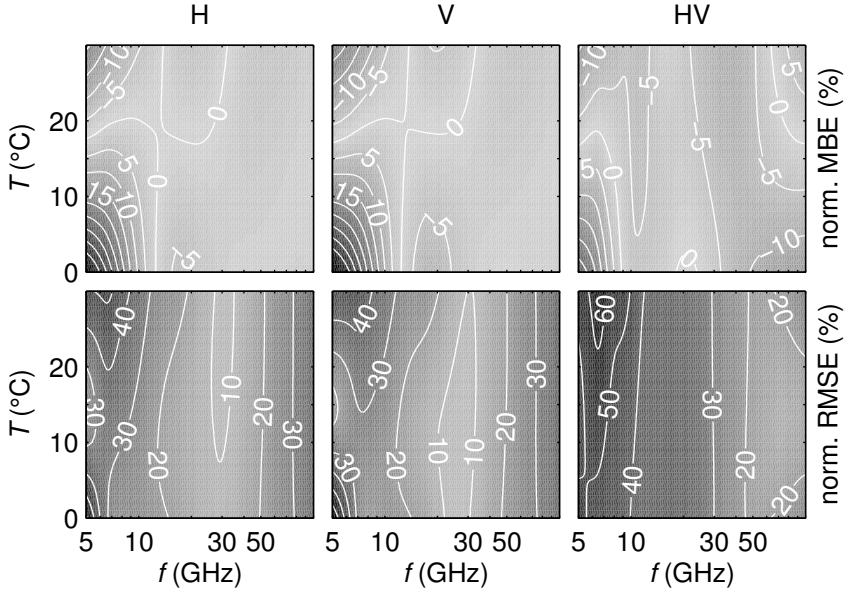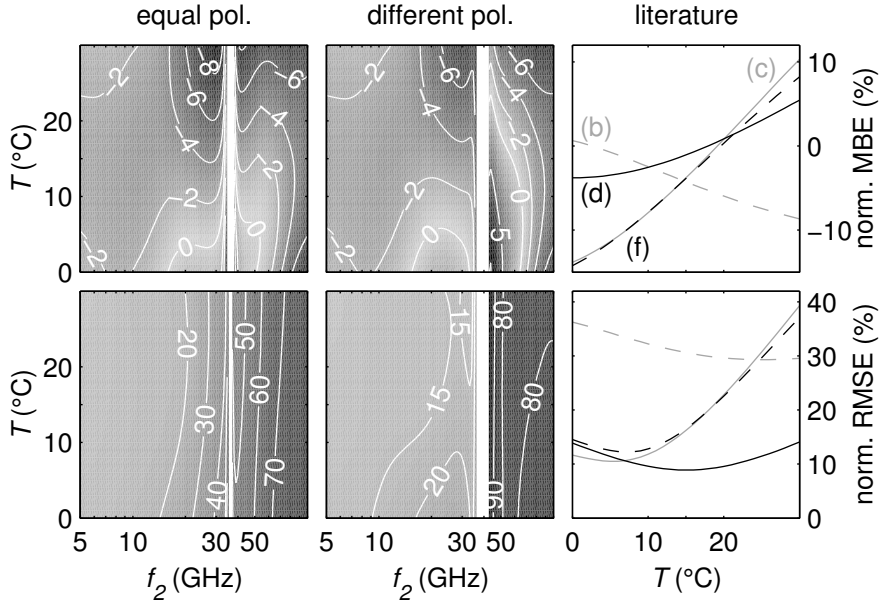
Figure 5.8: Normalized MBE (top) and RMSE (bottom) of the retrieved rainfall intensity from dual-frequency links resulting from using a_Δ and b_Δ derived for $T = 288.15$ K. The first signal has a frequency of $f_1 = 35.9$ GHZ and is horizontally polarized, and the second signal has a variable frequency f_2 and is horizontally (left) or vertically (center) polarized. Also shown are results for dual-frequency links encountered in the literature (right, (b), (c), (d), and (f)).

links and simulated spatially correlated exponential DSD parameters.

Range profiles of DSDs have been generated using time series of measured DSDs in combination with wind velocity measurements. Taylor's hypothesis is invoked to transform the time coordinate to a spatial coordinate. Profiles of DSDs are generated with a resolution of 250 m, which in this case corresponds to time intervals between 16.3 seconds and 14 minutes (with an average of 52.5 s), depending on the wind velocity. The use of these point-scale (i.e. 100 cm^2) DSD measurements for the generation of volume data (the average effective cross-section of the beam is $\sim \frac{1}{2}\lambda L$) will introduce some sampling uncertainty. The Edgeworth expansion technique as used by *Uijlenhoet et al.* (2006) was applied to analyse the sampling uncertainty in R for a 100 cm^2 sampling area given a *Marshall and Palmer* (1948) DSD for a rainfall intensity of 1.44 mm h^{-1}, the mean rainfall intensity measured by the 2DVD (see Figure 5.1). For a 16.3 s sampling interval, the coefficient of variation is 14% and the 10% and 90% quantiles are 1.19 mm h^{-1} and 1.71 mm h^{-1}, respectively. For a sampling interval of 52.5 s, these values are 7.9%, 1.30 mm h^{-1}, and 1.59 mm h^{-1}. Hence, uncertainties related to DSD sampling uncertainties are limited. The value of
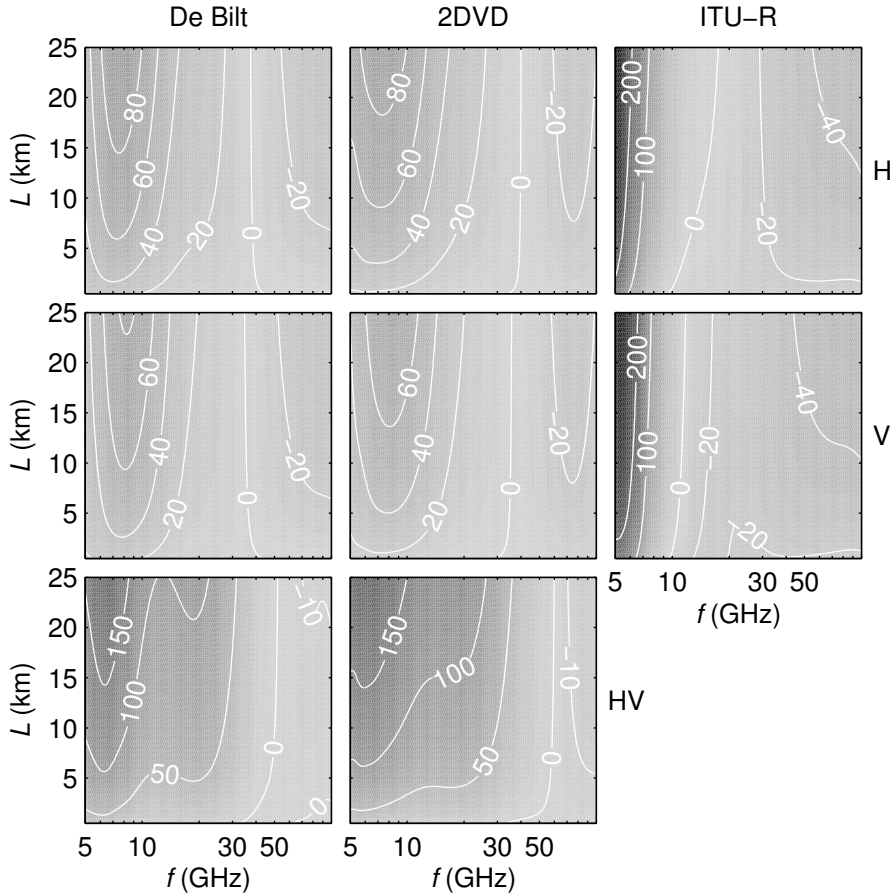
Figure 5.9: Normalized MBE (%) in the retrieved rainfall intensity resulting from using the point-scale relations derived from the De Bilt data (left, see section 5.3.1) and the 2DVD data (center, see section 5.3.2) and the *ITU-R P.838-3* (2005) relations (right) on the profiles generated using the 2DVD data. Results are shown for horizontal (top), vertical (middle) and differential (bottom) polarizations.

250 m for the present analyses was chosen based on a minimum sampling interval of 15 s.

Using the range profiles of DSDs, rainfall intensities R and values of specific attenuation k are computed for different frequencies and polarizations for each 250-m range bin. These values are then integrated over a given link length L, and divided by the same L to obtain virtual link measurements of k. Power-law $R - k$ and $R - \Delta k$ relations are then used to derive rainfall intensities from these virtual link measurements. These virtual link estimates of R can
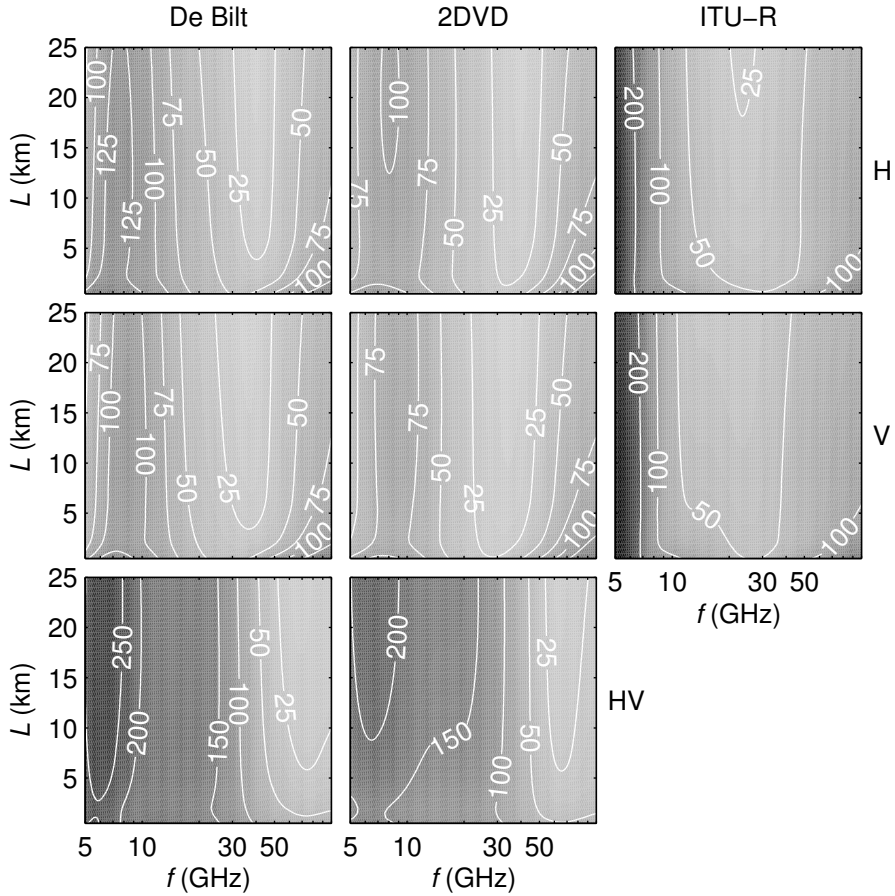
Figure 5.10: As Figure 5.9, but for normalized RMSE (%).

then be compared to true path-averaged R. Normalized MBE (Eq. (5.9)) and RMSE (Eq. (5.10)) will again be used to assess errors and uncertainties in link-estimated R.

5.5.1 Single-frequency links

Figures 5.9 and 5.10 show the normalized MBE and RMSE as functions of the link frequency and length. Results are shown for horizontal (top), vertical (middle) and differential (bottom) attenuation. For comparison of the different $R-k$ relations, all of the relations that were shown in Figure 5.3 have been used. Of these relations, the one derived using the 2DVD data can be seen to yield the best results, which is to be expected as it was derived using the same data as those used for the present analyses. The relations derived using the De Bilt

data are derived for Dutch climatological conditions, and are hence expected to perform relatively well (Figure 5.3 shows that the difference between these relations and those for the 2DVD data differ little). It can indeed be seen that the results using these relations are not much worse than those for the 2DVD relations, and that for the dual-polarization case it even performs better in terms of bias. The *ITU-R P.838-3* (2005) relations can be seen to give larger errors and uncertainties than the ones derived for Dutch conditions, especially at low frequencies.

At the optimum frequencies (see Table 5.1), the errors and uncertainties depend little on the length of the link. This is because the $R - k$ and $R - \Delta k$ relations do not depend on the DSD much at these frequencies, so that variations in DSDs along the link will not greatly influence results. However, at other frequencies (especially at the low end), variations in DSDs play a larger role, and hence the errors increase with link length. The averaging of DSDs resulting from using longer links can be seen to reduce the normalized RMSE somewhat. If the link frequency is chosen carefully (i.e., close to the optimal values given in Table 5.1), the MBE and RMSE are acceptable for all of the polarization settings.

5.5.2 Dual-frequency links

Errors and uncertainties for dual-frequency links are shown in Figure 5.11. Again (as in Section 5.4.4), one signal has been fixed at the optimal single-frequency settings (35.9 GHz, horizontally polarized), while the other is varied, and links settings from the literature have been used (see the end of Section 5.4.3). It is evident from these graphs that the errors and uncertainties are acceptable only if the second signal has a frequency that is lower than $f_1 = 35.9$ GHz in this case. Otherwise either the bias or the uncertainty will be very large. In the range where $f_2 < f_1$, it is apparent that using different polarizations yields smaller errors and uncertainties than using equal polarizations. The uncertainty (RMSE) decreases with link length due to decreased effect of variation in DSDs.

The two links with the low-frequency combinations from the literature ((c) and (f)) seem to be much less dependent on the length of the link, and the associated errors and uncertainties are much smaller than their high-frequency counterparts. However, as the temperature dependence of these low-frequency links is more severe (see Figure 5.8), it depends on the expected temperature variations which should be preferred.

Table 5.2 shows the coefficients and exponents of the $R - k$ and $R - \Delta k$ relations derived for the De Bilt data, as well as the errors and uncertainties that result from applying these relations to the (2DVD-derived) range profiles of DSDs for several (single- and dual-frequency) link settings (frequency, polarization and length), as presented in the literature. Both single- and dual-frequency links can be seen to perform well if the frequency (combination) is chosen correctly (for Dutch conditions). The errors and uncertainties are closely related to the proximity to unity of the exponent b or b_Δ of the $R - k$
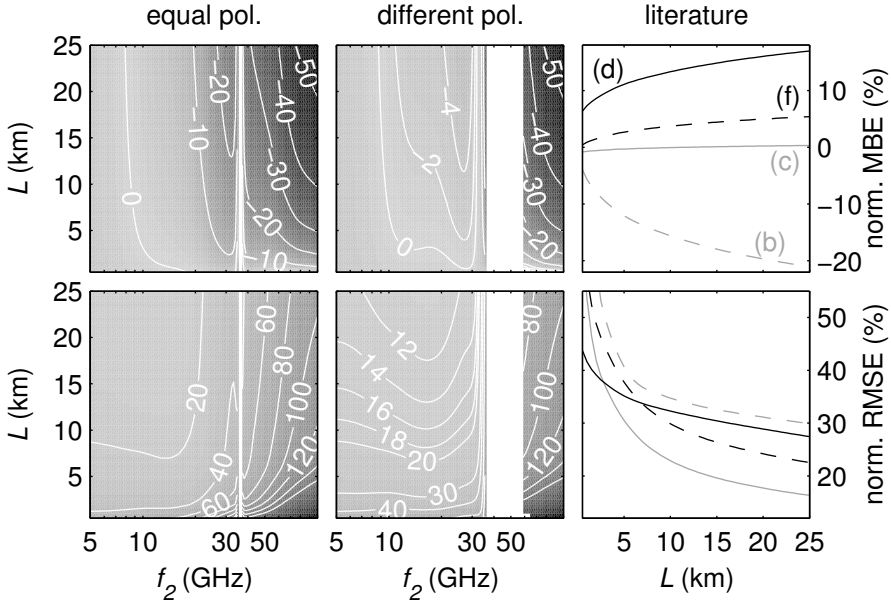
Figure 5.11: Normalized MBE (top) and RMSE (bottom) in the retrieved rainfall intensity resulting from using the point-scale relations derived from the De Bilt data for dual-frequency links with one of the signals fixed at $f_1 = 35.9$ GHz (horizontally polarized). The frequency of the second signal f_2 is varied, as is its polarization: horizontal (left) and vertical (center). Also shown are the results for frequency and polarization combinations from the literature (right, (b), (c), (d), and (f)).

or $R - \Delta k$ power laws. This is also apparent from Figure 5.12, where the normalized MBE and RMSE are shown as a function of the power-law exponent regardless of other link settings. This exponent can be seen to explain a large part of the variation in errors and uncertainties.

5.6 Effects of different rainfall climatology

To investigate the effect of contrasting climatological conditions, drop size distributions that are characteristic for intense Mediterranean rainfall have been simulated as described in Section 5.3.3. These DSDs have been used to derive coefficients and exponents of point-scale power-law relations (see Eqs (5.5) and (5.6)) between rainfall intensity and specific or differential attenuation as a function of link frequency (combination) and polarization. These coefficients and exponents have been fitted as described in Section 5.4. Using these power laws in combination with simulated DSD profiles, which are correlated in space, errors and uncertainties in retrieved path-averaged R can be quantified

as a function of link length and frequency (combination) for different polarization settings. The method to quantify these errors and uncertainties has been described in Section 5.5.

5.6.1 Single-frequency links

Results of the power-law fits for single-frequency links are shown in Figure 5.13, along with those for the De Bilt data and values suggested by *ITU-R P.838-3* (2005) (see Figure 5.3) for comparison. It can be seen that the exponent of the fitted power-law relations is closer to 1 than that of the other relations for nearly the entire range of frequencies under consideration, for both specific and differential attenuation. The optimal link frequency based on the linearity of the $R - k$ power-law for single-frequency links is 28.4 GHz for horizontal polarization, 24.2 GHz for vertical polarization, and 42.2 Ghz for differential attenuation. *Berne and Uijlenhoet* (2007) found that linearity of the relation between *path-averaged* R and k occurs at approximately 30 GHz for links longer than 3 km and at slightly lower frequencies for shorter links. These optimal frequencies are all considerably lower than those found using the De Bilt data (see Table 5.1). The coefficients of the Marseille power laws are comparable to those of the other power laws. As the relation between R and the measured variable is closer to linearity (see Figure 5.12), it is expected that the errors and

Table 5.2: Normalized MBE and RMSE of different link settings presented in the literature (see Table 5.3 for references (a) through (m)), computed using 2DVD-generated profiles with relations based on the De Bilt data. If two polarizations or frequencies are given, differential attenuation is used.

source letter	pol.	f (GHz)	L (km)	a, a_Δ	b, b_Δ	MBE (%)	RMSE (%)
(a)	HV	35.0	0.51	25.6	0.81	1.1	126.6
(b)	HH	25.4, 38.0	2.3	6.6	1.15	-8.8	55.2
(c)	VV	12.8, 17.6	23.3	31.6	0.99	0.3	17.3
(d)	HH	13.9, 22.9	13.9	12.5	0.93	14.6	32.3
(e)	N/A	50.0	0.82	2.0	1.13	-2.1	66.4
(f)	VV	10.5, 17.5	29.6	22.5	0.97	5.7	22.3
(g)	H	22.9	13.9	8.4	0.89	23.5	50.1
(h)	N/A	8.0	16.11	50.9	0.70	82.2	138.2
(i)	N/A	18.0	5.8^2	12.6	0.86	21.5	66.1
(j)	N/A	18.0	9.48	12.6	0.86	25.0	64.6
(k)	N/A	23.0	1.53	8.3	0.89	11.7	59.3
(l)	N/A	38.5	6.72	3.3	1.03	-0.1	20.6
(m)	N/A	27.0	4.89	6.3	0.92	13.6	45.0

[2]There are three links with near-equal lengths (5.77, 5.86, and 5.88 km) in the same frequency band
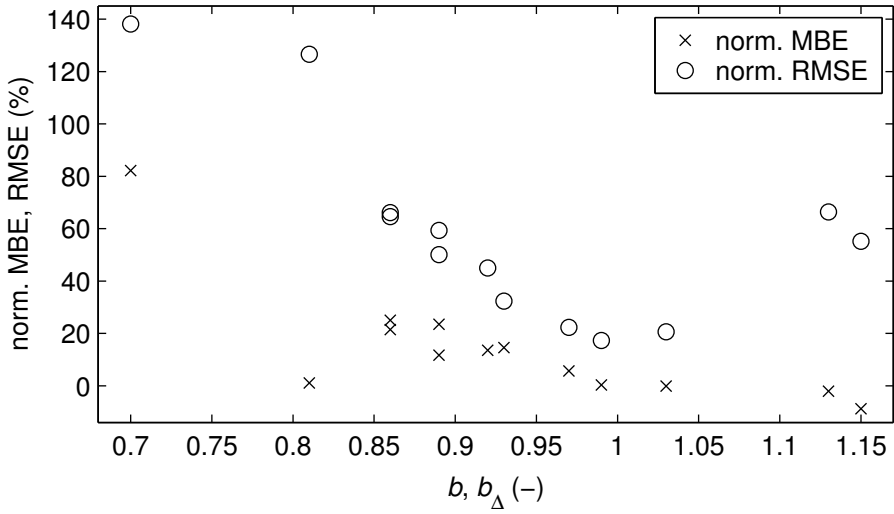
Figure 5.12: Normalized MBE and RMSE as a function of the exponent of the power law b or b_Δ for the link settings presented in the literature and given in Table 5.2.

uncertainties in microwave link rainfall estimates will be less severe for intense Mediterranean rainfall than for typical Dutch rain. The frequencies at which errors and uncertainties are minimal are expected to be lower than in Dutch conditions.

Figures 5.14 and 5.15 show the normalized MBE and RMSE, respectively,

Table 5.3: References to publications where microwave links have been used.

source letter	source
(a)	*Ruf et al.* (1996)
(b)	*Rincon and Lang* (2002)
(c)	*Holt et al.* (2003); *Rahimi et al.* (2003)
(d)	*Rahimi et al.* (2003, 2004); *Upton et al.* (2005)
(e)	*Minda and Nakamura* (2005)
(f)	*Krämer et al.* (2005)
(g)	*Upton et al.* (2005)
(h)	*Messer et al.* (2006)
(i)	*Messer et al.* (2006)
(j)	*Messer et al.* (2006)
(k)	*Messer et al.* (2006)
(l)	Chapter 4
(m)	Chapter 3
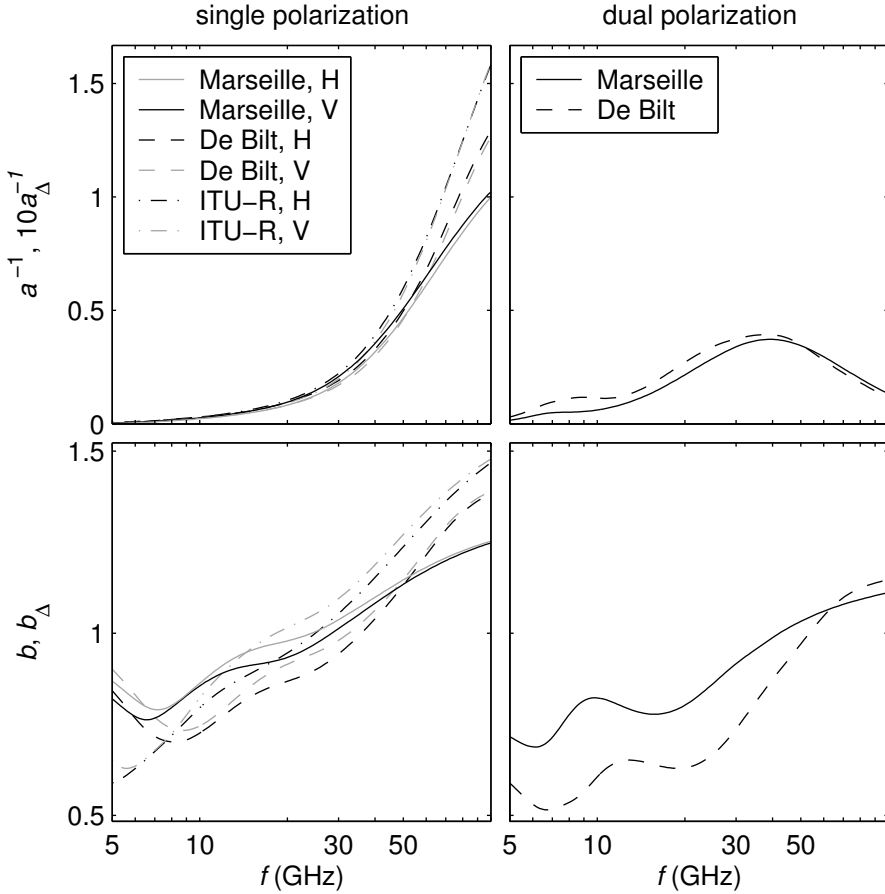
Figure 5.13: Results of fitting $R - k_X$ (left) and $R - \Delta k_{HV}$ (right) power-law relations for single-frequency links, for the Marseille DSD simulations. As a comparison, coefficients and exponents derived from the De Bilt data and those recommended by *ITU-R P.838-3* (2005) (single polarization only) are also shown (see also Figure 5.3). Note that the legends of the top graphs also apply to those below.

in the retrieved path-averaged R computed using the Marseille DSD simulations with three different types of $R - k$ relations. A comparison of Figures 5.14 and 5.15 (derived using the Marseille DSD simulations) to Figures 5.9 and 5.10 (derived using the Dutch 2DVD measurements) yields striking differences in the magnitudes of normalized MBE and RMSE. These large differences can be explained by the fact that the 2DVD-derived profiles suffer from sampling uncertainties, and that the Marseille DSD simulations are all based on exponential DSDs. Hence the use of a power law to describe the $R - k$ relation
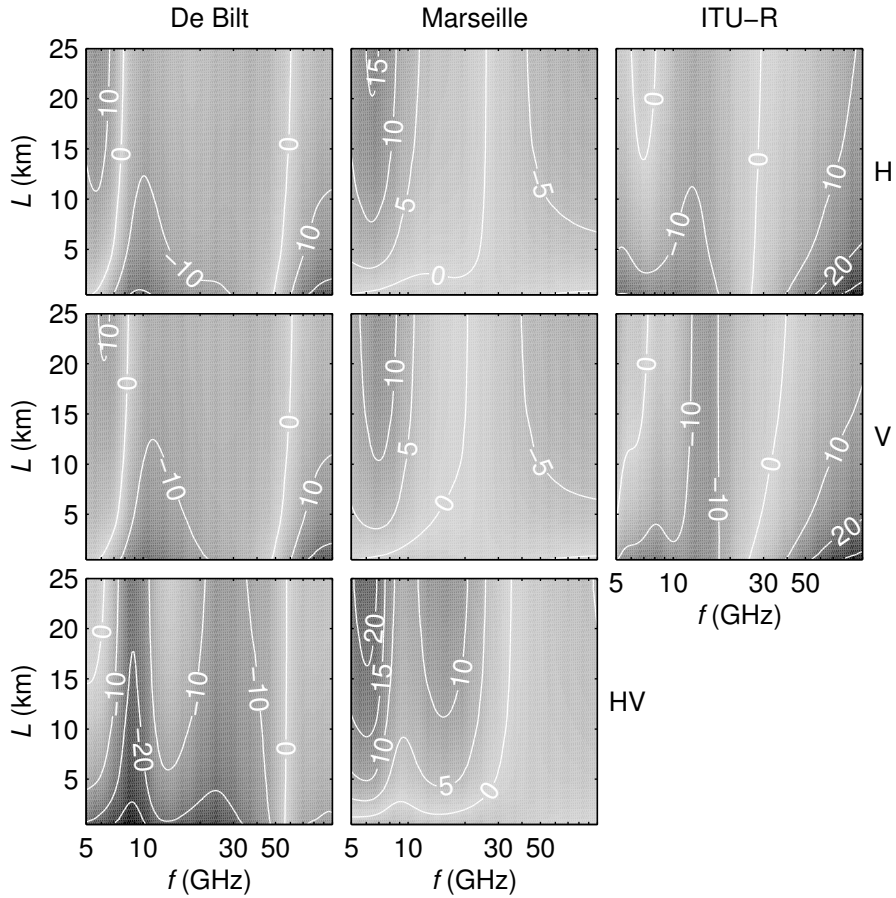
Figure 5.14: Normalized MBE (%) in the retrieved rainfall intensity resulting from applying the point-scale relations derived from the De Bilt data (left, see section 5.3.1) and the Marseille DSD simulations (center, see section 5.3.3), and the *ITU-R P.838-3* (2005) relations (right) to the simulated Marseille DSD profiles. Results are shown for horizontal (top), vertical (middle) and differential (bottom) polarizations.

results in lower error in the retrieved rain rate for Marseille DSDs than for 2DVD DSDs. Therefore, these large differences will not be further discussed here.

It is clear from Figures 5.14 and 5.15 that the point-scale power laws derived using the Marseille DSD simulations perform better than the others for shorter links. However, as links become longer, the performance of the other relations approaches that of the Marseille relations. This is due to the very short characteristic spatial scales of these intense Mediterranean rainfall events (e.g. *Berne*
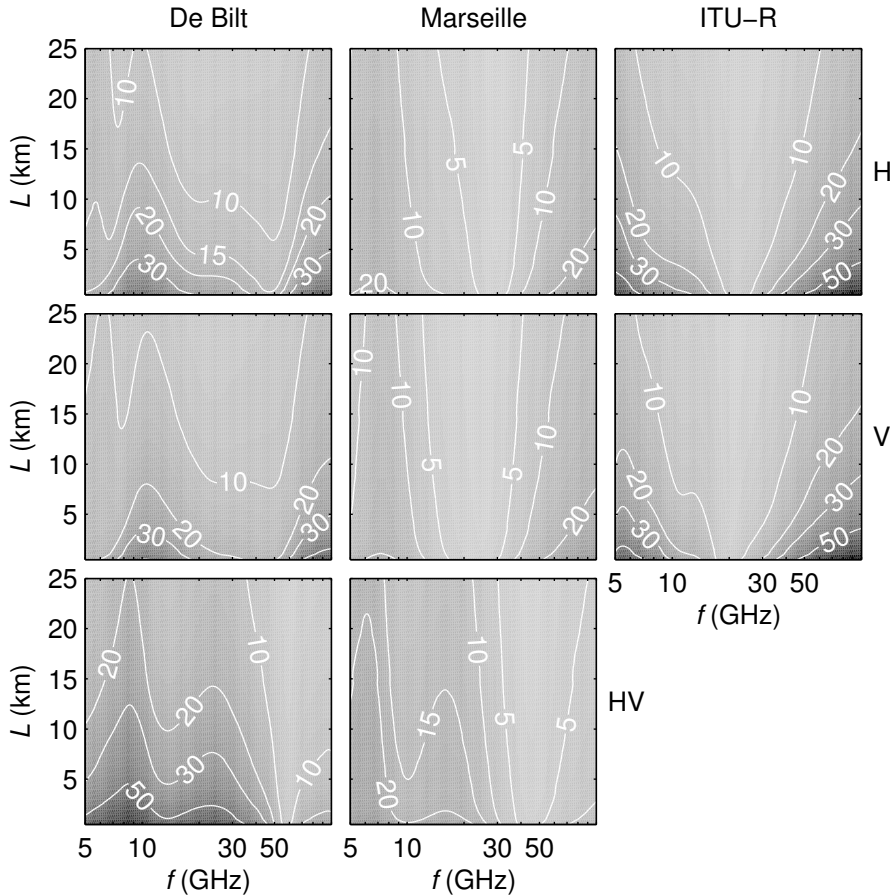
Figure 5.15: As Figure 5.14, but for normalized RMSE (%).

et al., 2004b). The averaging over long paths dampens out the extreme intensities that can occur at small scales. The relations that were derived using the Marseille DSD simulations accomodate for these extreme intensities, whereas the others don't. There is a frequency range where the MBE and RMSE are both limited for all link lengths. For single-polarization links, this frequency is around 30 GHz, and around 50 GHz for dual-polarization links. Hence, if the link frequency is chosen correctly, the use of point-scale $R-k$ relations derived for the climatology under consideration does not cause major errors.

5.6.2 Dual-frequency links

Figure 5.16 shows the power-law coefficients and exponents for dual frequency links as functions of the two frequencies, for different polarization combinations.
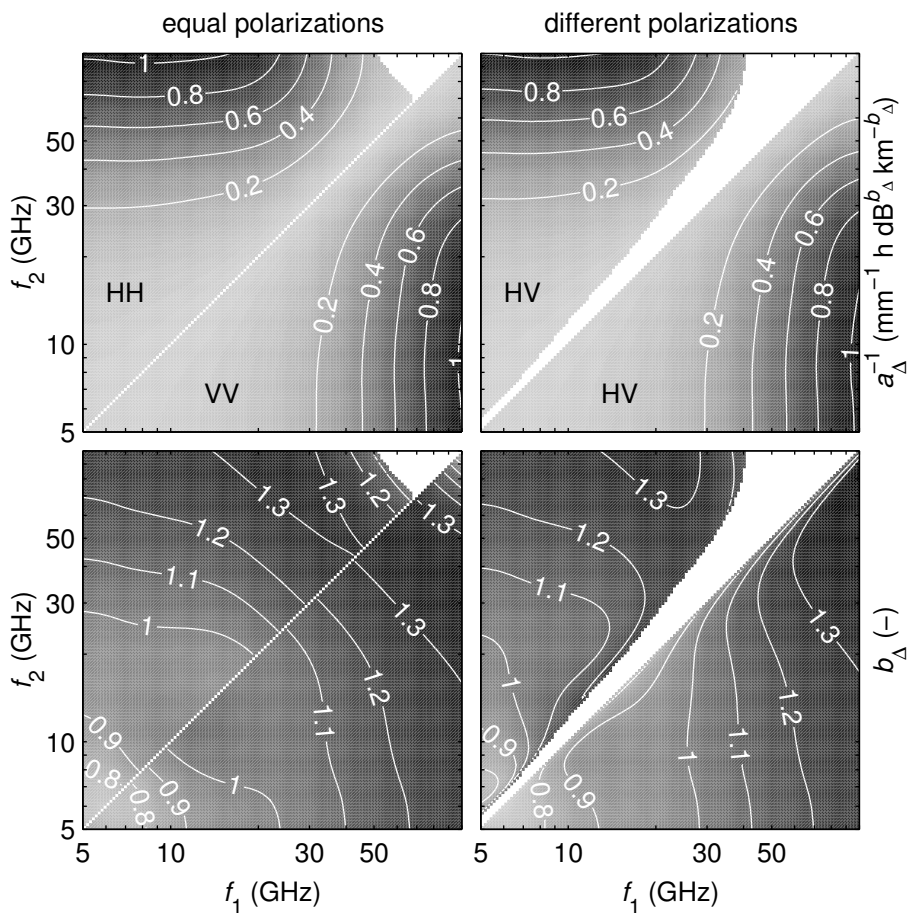
Figure 5.16: Results of fitting $R - \Delta k_{\mathrm{XY}}(f_1, f_2)$ power-law relations for the Marseille DSD simulations. Polarization combinations XY are indicated in the top panels, and apply to both the upper and the lower graphs. White areas indicate inconsistent signs of the differential attenuations for different DSDs.

Compared to the $R - \Delta k$ relations derived for the De Bilt data (see Figure 5.5), there is little difference for low frequencies. However, when one (or both) of the two frequencies is high, the value of the exponent of the relation derived for the Marseille DSD simulations is closer to 1. This is similar to what was observed for the $R - k$ relations for single-frequency links (see Figure 5.13). The values of the power-law coefficients also differ little at high frequencies. However, as was noted in Section 5.6.1, apparent small differences in $R - k$ power laws do not necessarily imply that the differences in corresponding errors and uncertainties are small.
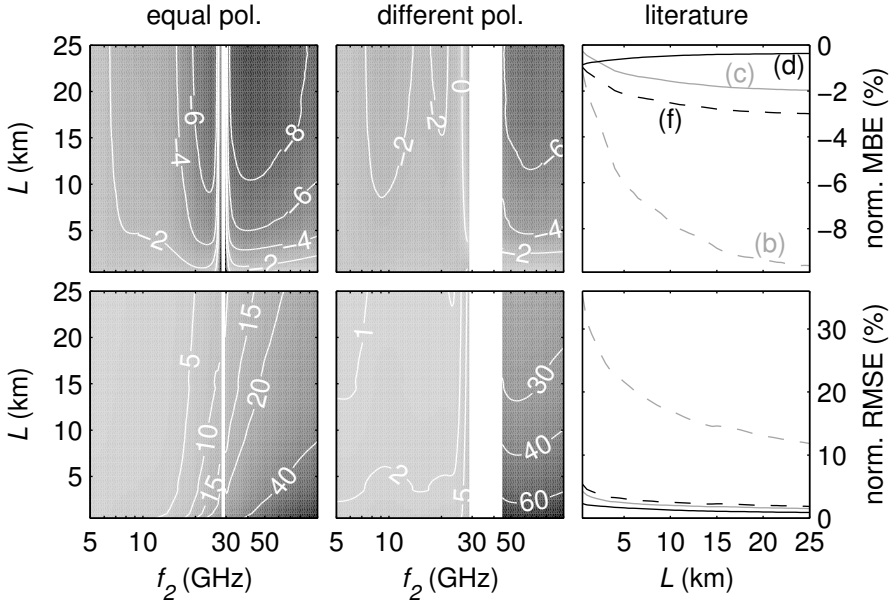
Figure 5.17: Normalized MBE (top) and RMSE (bottom) in the retrieved rainfall intensity resulting from using the point-scale relations derived from the Marseille DSD simulations for dual-frequency links with one of the signals fixed at $f_1 = 28.4$ GHz (horizontally polarized). The frequency of the second signal f_2 is varied, as is its polarization: horizontal (left) and vertical (center). Also shown are the results for frequency and polarization combinations from the literature (right, (b), (c), (d), and (f), see Section 5.4.3).

Normalized MBE and RMSE are shown in Figure 5.17 for dual-frequency links when one of the signals is fixed at a frequency of $f_1 = 28.4$ GHz and horizontally polarized (the optimum for a single-frequency link, see Section 5.6.1), and for four frequency combinations from the literature (see Section 5.4.3). For these analyses, $R - \Delta k$ relations derived from the Marseille DSD simulations have been used (see Figure 5.16). It is clear from these figures that if the second frequency is chosen below 28.4 GHz, dual-frequency links yield good results. The same conclusions could be drawn from Figure 5.11 for Dutch conditions, where measured (2DVD) DSD profiles were used with $R - \Delta k$ relations derived using the De Bilt data. The structure of these graphs is similar to those in Figure 5.17, leading to similar conclusions. Of the frequency combinations suggested in the literature, all except (b) are seen to perform well. The fact that (b) performs worse than the other three is likely due to the larger deviation from unity of the exponent of the $R - \Delta k$ power law at this frequency combination (25.4 GHz and 38.0 GHz, both V).

5.7 Conclusions

The objective of this chapter was to assess the errors and uncertainties in single- and dual-frequency microwave link estimates of path-averaged rainfall intensities. Measurements from two types of disdrometers have been used in combination with a numerical electromagnetic scattering model to compute rainfall intensities and specific attenuations at different frequencies and polarizations. The effect of canting angles of drops on the specific attenuation and the differential attenuation (for different polarizations) has been investigated and has been found to be of minor influence, and even negligible for specific attenuation.

Power-law relations between rainfall intensity and quantities that can be measured using single- and dual-frequency microwave links (either k or Δk) at the point scale have been derived and evaluated. Criteria for determining the optimum frequency (or combination of frequencies) are given: (1) the exponent of the power law should be close to 1; (2) the sensitivity should be large; and (3) the expected errors and uncertainties should be small. For all of the methods presented (single- and dual-frequency/polarization), there is a frequency (combination) between 5 and 100 GHz at which the exponent of the power law is 1. The associated sensitivities at these frequencies are relatively large (compared to the values at other frequencies). The corresponding errors and uncertainties are usually at a minimum around these frequencies, from which we can conclude that at the optimum frequencies (i.e., exponent close to 1), the dependence of the relation between R and k or Δk on the DSD is also at a minimum. For dual-frequency links, there are two degrees of freedom that can be tuned to meet all of the above criteria. Hence, for all of the methods examined, an optimal frequency (combination) can be found. For dual-frequency links, it is suggested to choose one of the frequencies such that it is optimal for single-frequency use.

For single-frequency links, the sensitivity is much larger for k than that for Δk. This would mean that specific attenuation should be preferred over differential attenuation. However, the insensitivity of differential attenuation to problems such as absorption by atmospheric constituents and wet antenna attenuation give this method a clear practical advantage. A more detailed study of these issues is beyond the scope of this chapter.

As attenuation and rainfall intensity are both dependent on temperature, this dependence has been investigated at the point scale. Variation with temperature for single-frequency links is only important at frequencies far away from the optimum for specific attenuation. For differential attenuation, there is a limited temperature dependence. For dual-frequency links with one frequency fixed at the optimum for single-frequency links, temperature dependence is also limited. However, for some frequency combinations from the literature temperature may play a significant role.

Arrival times, drop sizes and velocities measured by a 2DVD during the BBC2 measurement campaign at CESAR (The Netherlands) have been used in combination with wind velocity measurements to generate range profiles of

DSDs. These profiles have been used to compute corresponding profiles of rainfall intensities and specific attenuations (at different frequencies and polarizations). Using these profiles, the effect of the variation in DSDs along a simulated microwave link has been studied as a function of its length, frequency (combination) and polarization (combination). For single-frequency single-polarization links, the effect of using different relations to convert specific attenuation to rainfall intensity has been studied. One type of relation was derived using the same dataset (the 2DVD data), one was derived using a different data set for the same climatology, and yet another one was taken from the literature.

The errors made in the retrieved path-averaged rainfall intensities are nearly always at a minimum at the optimal frequency derived using point-scale data. This is due to the relative insensitivity of the $R-k$ and $R-\Delta k$ relations to the DSD at these optimum frequencies. This is also the reason why there is hardly any dependence on the length of the link at these frequencies. At frequencies away from the optimum, errors (i.e. bias) increase with link length, which can be attributed to the nonlinearity of the $R-k$ and $R-\Delta k$ relations at these frequencies. Uncertainties are seen to slightly decrease with link length, as longer links average more. For dual-frequency links, errors may become severe if one of the frequencies is chosen to be very high (> 60 GHz). In the case where one of the signals is at the optimum for single-frequency links, errors and uncertainties are limited if the second frequency is chosen below the first. The dependence of the errors and uncertianties on link length varies with the chosen frequency pair.

The $R-k$ relations recommended by *ITU-R P.838-3* (2005) which are often used operationally are not well suited for Dutch conditions. The relations derived for Dutch conditions perform much better, even if they are derived using a different instrument than used to validate them. This means that it is preferable to use local relations for accurate microwave link rainfall estimation.

In order to investigate the effect of different climatologies on the errors and uncertainties related to microwave link rainfall estimation, analyses have been carried out using simulated DSD profiles based on intense Mediterranean rainfall. The derived $R-k$ and $R-\Delta k$ relations are closer to linearity than those derived using Dutch DSD datasets and those recommended by *ITU-R P.838-3* (2005) over nearly the entire range of frequencies under consideration. The errors and uncertainties in the retrieved path-averaged rainfall intensity are less severe when local $R-k$ relations (i.e., those derived using the Marseille DSD simulations) are used, especially for shorter links for the small-scale intense Mediterranean rainfall under consideration. Magnitudes of normalized MBE and RMSE computed using the 2DVD-measured DSD profiles and those computed using simulated Marseille DSD profiles have not been compared here because there are too many differences in the nature of the underlying data sets. For dual-frequency links, the range of frequency combinations where errors and uncertainties are small is smaller when derived using the Marseille DSD simulations than that when derived using 2DVD-measured DSDs. Otherwise the dependence of errors and uncertaities on link frequency and length (i.e., the

general behavior, not the magnitude) is seen to be similar when derived using these two data sets.

It is possible to choose microwave link frequency (pairs) and polarization (pairs) such that both systematic errors and uncertainties are limited. These links can be operated over a range of lengths without much loss of accuracy. However, errors related to e.g. absorption by atmospheric constituents and wet antenna attenuation will have to be studied to be able to provide a more complete picture of the type of link that is best suited for rainfall estimation in a given climatological setting.

CHAPTER 6

Effects of the macrostructure of rain

6.1   Introduction

Microwave links can be used to estimate path-averaged rainfall intensity, both in a research setting (e.g. *Ruf et al.*, 1996; *Rincon and Lang*, 2002; *Holt et al.*, 2003; *Minda and Nakamura*, 2005, and Chapter 3) and using commercial cellular communication networks (see *Messer et al.*, 2006, and Chapter 4). Some of the issues that have been raised in several of these publications include the effects of the spatial variation of rain (*Berne and Uijlenhoet*, 2007, and Chapters 3, 4, and 5), the temporal sampling (see Chapter 4), the resolution with which the received power is stored (Chapter 4) and wet antenna attenuation (*Minda and Nakamura*, 2005, and Chapters 3 and 4). These issues will be examined in this chapter using high-resolution X-band weather radar data collected in The Netherlands during more than 1.5 years, as well as data from the 27 GHz microwave link described in Chapter 3.

This study is different from that of *Berne and Uijlenhoet* (2007) and that presented in Chapter 5 in the sense that these studies focused solely on the variation of DSDs along the path of the link, and were only able to investigate the effect of spatial variation. Here, the nature of the data set used is such that the effects of both spatial and temporal variations can be examined, and climatological statistics for Dutch conditions can be derived. The issues related to rainfall estimation using commercial cellular communication links

---

(see Chapter 4) such as the effect of temporal sampling and power resolution can hence be studied. Link signals have been simulated using rainfall fields in the past (*Giuli et al.*, 1991, 1999), albeit for studying different aspects of microwave link rainfall estimation than examined in the present study. However, these studies were based on 2 hours of rainfall data generated using a stochastic model (*Giuli et al.*, 1991) and 30 minutes of radar data (*Giuli et al.*, 1999), whereas the results presented in this chapter are based on more than 1.5 years of radar data.

Wet antenna attenuation is a problem that has been identified in the literature, but still requires much attention before microwave links can be used for accurate estimation of rainfall intensities. There have been experiments where antennas have been wetted artificially (see *Kharadly and Ross*, 2001; *Minda and Nakamura*, 2005), but a general description of the phenomenon is still lacking. A simple parametric method is proposed to compute the attenuation caused by wet antennas, of which the parameters are independent of frequency. These parameters are calibrated based on data from an experiment with a 27-GHz microwave link (see Chapter 3). Subsequently, this method is applied to investigate the effects of wetting of antennas, and correction for this.

Time series of profiles of rainfall intensities derived from these radar data are used to generate time series of profiles of specific attenuation for different microwave frequencies. From these profiles virtual microwave-link estimates of rainfall intensity can be derived as a function of the link length, which can then be compared to the "true" path-averaged rainfall intensity. Degradation of the power resolution and wetting of the link antennas are also simulated in this framework. The interplay between the space-time structure of rain and the length of the link, the non-linearity of the $R - k$ relation and the temporal sampling strategy is the cause of the errors and uncertainties examined in this chapter. Therefore, this space-time structure of rain will also be analyzed. The results from these analyses can then be used to explain the observed behavior of the derived errors and uncertainties in link-estimated rainfall intensities as a function of link length and temporal sampling.

Actual microwave link and rain gauge measurements are used to perform similar analyses. The effects of the degradation of power resolution, of the applied temporal sampling strategy, and of the correction for wet antennas are examined. The results can then be compared to the results from the simulations.

The data sets used in this chapter are discussed in Section 6.2, in particular the radar data set and corrections applied to it. The method used to simulate microwave link signals is also presented in this section. Wet antenna attenuation is discussed in Section 6.3. In Section 6.4 the space-time structure of rain is investigated using the radar data. Results of simulation of microwave link signals are described in Section 6.5, where the effects of the link length and frequency, temporal sampling strategy, power resolution, wetting of antennas, and correction for this are shown as well. Results of actual link measurements are also given as a comparison. Finally, conclusions are drawn in Section 6.6.

6.2 Data and methodology

6.2.1 Radar data

Data were collected by the International Research Centre for Telecommunications-transmission and Radar (IRCTR) of the Department of Electrical Engineering, Delft University of Technology (TU Delft) between May 15, 1993 and December 31, 1994 using the high-resolution X-band FM-CW weather radar SOLIDAR (see *Ligthart and Nieuwkerk*, 1990, for more details regarding this radar). At the time of interest, SOLIDAR was located on top of the 97 m high Electrical Engineering building at the TU Delft, The Netherlands. Table 6.1 lists some characteristics of this radar.

A typical map of radar reflectivity factors (in dBZ) is shown in Figure 6.1, which shows that the radar only covers a 240° sector. This is due to another radar blocking the beam in the remaining 120°. Several areas affected by unwanted echoes from ground targets (clutter) are also apparent in this figure.

Because of storage capacity issues, radar data were only stored when judged to be interesting for atmospheric propagation studies. This judgment was performed automatically based on measurements by multiple instruments installed in the area. The following four criteria have been used for storing of radar data (see *Ligthart and Nieuwkerk*, 1990):

1. At least one of two radiometer readings indicate that there is at least 0.6 dB attenuation on a satellite path.

2. At least one of four rain gauges (in the area covered by the radar) measures a one-minute averaged rainfall intensity of 2 mm h^{-1}.

3. At least one of the radar pixels registers a reflectivity value corresponding to a rainfall intensity of at least 10 mm h^{-1}.

4. At least 5,500 out of the 16,384 (i.e., 33.6%) radar pixels register a reflectivity value corresponding to a rainfall intensity of at least 2 mm h^{-1}.

These criteria result in a data set containing separate rainy periods. Only those periods where at least 30 minutes of consecutive data have been recorded have been used for the present analyses. An additional manual selection based on visual inspection of the radar data for non-rain related artefacts (e.g., sudden

Table 6.1: Characteristics of the SOLIDAR radar

frequency	9.47 GHz
range resolution	0.12 km
azimuth resolution	1.875°
beam width	2.8°
maximum range	15.36 km
revolution time	15.6 s
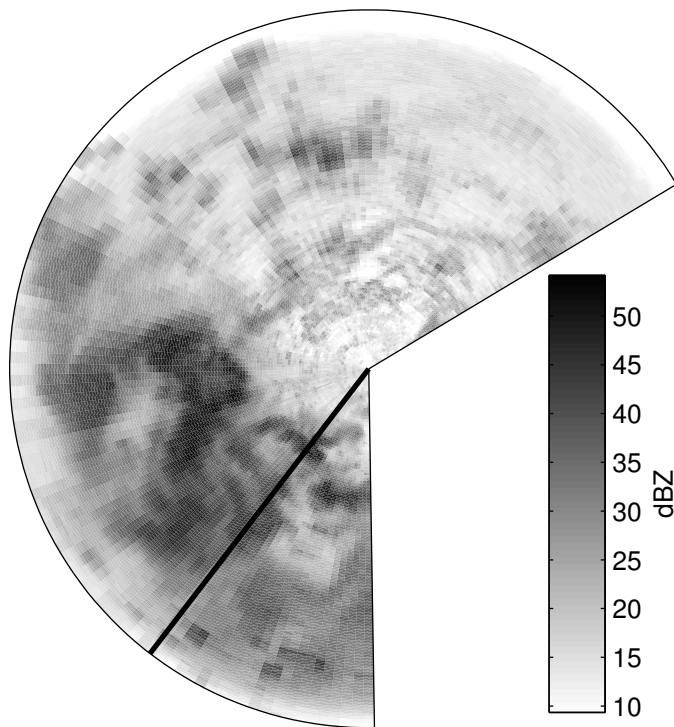
Figure 6.1: Map of radar reflectivity values (in dBZ) on 8 September 1993 at 16:33 local time. The thick black line indicates the selected radial.

beam-filling peaks in reflectivity) has been applied. The resulting data set consists of 332 events with a total length of 16 days (i.e., 384 hours) and 40 minutes, corresponding to a total of 89210 radar images.

For the purpose of this study, the main interest is in obtaining realistic range-time maps of rain. Hence it is more important to capture the spatial and temporal structure and the intermittency (i.e., identification of wet and dry periods and areas) of rain rather than having maps of precise values of rainfall intensities. The corrections applied to the radar reflectivity factors Z (mm^6 m^{-3}) in the data set described in Appendix A focus on this aspect.

Broadening of the radar beam with range may affect the derived rainfall fields because of the range-dependence of the sampling volume (it increases by a factor of 100 as the range increases from 1 to 10 km). However, as shown in Figure 6.2, there is no systematic behavior with range of the base level of Z. Hence, it is assumed that this causes no systematic errors. A more detailed study of this sampling effect is outside the scope of this chapter. Because only one radial has been selected in the radar data, derived statistics may be different if a different direction had been chosen. The direction of the selected radial is nearly parallel to the prevailing wind direction in this area. An investigation of the effect of choosing a direction that is e.g. perpendicular to the prevailing
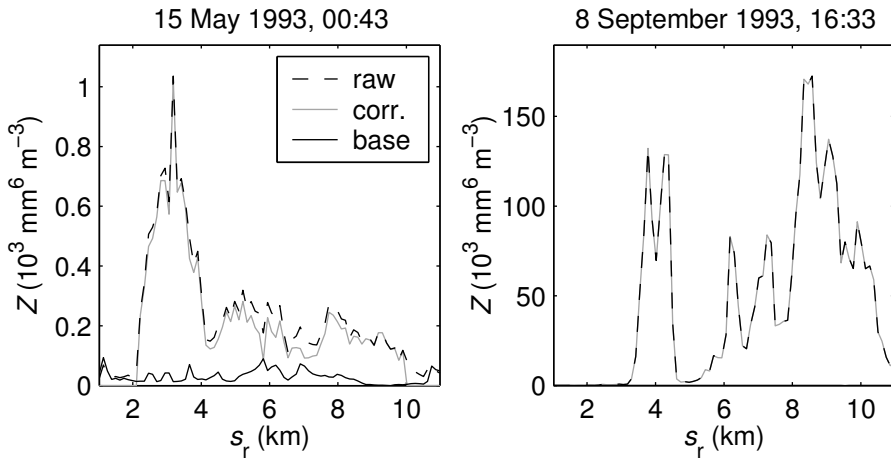
Figure 6.2: Examples of range profiles of Z before (raw) and after (corr) correction. Also shown is the range-dependent base level (see Appendix A) of Z used in the correction (base). Maximum values of Z correspond to $R = 2.8$ mm h^{-1} (left) and $R = 53.8$ mm h^{-1} (right).

wind direction is outside the scope of this study.

The range-time field of rainfall intensities resulting from the corrections described in Appendix A will be used in all subsequent analyses in this chapter. The fraction of zero-rainfall radar bins for all events is 49%. The histogram of nonzero rainfall intensities for all radar bins under consideration is shown in Figure 6.8 on p. 100.

6.2.2 Microwave link data

Microwave link data have been collected during an earlier experiment (see Chapter 3) in the late spring-early summer of 1999 with a 4.89-km 27-GHz research link and a line configuration of 7 tipping bucket rain gauges. The microwave link is sampled with a frequency of approximately 18 Hz. Three-minute averages of path-integrated attenuation measured by the link and of rainfall intensities measured by the gauges, resulting in 3335 time steps in 25 events, are used for the calibration of wet antenna attenuation relations. The two gauges closest to the antennas of the microwave link (0.00 km and 0.43 km) are used to measure rainfall at the antennas. The sum of the wet antenna attenuation at the two antennas is computed by subtracting the expected path-integrated attenuation based on the rain gauge measurements from the measured total attenuation. Hence, we assume that the gauge-measured path-averaged rainfall intensity is the true path-averaged R.

For the analyses of the errors related to sampling, 15-minute periods are used (see also Appendix A). There are 721 of such periods (corresponding to
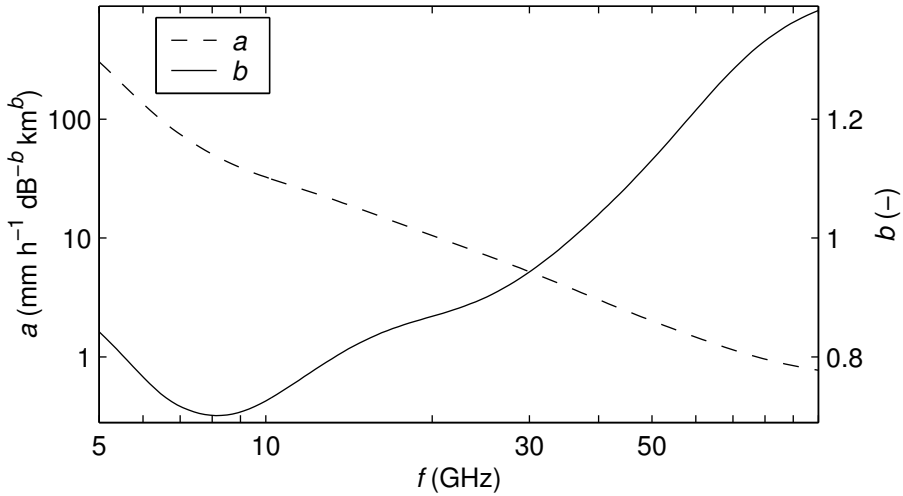
Figure 6.3: Coefficient a and exponent b of the power-law relation between R and k as a function of signal frequency (see also Figure 5.3).

more than 7.5 days), each containing 16,386 samples, in these 25 events in the data set.

6.2.3 Simulation of microwave link data

The profiles of rainfall intensities derived from the radar data (see Section 6.2.1) are used to generate microwave link signals for different link lengths between 0.24 and 10.08 km and at different frequencies between 5 and 100 GHz. The profiles of R are converted to profiles of specific attenuation using relations derived for horizontal polarization in Chapter 5. Figure 6.3 shows the frequency dependence of the coefficient a and exponent b of the power-law relation between R and k (see also *Atlas and Ulbrich*, 1977)

$$R = ak^b. \tag{6.1}$$

The coefficients and exponents of these power laws have been calculated based on drop size data measured by *Wessels* (1972) over more than one year in De Bilt, The Netherlands. Scattering was computed using the T-matrix method (see e.g. *Mishchenko*, 2000), where generalized Chebyshev-shaped drops (e.g. *Chuang and Beard*, 1990) were assumed. Path-integrated attenuation over a link is then computed by integrating the profiles of specific attenuation over the length of this link. The simulated links of different lengths all have the same center, and for each link length increment, one range cell is added on each side of the profile used for the computation of path-integrated attenuation.

Path-averaged rainfall intensities are retrieved from these simulated link signals using Eq. (6.1). These retrieved values of R are then compared to true

path-averaged rainfall intensities by calculating the mean bias error (MBE) and the bias-corrected root mean square error (RMSE)

$$\text{MBE} = \frac{1}{N_\text{s}} \sum_{i=1}^{N_\text{s}} \left(a k_i^b - R_i \right) \tag{6.2}$$

$$\text{RMSE} = \sqrt{\frac{1}{N_\text{s}} \sum_{i=1}^{N_\text{s}} \left(a k_i^b - R_i - \text{MBE} \right)^2}, \tag{6.3}$$

where N_s is the total number of time steps in the entire data set (i.e., the sums are taken over the entire data set and not over each event separately). Note that the RMSE according to this definition is equivalent to the standard deviation of the residuals. Both of these errors are normalized by the mean rainfall intensity $\frac{1}{N_\text{s}} \sum_{i=1}^{N_\text{s}} R_i$, as shown as a function of link length in Figure 6.9 on p. 101. Note that the link-estimated rainfall intensity is computed using the same power-law relation as was used to convert point-scale R to point-scale k. Hence, results of these simulations will only include effects related to the interplay between non-linearity of $R-k$ relations and the spatial variation in R. The effects of using erroneous $R-k$ relations have been investigated elsewhere (see e.g. *Berne and Uijlenhoet*, 2007, and Chapter 5).

6.3 Wet antenna attenuation

It has been shown by *Minda and Nakamura* (2005) and in Chapters 3 and 4 that wetting of antennas in rain causes additional attenuation that can lead to severe overestimation of the rainfall intensity. Here, an attempt is made to quantify the errors caused by this phenomenon, and it is investigated how well a correction algorithm would work in different settings. For this purpose, it is assumed that in rain, a water film of uniform thickness l is formed on the material (e.g. a water-repellent cloth) covering the antennas, and that l depends only on the rainfall intensity. This implies that the water film instantaneously disappears when it stops raining, which was shown in Chapter 3 to be a valid assumption. The relation used to compute the wet antenna attenuation from l is given in Appendix B. Empirical relations for wet-antenna attenuation such as those given by *Kharadly and Ross* (2001) cannot be used in this study as the corresponding parameters depend on the frequency of the link. Therefore wet antenna attenuation cannot be studied as a function of link frequency using these relations.

6.3.1 Calibration of wet antenna attenuation function

The relation between the rainfall intensity and the thickness of the water layer formed on link antennas is of course dependent on the type of antenna (e.g., shape, cover material), the wind direction, surrounding obstacles, etc. It is
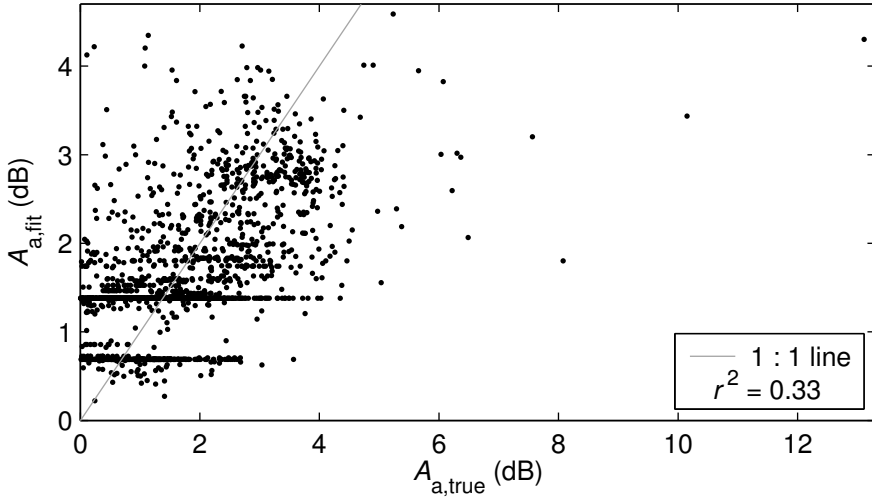
Figure 6.4: Fitted wet antenna attenuation vs. that derived from measurements.

assumed here that all links use similar antennas, and that the thickness of the water film depends only on R. The microwave link and raingauge data from the experiment described in Chapter 3 and Section 6.2.2 are used to fit a relation between the water layer thickness l and R, which is asusmed to be a power law

$$l = \gamma R^{\delta}. \tag{6.4}$$

The values of γ and δ are determined by numerical non-linear least-squares fitting of the measured sum of the attenuation caused by the two antennas (see Section 6.2.2) to that computed from Eqs (6.4) and (B.1) (see Appendix B) using the rain gauge-esimated values of R at the two antennas (i.e., the values of wet antenna attenuation are computed for each antenna separately, after which they are added). The values of γ and δ are varied in order to find optimum values for which the sum of the squares of the differences between the measured and calculated wet antenna attenuation is at a mimnimum. Only values where at least one of the rain gauges measures a nonzero rainfall intensity and where the apparent wet antenna attenuation is positive are used in the analysis.

The resulting coefficient and exponent are $\gamma = 2.06 \times 10^{-5}$ m mm$^{-\delta}$ h$^{\delta}$ and $\delta = 0.24$. Figure 6.4 shows the wet antenna attenuation resulting from this fit ($A_{\text{a,fit}}$) as a function of the "true" (i.e., resulting from measurements, $A_{\text{a,true}}$) wet antenna attenuation. It is clear from this figure that there is a significant amount of scatter about the fit ($r^2 = 0.33$) and that there are some outliers. This may partly be explained by the fact that there are gauges only at a few points along the 4.89 km link, the gauge closest to one of the antennas is 0.43 km away, and the fact that the $R - k$ relation at 27 GHz is slightly non-linear. Because of this, spatial variations in rain may cause part of the
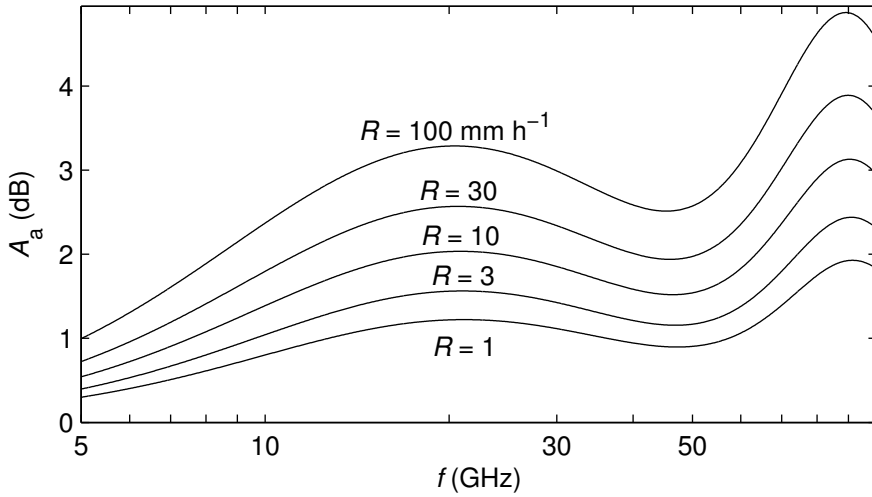
Figure 6.5: Wet antenna attenuation A_a as a function of signal frequency for different rainfall intensities.

scatter in Figure 6.4. Another reason may be that the water on the antennas does not form a perfectly flat film. This causes the antenna patterns, and hence the received signal level to change. The dependence of the wet antenna attenuation on wind speed and direction (analyses not shown here) is negligible for the data set under consideration. A more in-depth investigation into wetting of antennas is required to give a more accurate description of these effects, but this is beyond the scope of the current study.

Figure 6.5 shows the relation between wet antenna attenuation and frequency for different rainfall intensities for a single antenna. It is apparent from this graph that there is significant wet antenna attenuation for all intensities. The increase of attenuation with rainfall intensity is greatest at small rainfall intensities. This means that it is important to know when it rains and when the antennas become dry, as the difference in wet antenna attenuation is quite large (using this approximation for wet antenna attenuation). These observations can also be made from Figure 6.6, where wet antenna attenuation at 27 GHz is shown as a function of R. For comparison, the wet antenna attenuation resulting from an empirical relation used in Chapter 3, which was fit on the data described in Section 6.2.2 (i.e. the same data that were used to fit the $l - R$ relation of Eq. (6.4)) is included in the figure. It can be seen that the two relations are quite similar for low rainfall intensities, but significant deviation occurs at higher intensities. However, as the relative contribution to the total attenuation of the wet antenna attenuation is much greater at low rainfall intensities, deviations at higher intensities are relatively less important.
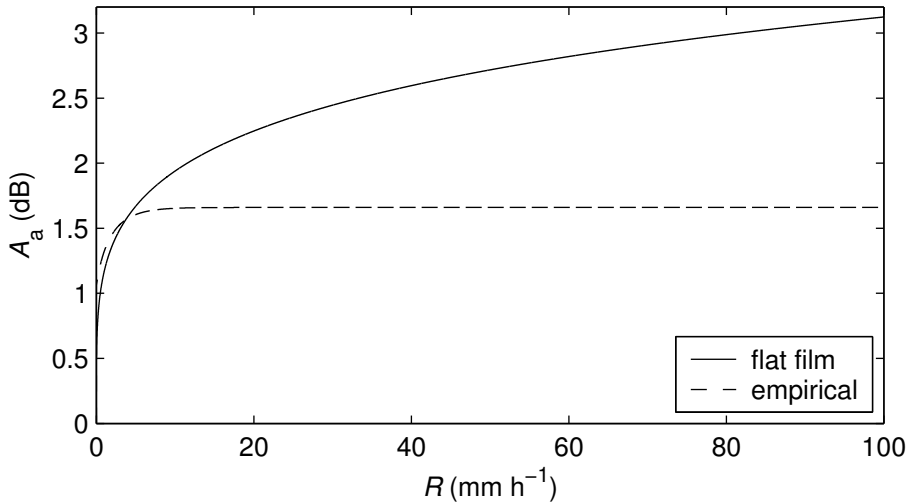
Figure 6.6: Wet antenna attenuation A_a as a function of the rainfall intensity at 27 GHz. Shown are the current method (flat film) and an older method (empirical).

6.3.2 Correction for wet antenna attenuation

Microwave link signals can be corrected for wet antenna attenuation. The method used in this chapter assumes that the rainfall intensity is constant over the entire link, and that the relation between the rainfall intensity and wet antenna attenuation is perfectly known (i.e., the constants γ and δ are the "true" values). The total attenuation is the sum of the path-integrated attenuation by raindrops in the path of the links and twice (two antennas) the wet antenna attenuation.

$$A_{\mathrm{m}} = L\left(\frac{R}{a}\right)^{1/b} + 2A_{\mathrm{a}}(R) \tag{6.5}$$

As both of these quantities are functions of the rainfall intensity, R can be determined by (implicitly) solving this equation. Of course, errors are introduced when the rainfall intensity is not the same over the two antennas and along the link. This will be investigated in Section 6.5.3. Note that this correction cannot be used on the radar data, as the relation between l and R depends on the antenna type.

The ratio of the first term to the second term of Eq. 6.5 for a 1 km link is shown in Figure 6.7 as a function of link frequency and rainfall intensity. Note that values for different link lengths can be obtained by simply multiplying the values in Figure 6.7 with the link length. It can be seen that the attenuation caused by the wetting of the antennas dominates that caused by rain along the path for low rainfall intensities and at low frequencies. The frequency for
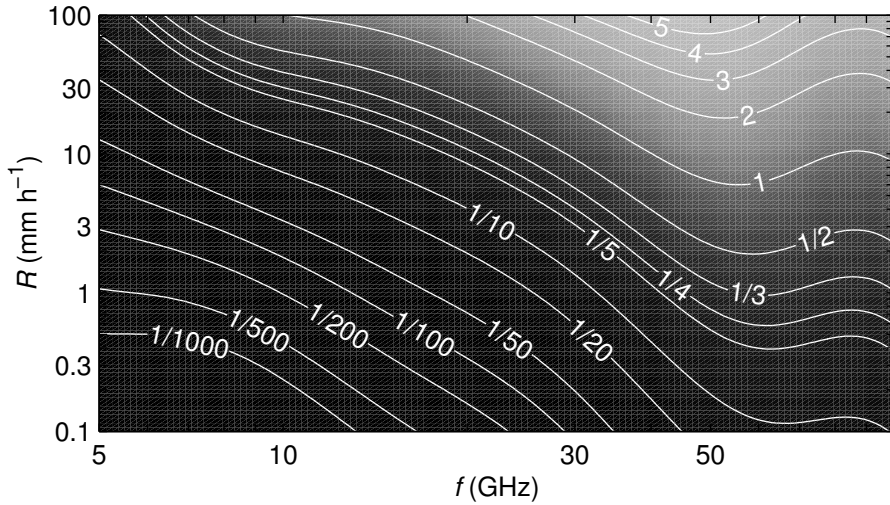
Figure 6.7: Ratio of rain-induced attenuation to wet antenna attenuation as a function of signal frequency and rainfall intensity for 1 km links.

which the ratio has a maximum for a given R depends somewhat on R itself, but is seen to be in the range $f > 45$ GHz.

6.4 Space-time structure of rain

The length and time scales of rain events are very important variables to know for understanding the dependence of errors on link length and sampling strategy. If most of the variation in rainfall occurs within a link (i.e., if the link is much longer than the typical length scale of rainfall events), the relation between rainfall intensity and specific attenuation will have to be very close to linear in order to give accurate estimates of path-averaged rainfall intensity. On the other hand, if the variation in rain is small along an entire link, this requirement of near-linearity is much less stringent. The same applies to the interplay between sampling intervals or averaging times and the typical temporal scales of rain events.

The length and time scales of rainfall have been independently investigated using the data set described in Section 6.2.1 (i.e., the range bins between 0.96 and 10.08 km from the radar in the selected radial). For the length scales of rain, the autocorrelation function of the rainfall intensity has been computed for each time step in the data set. The charateristic length scale of rain is defined to be the e-folding distance (i.e., the distance over which the autocorrelation reduces to $e^{-1} \approx 0.37$). Characteristic time scales are computed in the same manner, where the autocorrelation function is computed for each of the 332 events, for each range bin. Figure 6.8 shows the empirical probability density
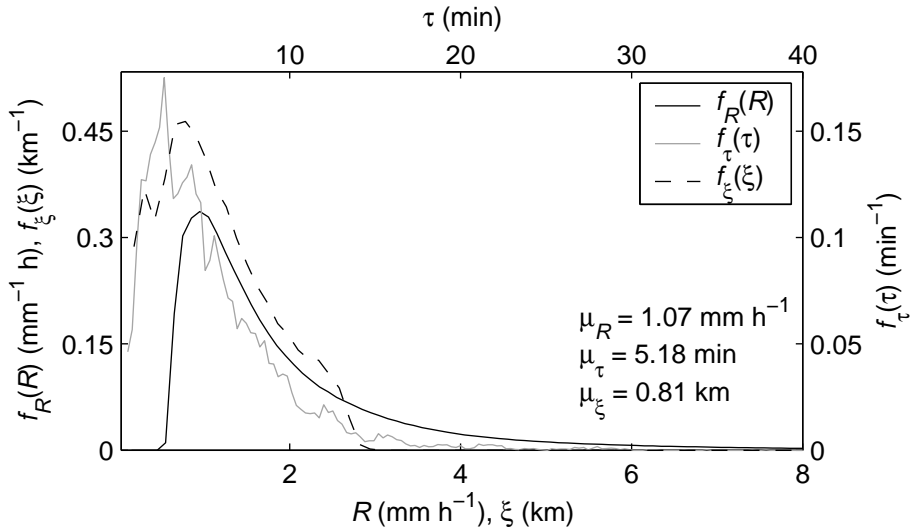
Figure 6.8: Empirical probability density functions of intensity R, characteristic time scale τ, and characteristic length scale ξ of rainfall events under consideration. Zero values are not shown, and the R, τ and ξ axes are cut off so that the maximum values are not shown in this graph. Zeroes have been included for the computation of means.

functions of the characteristic length (ξ) and time (τ) scales computed for the entire data set in this way. It can be seen here that the typical temporal scales are mostly below 10 min, with a mean of approximately 5 min. The typical spatial scales are mostly below 2 km, with a mean of 0.8 km. These values are both quite small, and as a result, it is expected that if a moderately nonlinear $R - k$ relation is needed for the considered link frequency, links should be very short ($1 - 2$ km), and they should be sampled at least once every few minutes.

The time scales of path-averaged rainfall intensities are also important for this chapter. Analyses of the mean characteristic times of rain events for rain averaged over paths of different lengths are shown in Figure 6.9. The mean characteristic times show a nearly linear increase with the path length. This means that for longer microwave links, constraints on the sampling frequency should be less stringent than for short links, as was to be expected. It is also shown that the mean path-averaged rainfall intensity is nearly independent of the path length, which is a result of the corrections described in Appendix A.
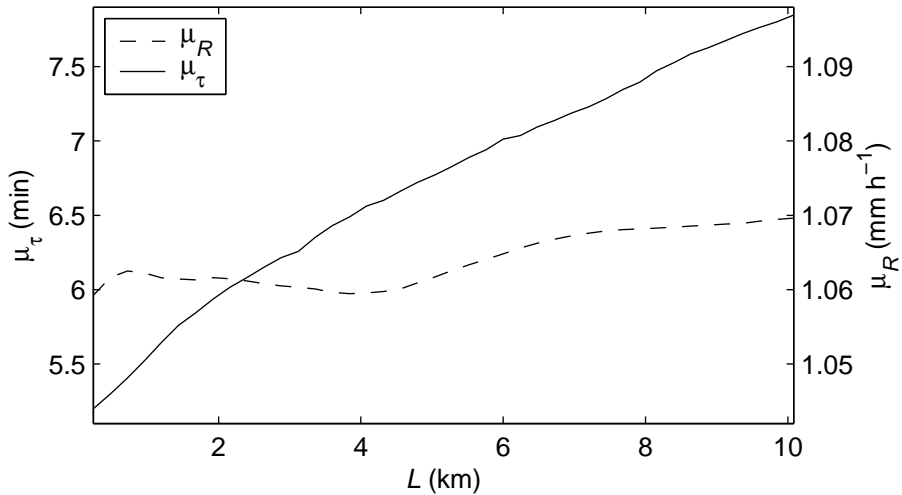
Figure 6.9: Means of rainfall itensities μ_R and characteristic times μ_τ of path-averaged R as a function of the path length.

6.5 Results and discussion

6.5.1 Effects of link length and frequency, temporal sampling and power resolution

If the sampling of link signals is not (quasi-) continuous, errors may result because of temporal variations in the rain that are not captured by the link. If the link signals are sampled continuously, but only time averages are stored, the same temporal variations may cause errors due to the nonlinearity of $R - k$ relations. Here link signals are simulated with three different sampling strategies:

1. *Continuous.* The link signal is converted to a rainfall intensity at every timestep, after which these values of R are averaged over 15 minutes. This is common when using research microwave links (see e.g. *Ruf et al.*, 1996; *Rincon and Lang*, 2002; *Rahimi et al.*, 2003, and Chapter 3).

2. *Averaged.* The link signal is averaged over 15 minutes, after which this time average is converted to a value of R. This is common in commercial cellular communication link monitoring (see *Messer et al.*, 2006).

3. *Intermittent.* The link signal is sampled only once every 15 minutes, in the middle of the averaging periods mentioned above. This is also encountered in commercial cellular communication link monitoring (see Chapter 4).

Figure 6.10: Normalized MBE (%) as a function of link frequency and length, for different sampling strategies and power resolutions. White areas indicate zero total link-estimated rain (over the entire data set).

The 15-minute periods mentioned above have been selected based on the local clock time (0, 15, 30 and 45 minutes after the hour), so that the starting times of the periods considered are independent of the onset of rainfall (see also Appendix A.3). All of the resulting 15-minute link-estimates of R are compared to the same 15-minute averaged true R.

If the resolution of the recorded link signal is limited (e.g., 1 dB), this may cause rounding errors. The severity of these rounding errors depends on the amount of total attenuation relative to the power resolution. If the path-integrated attenuation is low due to low rainfall intensities, short links or low sensitivity due to low link frequency (see also Figure 6.3), the rounding errors may dominate. Here the effect of having a power resolution of 1 dB, which is typical for commercial cellular communication links (see *Messer et al.*, 2006, and Chapter 4), is investigated.

Simulation results are shown in Figures 6.10 and 6.11 (MBE and RMSE, respectively). In the perfect case (i.e., continuous sampling and no rounding of power levels), errors and uncertainties increase with link length at frequencies where the $R - k$ relation deviates from linearity (see Figure 6.3). This can be explained by the increase in variation in R along the link for increasing link lengths (see Figure 6.8), which causes nonlinearities in relations to yield erroneous path-averaged values.
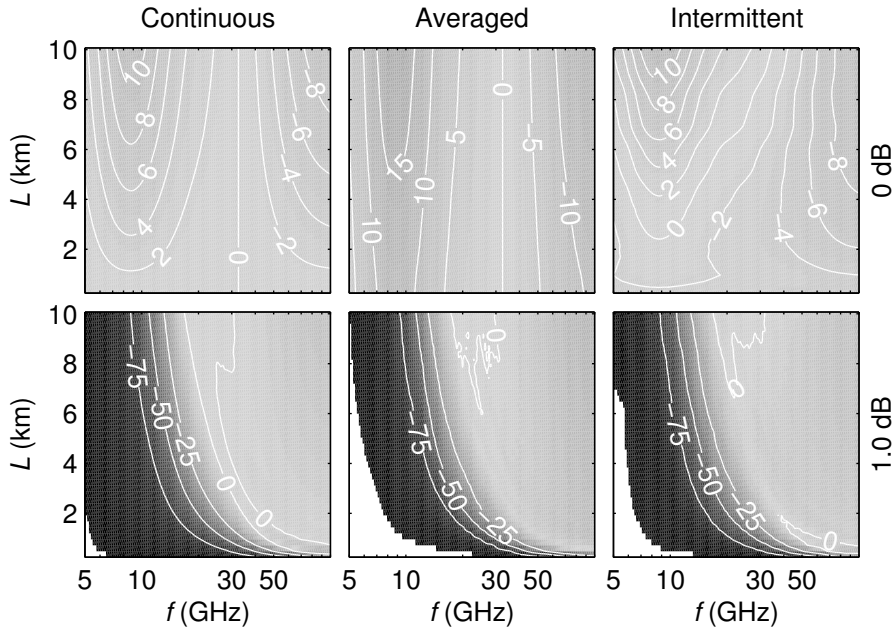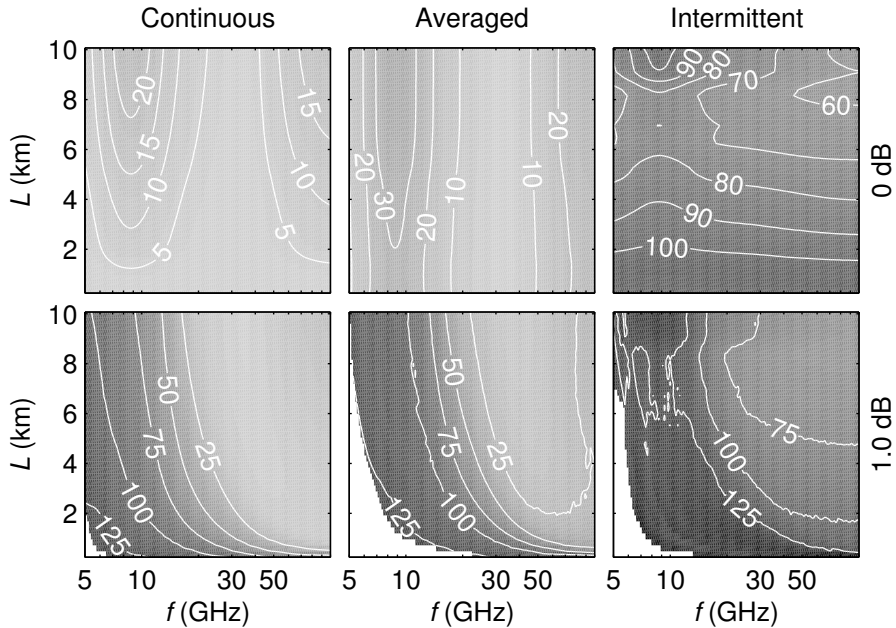
Figure 6.11: Normalized RMSE (%) as a function of link frequency and length, for different sampling strategies and power resolutions. White areas indicate zero total link-estimated rain (over the entire data set).

The degradation of the power resolution can be seen to cause severe errors and uncertainties for short links and at low frequencies. This is to be expected as the total path-integrated attenuation is smallest in these regions, so that the effect of rounding is large. However, for longer links and at higher frequencies, this is not the case. The differences in MBE between three temporal sampling strategies can be seen to be minor. The largest differences exist between the averaged and the other two strategies. These differences decrease with link length, which can be expected as the characteristic times of path-averaged rainfall intensities increase with the length of the path (see Section 6.4). The expected inferior performance of the instantaneous sampling strategy only becomes apparent when examining the RMSE. This clearly shows that this is not a good sampling strategy, and that time averages of path-integrated attenuation should always be preferred if continuous measurements are not available.

6.5.2 Effects of wet antenna attenuation

In Figures 6.12 and 6.13, normalized MBE and RMSE, respectively, are shown as a function of frequency and link length for the different sampling strategies and power resolutions considered in Section 6.5.1, when the effect of wet antennas is included in the simulated microwave link signal. Wet antenna at-
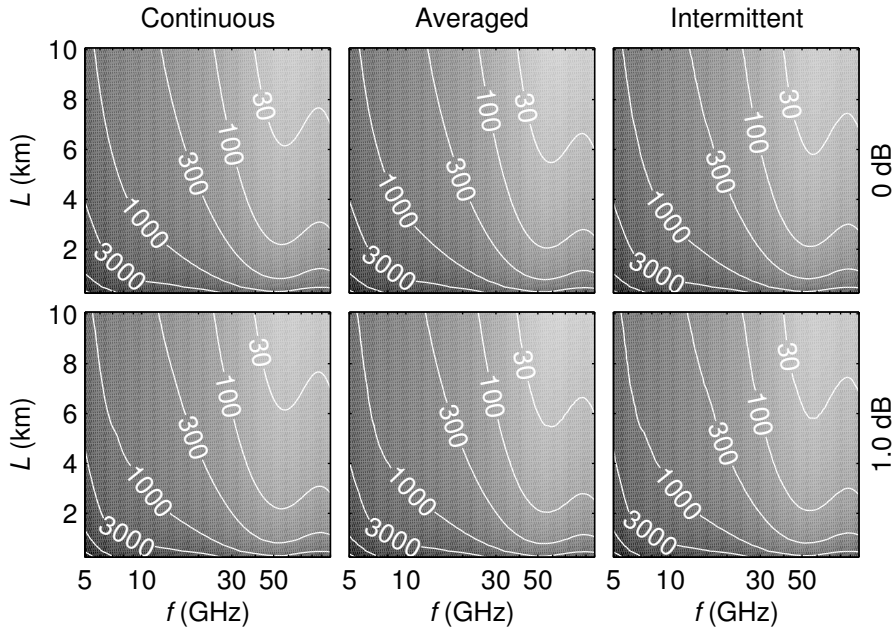
Figure 6.12: As Figure 6.10, but including wet antenna attenuation. Gray scale is logarithmic.

tenuation is seen to cause both large bias and large uncertainties. Because wet antenna attenuation is relatively larger than path-integrated attenuation at low frequencies and for short links (see Figure 6.7), the errors are worst in this region. Links that are longer than the characteristic length scales of rain events have a higher probability of having one or both of the antennas in a dry region, which greatly reduces error statistics. Errors are also less severe because long links experience more path-integrated attenuation relative to wet antenna attenuation simply because the path is longer. However, even if a link is very long, and if the frequency is chosen such that the ratio of path-integrated attenuation to wet antenna attenuation is minimal (i.e., $f \approx 50$ GHz, see Figure 6.7), it is higly desirable to somehow correct for wet antenna attenuation. The sampling strategy and power resolution is seen to be of very little influence as the errors caused by wet antennas are much larger. Only in the region where these errors are limited (high frequencies, long links) a slight difference can be seen, especially in the normalized RMSE (see also Figure 6.11).

6.5.3 Effects of correction for wet antenna attenuation

Figures 6.14 and 6.15 show the normalized MBE and RMSE, respectively, for link signals that suffer from wet antenna attenuation and where the correction algorithim as described in Section 6.3.2 has been applied.
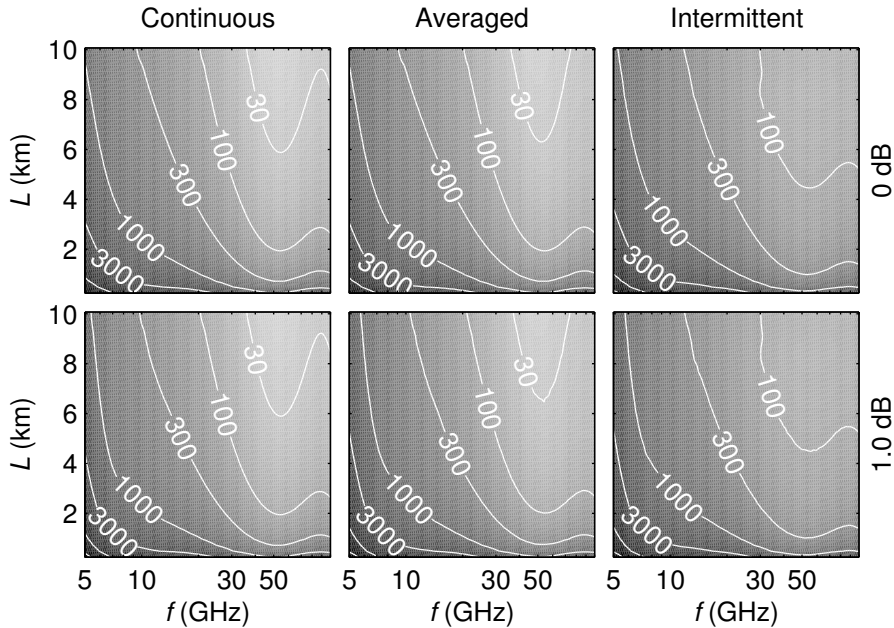
Figure 6.13: As Figure 6.11, but including wet antenna attenuation. Gray scale is logarithmic.

If the correction method presented in Section 6.3.2 is used, a systematic underestimation of path-averaged rainfall intensities can be seen, except for extremely short links. Especially the rainfall intensity based on the time-averaged specific attenuation is lower than the "true" R. This systematic underestimation is caused by the same mechanisms that limit the errors when the uncorrected signal is used. If the rainfall intensity at the two antennas is different from that along the link, the assumptions on which the correction method is based are no longer valid. If one or both of the antennas are dry, the correction algorithm will correct for a phenomenon that does not occur, and hence it will underestimate the path-averaged R. This is the reason why the negative bias (MBE) becomes more pronounced with link length for the continuous and intermittent cases. When the specific attenuation is not only averaged in space, but also in time, the negative bias becomes less pronounced with link length. This is caused by the fact that temporal averaging removes dry periods, which are more abundant in short links, so that the severity of errors will decrease.

It is interesting to note that the degradation of the power resolution has less effect than if no wet antenna attenuation is considered. This is due to the fact that the total attenuation is higher, especially in the low-frequency region, where the wet antenna attenuation is large relative to the path-integrated attenuation (see Figure 6.7). In fact, at these low frequencies, it is not the path-integrated attenuation but the wet antenna attenuation that is mainly used to

Figure 6.14: As Figure 6.10, but including wet antenna attenuation, and correction for it. Gray scale is logarithmic in areas where the normalized MBE is greater than 50% (i.e., areas in the bottom panels where $f <$ 5.75 GHz).

estimate rainfall intensity, which in that case is not so much the path-averaged R as the two-point averaged R. It is only at the very low frequencies where errors and uncertainties increase due to power resolution degradation. Nearly the same holds for the variation (RMSE), where the only differences occur at low frequencies. The high RMSE for the intermittent sampling strategy for all link frequencies and lengths suggests that this is not a good temporal sampling strategy. Of course, the continuous strategy is to be preferred, but if this is not possible, averaged values of A_{m} may still yield good results if the frequency is around 40 GHz (which is between the frequency where the $R - k$ relation is linear and where the wet antenna attenuation has a minimum), especially for longer links.

It is clear that the correction for wet antenna attenuation greatly improves results. Hence it is recommended to apply such a correction in microwave link rainfall estimation. This also shows that it is important to more closely investigate the effects of wet antenna attenuation.

It is important to note here that the relations used for the retrieval of R from the simulated microwave link signals are the same as those used for the simulation of these signals. Therefore, the results presented in this chapter are "best case scenarios", as no errors in these relations are considered.
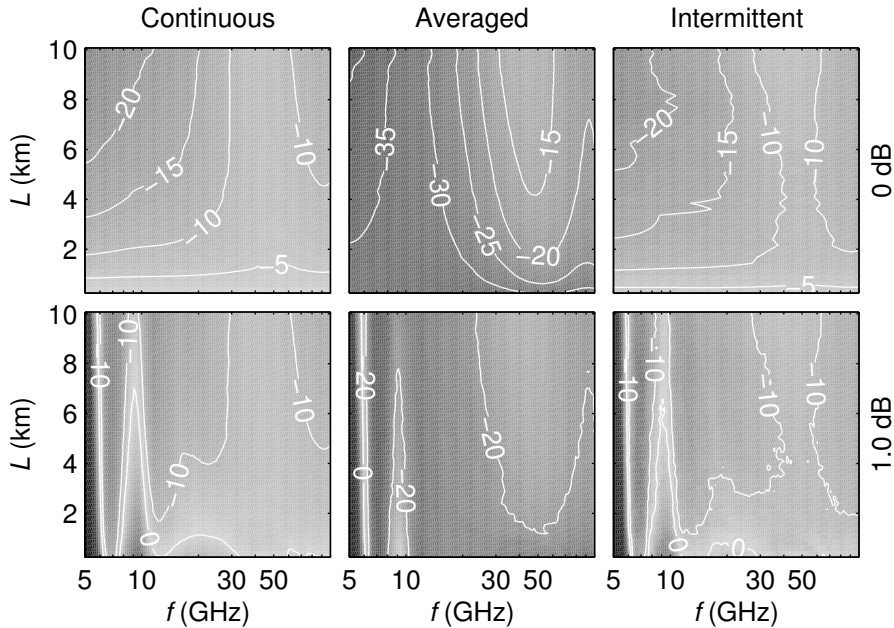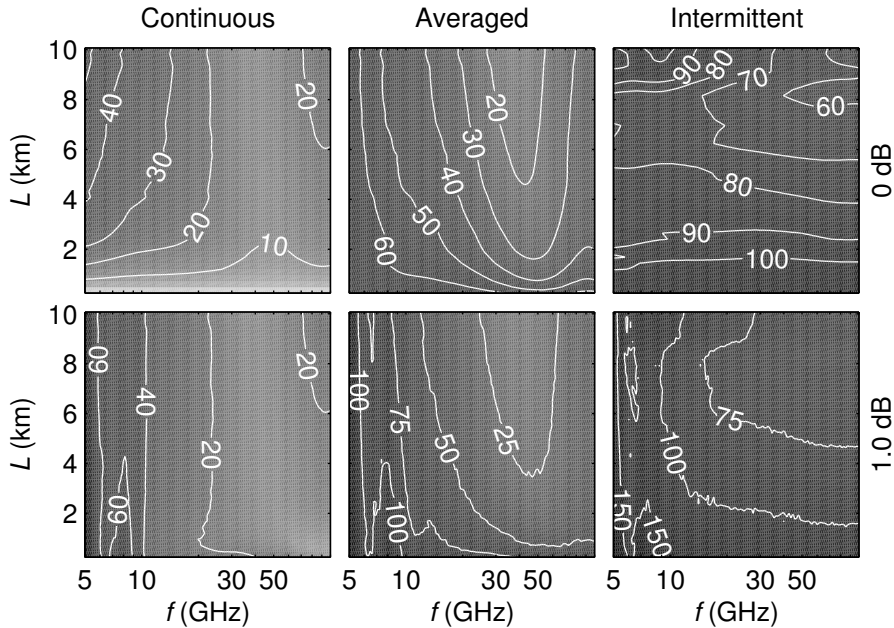
Figure 6.15: As Figure 6.11, but including wet antenna attenuation, and correction for it. Gray scale is logarithmic.

6.5.4 Two events

In order to study the effect of different phenomena on separate events, analyses of two events are shown in more detail. Link signals have been simulated for two 5 km links, with frequencies commonly used in commercial cellular communication: 18 GHz (*Messer et al.*, 2006) and 38 GHz (Chapter 4). The two events that are analyzed are a low-intensity event (15 May, 1993) and a high-intensity event (8 September, 1993). Examples of profiles for these events have been shown in Figure 6.2. The effects of power resolution, wet antenna attenuation and correction for wet antenna attenuation on the retrieved rainfall intensities for the two frequencies under consideration can be seen in Figures 6.16 and 6.17.

For both events, the retrieved R for the link measurements without wet antenna attenuation can be seen to be very close to the true path-averaged R. However, for the low-intensity event (see Figure 6.16) the effect of the degradation of the power resolution is very large for the 18-GHz link: no rain is estimated. This is less severe for the more sensitive 38-GHz link, where there is some error, but the link estimate follows the true R. This effect is much less pronounced for the high-intensity event (see Figure 6.17). The total attenuation reached such high values in high rainfall intensities that rounding of received power has a relatively small effect. The effect of wet antenna attenuation is also seen to be most pronounced for the low-intensity event and at 18 GHz,
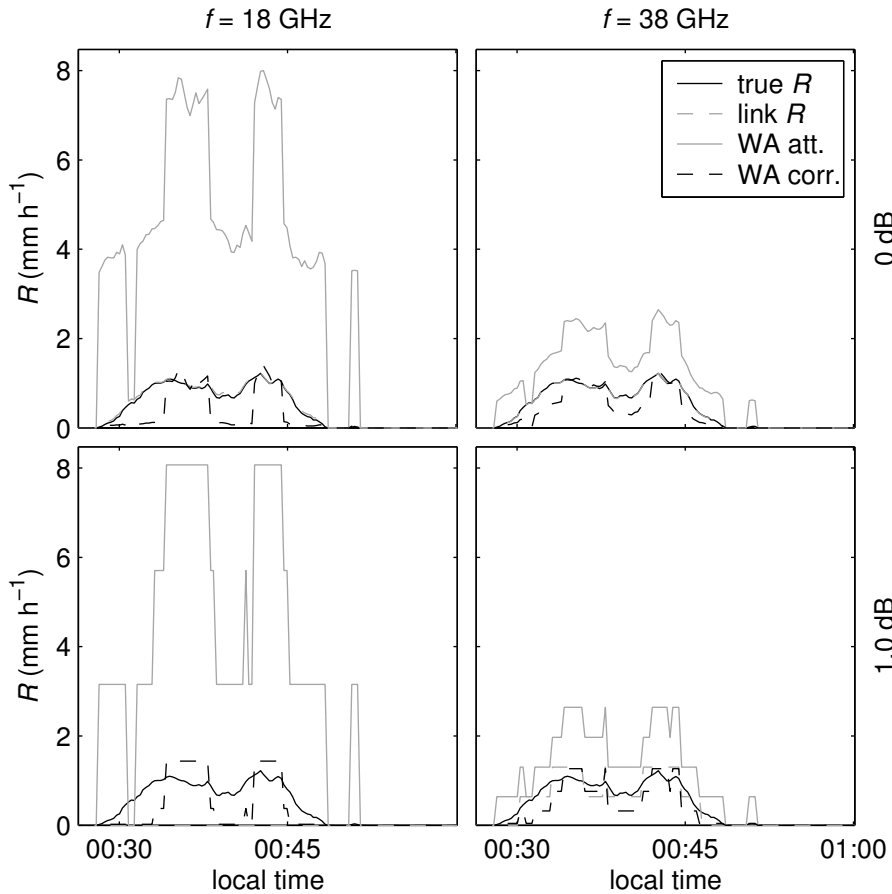
Figure 6.16: Microwave link rainfall estimates from different link settings (power resolution and frequency) compared to true path-averaged R (true R) for an event on 15 May, 1993. Microwave link signals are simulated without wet antenna attenuation (link R) and with wet antenna attenuation. In the latter case, correction for wet antenna attenuation is (WA corr.) and is not (WA att.) applied.

which is to be expected from the analysis of Figure 6.7. The correction for wet antennas yields a more noisy time series than the true path-averaged R, but the overall amounts are similar. This noise can be explained by the fact that the total attenuation is partly due to the rainfall intensity at two points, whereas the path-averaged R is a true path average.
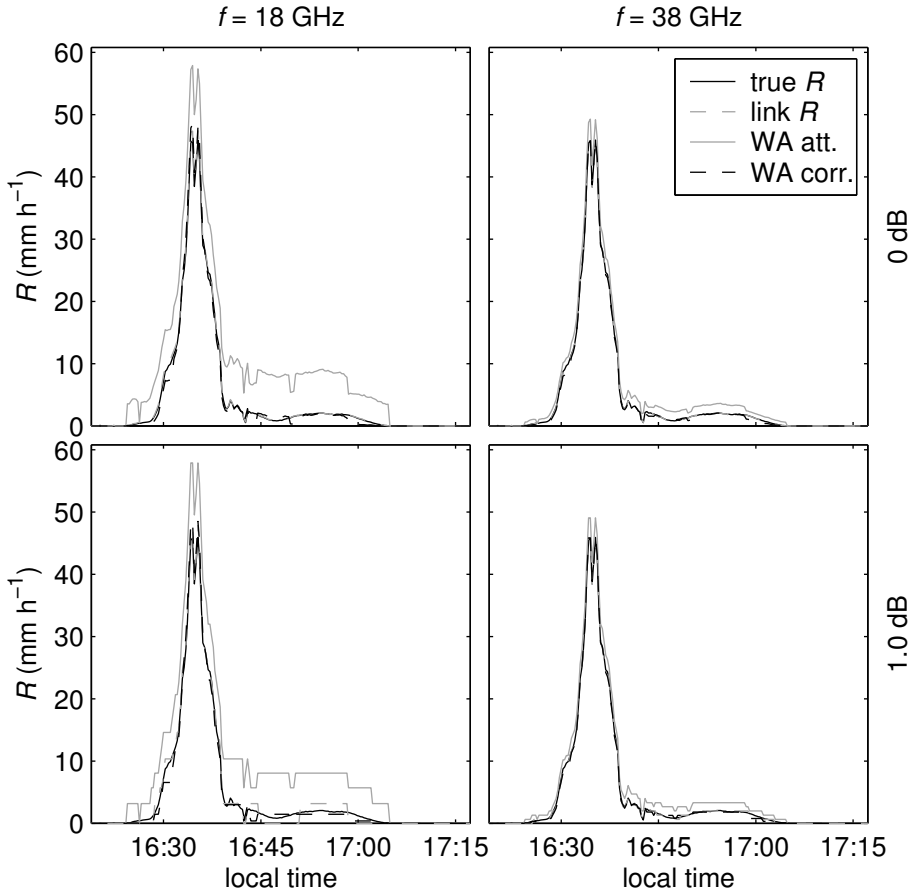
Figure 6.17: As Figure 6.16, but for an event on 8 September, 1993.

6.5.5 Errors and uncertainties in actual link measurements

For comparison with the presented simulations, the actual microwave link measurements described in Chapter 3 and Section 6.2.2 have been used to compute normalized MBE and RMSE in the same manner as described in Section 6.2.3. In this case, the "true" rainfall intensity is assumed to be that measured by the rain gauges. Hence, is is expected that the errors will be more severe in this case, as there are more sources of error (e.g., deviations from the assumed $R-k$ power law and system noise) involved than considered in the simulations. Link signals both uncorrected and corrected for wet antenna attenuation have been considered. This correction has been carried out as described in Section 6.3.2 (i.e., not as in Chapter 3). The three sampling strategies and the two power

resolutions as described in Section 6.5.1 have been employed here as well.

Table 6.2 shows the normalized MBE and RMSE of microwave link measurements for different sampling strategies and power resolutions, both corrected and uncorrected for wet antenna attenuation. As a comparison, the values of normalized MBE and RMSE resulting from the simulations (see Figures 6.12-6.15) for 27 GHz and a link length of 4.89 km are also given. Both the MBE and RMSE for the uncorrected cases are higher for the measured data than for the simulations, which is to be expected. However, both the measured and simulated results show the same dependence on the temporal sampling strategy and power resolution. The consistently higher MBE for the measured data that is corrected for wet antenna attenuation is likely caused by the fact that there is some drift and noise in the base level of the signal (see Chapter 3). As the values of attenuation that are below 0 dB (which is not possible for the simulated data) are set to 0 dB, this may result in a higher mean link-estimated R. Again, the same dependence on temporal sampling and power resolution can be observed. This is also the case for the normalized RMSE for the wet antenna attenuation-corrected data. Hence these analyses lead to similar conclusions regarding temporal sampling, power resolution, and correcting for wet antennas as those drawn in Sections 6.5.1–6.5.4.

6.6   Conclusions

Data from a high-resolution X-band weather radar, recorded over more than 1.5 years, have been used to investigate the errors and uncertainties in microwave link rainfall estimates. In this study, the effects of sampling strategy, power resolution and wet antenna attenuation have been considered for a range of link lengths and frequencies. In order to examine the effect of wet antenna attenuation, a simple parametric method to compute wet antenna attenuation

Table 6.2: Normalized MBE and RMSE (both in %) for microwave link measurements (denoted by (meas)) compared to values resulting from simulations (denoted by (sim)). Results are shown with and without correction for wet antennas (correction for this is denoted by the subscript corr).

	continuous		averaged		intermittent	
	0 dB	1.0 dB	0 dB	1.0 dB	0 dB	1.0 dB
MBE (meas)	287	287	297	283	292	292
MBE (sim)	163	161	165	162	160	159
MBE$_{corr}$ (meas)	-6	-6	8	-10	1	1
MBE$_{corr}$ (sim)	-10	-10	-21	-21	-13	-13
RMSE (meas)	232	232	228	249	324	324
RMSE (sim)	129	129	128	135	180	183
RMSE$_{corr}$ (meas)	93	93	92	94	161	161
RMSE$_{corr}$ (sim)	17	17	28	32	78	80

has been proposed and calibrated using microwave link and rain gauge data.

Wet antenna attenuation can be roughly approximated by assuming that there is a perfectly flat film of water on the antenna. The thickness of this film depends on the rainfall intensity. A power-law relation between these two variables has been suggested in this chapter. This power law has been calibrated using an experiment with a microwave link and a line configuration of rain gauges. The relation is seen to be far from perfect, which can be explained by the imperfect estimation of path-averaged and point rainfall intensities by the gauges (at the antennas), and by the violation of the assumption of there being a flat film of water on the antennas. Correction for wet antenna attenuation can be done by (implicitly) inverting the relation between rainfall intensity and wet antenna attenuation.

Using profiles of rainfall intensities derived from radar data an analysis of the spatial and temporal variation of rain to be expected along microwave links was performed. The means of the characteristic space and time scales of all rain events in the data set are 5.2 min and 0.8 km, respectively. This means that the nonlinearity of the $R - k$ relation that is used becomes important for very short links, and at time scales in the order of a few minutes. Of course, these values of characteristic scales are climatological averages for Dutch conditions, so that for certain events these scales may be even shorter. The characteristic time scale of path-averaved rainfall intensity increases linearly with the length of the link. Therefore the errors and uncertainties related to the temporal sampling are expected to be worse for short links than they are for long links.

Errors and uncertainties that occur for different sampling strategies found in the literature have been examined, as well as those caused by degradation of the resolution of the recorded power. The effect of the degraded power resolution is seen to be greatest, and to dominate other sources of error, at low link frequencies and for short links. However, for longer links and at higher frequencies, this power resolution is much less of a problem. Here errors related to nonlinearities in $R - k$ relations and sampling strategy dominate. The errors and uncertainties related to nonlinearities in these relations are limited, but certain frequencies (around 35 GHz, where the $R - k$ relations are close to linear) are to be preferred. It is clear that if continuous samples of path-integrated attenuation are not available, time averages should be preferred over instantaneous measurements.

It has been shown that wet antenna attenuation causes very large errors and uncertainties that dominate all other sources of error. The effect is most pronounced at high frequencies, where wet antennas cause relatively more attenuation than rain along the path does. But, for all link lengths and frequencies, it is important to correct for this phenomenon.

The systematic underestimation of path-averaged R that is seen from wet antenna attenuation-corrected simulation results, especially for longer links, is the result of correction for a phenomenon that does not always occur. For small-scale rain events, it may rain between, but not on the antennas. This effect is enhanced, and can be quite severe for the averaged sampling strategy, where dry periods are removed by temporal averaging. The uncertainties are

again much worse for the intermittent sampling strategy than for the other two, confirming the previous conclusion that if continuous samples of path-integrated attenuation are not available, time averages should be preferred over instantaneous measurements. The effect of the degradation of the power resolution is smaller than in case wet antenna attenuation is not considered, simply because there is more attenuation.

Errors and uncertainties from simulation results have been compared to those from data measured using a microwave link and rain gauges. The absolute errors and uncertainties are different, which is to be expected as there are more sources of error than those that were modeled. However, the dependence on temporal sampling, power resolution and wet antenna attenuation correction are similar. Hence, regarding temporal sampling, power resolution, and correction for wet antennas, the conclusions drawn from the actually measured data are the same as those drawn from the simulation results.

From the analyses presented in this chapter, it can be concluded that the errors and uncertainties related to power resolution and wet antenna attenuation are limited (i.e., MBE and bias-corrected RMSE are $> -20\%$ and $< 20\%$ of the mean rainfall intensity, respectively) if certain conditions are met. These conditions are that wet antenna attenuation should be corrected for and that the frequency and length of the link should be greater than ~ 20 GHz and ~ 2 km, respectively. It is also clear that the continuous sampling strategy is the best strategy, but if this is not available, the averaged strategy is to be preferred over the intermittent strategy.

CHAPTER 7

Synthesis

7.1 Conclusions

Measurement of both evaporation and precipitation (i.e. the total vertical water flux at the land-atmosphere interface) on a regional scale is important for many purposes, e.g. in hydrology and water management, and in meteorology. Both of these water fluxes can in principle be measured using a single instrument: the microwave link. Microwave links typically operate at path lengths of a few kilometers, yielding path-averages of evaporation and precipitation at this scale. As this scale is the scale of interest of many applications, microwave link measurements offer a clear advantage over point-scale measurements. Other instruments have disadvantages that make their measurements potentially less accurate than those from microwave links. However, microwave links are by no means perfect. Therefore microwave links, like all other instruments, will be of most benefit if used in combination with other instruments. There is great potential for the use of microwave links from (very dense) existing commercial cellular communication networks, especially for the estimation of rainfall, which makes reseach on these instruments highly worthwhile and relevant.

It has been shown in this thesis that microwave links are highly suitable for the measurement of both evaporation and precipitation if certain criteria are met and some corrections are applied to the data. Especially the very dense networks of microwave links used for commercial cellular communication offer great potential for operational monitoring of these water fluxes. However, especially for the measurement of evaporation, more research is neccesary before this can be implemented. Suggestions for future research are given in Section 7.2. More detailed conclusions that can be drawn from the work presented in this thesis follows below, separated in conclusions about the estimation of

evaporation (Section 7.1.1) and rainfall (Section 7.1.2).

7.1.1 Evaporation

Evaporation can be estimated from microwave link measurements when the instrument is used as a scintillometer. The water vapor transported into the atmosphere by turbulent eddies causes the refractive index of air (at microwave frequencies) to fluctuate. These fluctuations cause the received microwave link signal to fluctuate as well. Besides these signal fluctuations, the estimation of evaporation requires measurements of wind velocity, net radiation, and ground heat flux (although this variable could also be estimated from the net radiation, see e.g. *Idso et al.*, 1975). It also requires an estimate of the effective vegetation height and the correlation coefficient between temperature and humidity fluctuations (r_{TQ}). Sensitivity analyses (see Section 2.3.2) have shown that the estimate of the effective vegetation height may be a rough one. The errors introduced when erroneously assuming $r_{TQ} = 1$ are limited (see Section 2.3.3), especially under relatively wet conditions (i.e. Bowen ratio $\beta \leq 2$).

Using data from an experiment with a 27-GHz microwave link performed under relatively wet conditions, it has been shown in Chapter 2 that it is possible to estimate evaporation on a regional scale relatively accurately. Measured values of the structure parameter of the refractive index of air (C_n^2) are often too large, which is caused by either wind-induced vibrations of the masts to which the antennas have been attached or scattering of the signal off vegetation moving in the wind (see Section 2.3.3). This is a serious problem associated with microwave link estimation of evaporation, which should be investigated more closely. However, the method that is used to estimate evaporation from microwave link measurements has a built-in quality control of the measurem-tents in the sense that "impossible" values of C_n^2 are easily detected (see Section 2.3.1). The solution to the system of equations that is used to compute evaporation from microwave link measurements may not be unique (i.e. there may be multiple values of the latent heat fluc ($L_v E$) for a single set of values of C_n^2, the total available energy ($R_n - G$), the wind velocity (u), the effective average vegetation height (h_0), and r_{TQ}). It has been assumed in this thesis that the correct solution is that for "wet" (i.e. Bowen ratio smaller than $\beta \approx 2$) conditions. However, in dry conditions, this assumption may not be valid. Hence measurement of evaporation using a microwave link works best under relatively wet conditions, and care should be taken in the interpretation of estimates of evaporation in dry conditions.

7.1.2 Rainfall

The measurement of rainfall using a microwave link is based on the fact that raindrops attenuate the signal. Using point-scale measurements (taken at two locations in The Netherlands with two different instruments) as well as simulations (based on intense Mediterranean rainfall) of drop size distributions (DSDs), power-law relations between the rainfall intensity (R) and the spe-

cific (k) and differential (Δk, in the case of dual-frequency and/or polarization links) attenuation have been derived, where the signal frequency (or combination of frequencies) was varied. Such deterministic power laws (in the sense that the scatter around them is neglected) have been shown to be adequate for the estimation of rainfall in Chapter 5. For single-frequency links the relation is close to linear between 25 and 40 GHz, which is ideal for path-integrated measurements. At these frequencies the retrieved rainfall intensity is relatively insensitive to the rain temperature and canting angles of raindrops. Within one DSD climatology, link-estimated rainfall intensities are also relatively insensitive to the variability of the drop size distribution. However, application of an $R - k$ relation derived for a different climatology, such as those proposed by *ITU-R P.838-3* (2005), may lead to errors. For dual-frequency links it has been suggested in Chapter 5 that one of the frequencies should be chosen such that it is the optimal frequency (i.e. $R - k$ relation is linear) for a single-frequency link. The second frequency should not be too far away from the first, as the added value of a second signal would become smaller if the frequency separation would be too great.

It has been experimentally demonstrated in this thesis that microwave links are highly suitable for estimation of path-averaged rainfall, both in a research setting (Chapter 3) and using data from links constituting commercial cellular communication networks (Chapter 4). To show that both fluxes could indeed be measured using a single instrument, the experiment with the research microwave link was conducted with the same 27-GHz instrument that was used to measure evaporation in Chapter 2. Several issues with microwave link rainfall estimation have been raised: (1) drift in signal base level; (2) limited dynamic range; (3) the interplay of the micro- and macrostructure of rainfall and the nonlinearity of $R-k$ relations; and (4) wet antenna attenuation. For microwave links from commercial cellular communication networks, additional issues are: (5) rounding errors caused by limited power resolution (typically 1 dB); and (6) limited sampling rate of the signal (typically 4 h^{-1}).

The drift in signal base level (issue (1)) could be caused by both atmospheric and electronic phenomena. An attempt has been made to remove some of this drift by removing effects of attenuation by water vapor and effects of possible temperature-related drift in electronics. However, more detailed analyses are needed to resolve this issue. The limited dynamic range of the receiver (issue (2)) is only a limiting factor for the maximum measurable total attenuation (and hence path-averaged rainfall intensity) before the signal becomes undetectable. If the combination of link length and frequency is chosen carefully, problems could be avoided. Issues (3)-(6) have been investigated more closely in a simulation framework, where microwave link signals have been simulated using measured drop size distributions and radar data.

To investigate the effect of the microstructure of rainfall on link-estimated rainfall intensities (part of issue (3)), time series of measured DSDs in combination with wind velocity measurements and Taylor's hypothesis have been used to simulate profiles of k and R in Chapter 5. These profiles, as well as k and R profiles computed from simulated profiles of DSDs based on intense

Mediterranean rainfall have been used to simulate microwave link signals and the corresponding "true" path-averaged rainfall intensities. It is clear from the comparison of the retrieved and "true" rainfall intensities that if the frequency of the link is such that the $R - k$ relation is close to linear, both systematic errors and uncertainties are limited. Bias in the retrieved rainfall intensities is found to increase somewhat with link length, whereas uncertainties decrease slightly with link length.

High-resolution radar data recorded over more than 1.5 years have been used in Chapter 6 to investigate the effect of the interplay between the spatial and temporal macrostructure of rainfall and the nonlinearity of the employed $R - k$ relation (part of issue (3)), power resolution (issue (5)), temporal sampling strategy (issue (6)), wet antenna attenuation, and correction thereof (issue (4)) on microwave link performance. For this purpose a relation between rainfall intensity and wet antenna attenuation has been proposed in Chapter 6. This relation is based on the assumption that there is a perfectly flat layer of water on the antenna. The thickness of this water layer is assumed to be related to the rainfall intensity through a power law, which has been calibrated using the 27-GHz microwave link and rain gauge data that were used in Chapter 3. If wet antenna attenuation is not included in the simulated link signals, effects of a limited power resolution (i.e. 1 dB) dominate at low frequencies and for short links (i.e. small path-integrated attenuations). For longer links and at higher frequencies, the effect of nonlinearity in the $R - k$ relation becomes more important. Of the two temporal sampling strategies encountered in commercial cellular communication network monitoring, the strategy in which the link signals are averaged over 15 minutes is to be preferred over instantaneous values recorded once every 15 minutes, which results in much larger uncertainties. When quasi-continuous sampling is available, this should of course be preferred.

Wet antenna attenuation is seen to cause dramatic errors. Hence, correction for this phenomenon is necessary. If such a correction is applied, errors and uncertainties are acceptable. However, there is a systematic underestimation of path-averaged rainfall intensities caused by differences between the path-averaged rainfall intensity and the local rainfall intensities at the antennas and the highly nonlinear relation between rainfall intensity and wet antenna attenuation. The dependence of this bias on the link length depends on the temporal sampling strategy because of the increased probability of the removal of dry weather when temporal averaging is applied. In the case of wet antenna attenuation the effect of the power resolution is still present, but less severe as the total attenuation is greater than without wet antenna attenuation. The frequency at which the errors and uncertainties are at a minimum is slightly higher than the frequency where the $R - k$ relation is linear, because the optimum (i.e. maximum) ratio of the total path-integrated attenuation and wet antenna attenuation occurs at a higher frequency.

7.2 Perspectives

Several future research lines can be defined based on the issues raised in this thesis. The most obvious next step would be to set up an experiment with a microwave link to actually measure both water fluxes within one experiment. The instrument that is to be used in this experiment could be manufactured according to the recommendations on frequency and polarization (combinations) given in Chapter 5, and should preferably be a dual-frequency and dual-polarization link. The availability of such an instrument would make experiments with artificial wetting of antennas possible. The results of these experiments could greatly increase the accuracy of rainfall estimated using research links as well as links from commercial cellular communication networks. In such an experimental setting, it is also possible to investigate whether wind-induced vibrations of the link antennas can be corrected for using entire power spectra of the signal rather than only variances.

Results from experiments with a microwave link in different climatological regions can be used to test the dependence of performance on the region where it is applied. The effect of the climatological variation of the micro- and macrostructure of rainfall will become more apparent. But more importantly, the performace of a microwave link for the estimation of evaporation can be evaluated under drier conditions in this way.

The use of a combination of an optical and a microwave link has been shown by *Meijninger et al.* (2002a) to be highly suitable for the estimation of evaporation. Using such a combination means that point meaurements of the spatially variable total available energy are no longer necessary, which make the results of this method more representative of the spatially averaged evaporation than the results from using stand-alone microwave links. This combination of optical and microwave links could also be of interest for the estimation of rainfall (or other types of precipitation). However, as optical wavelengths are much more sensitive to rain-induced attenuation, the lengths of these optical links are limited if the signal is not to be lost in (heavy) rainfall.

Errors and uncertainties in microwave link estimates of evaporation due to e.g. signal noise could be studied in a simulation framework such as used for rainfall in Chapter 6. This requires data sets of measured evaporation, net radiation, ground heat flux, and wind velocity, in combination with information on land use. These analyses could yield important information regarding the applicability under dry conditions, and more accurate estimations of uncertainties can be given (not solely based on errors in the total available energy, as in Chapter 2).

As mentioned in Chapter 1, the only type of precipitation considered in this thesis is rainfall. However, in large parts of the world, frozen precipitation constitutes an important part of the total precipitation. Therefore, it is important to derive relations between the vertical water flux associated with these types of precipitation and the attenuation of the microwave signal at different frequencies and polarizations, and to assess the quality of microwave link estimation of these types of precipitation.

Cellular communication networks are very dense (i.e. 12,000 links with an avarage length of 3–4 km over a 35,000 km^2 area in The Netherlands), especially in urban areas (see Chapter 4). Therefore it is feasible to construct maps of rainfall intensity using tomographic reconstruction techniques (see e.g. *Giuli et al.*, 1999; *Messer et al.*, 2006), which could then be verified using operational weather radar data. Depending on the density of the grid on which the rainfall maps are made, this tomographic reconstruction could help reduce uncertainties in individual link measurements. If no radar or rain gauge data are available, such as in large parts of Africa, these maps can provide the rainfall measurements needed for many applications such as water management and climate modelling. They can also provide the necessary "ground truth" used for validation of satellite precipitation missions such as the Tropical Rainfall Measuring Mission (TRMM) and the planned Global Precipitation Measurement (GPM) mission. Another interesting application of these dense networks would be to integrate link measurements with operational weather radar data in a data assimilation framework.

If it is possible to construct maps of rainfall intensities using cellular communication networks, it should in principle be possible to do the same for evaporation. This requires that not the absolute signal level is recorded but the variance, which should be computed based on a signal that is sampled with a high enough frequency to capture the largest part of the inertial subrange (i.e. > 10 Hz). As this variance is not a standard product of the monitoring packages employed by cellular communication companies, measurement of evaporation would require considerably more effort on the part of these companies than measurement of rainfall would.

The use of dual- frequency and/or dual polarization links for rainfall estimation has only been considered in a single-parameter (k or Δk) rainfall estimation framework. The use of multi-parameter rainfall estimation (which is used in e.g. polarimetric radar rainfall estimation, see e.g. *Bringi and Chandrasekar*, 2001), such as using values of k measured at different frequencies and/or polarizations, could have advantages such as reduction of errors due to e.g. signal drift or wet antenna attenuation. This could be investigated theoretically, using simulation, and using actual dual-frequency/polarization microwave link measurements.

Weckwerth et al. (2005) showed that spatially distributed measurements of water vapor content improve short-term forecasts of convective events. Besides the measurement of evaporation and precipitation, microwave links could also be used to measure this variable. *Fabry* (2004) has demonstrated that this is possible with radars using phase changes in the signal from ground reflections. Microwave links could be used to estimate path-integrated water vapor based on both amplitude and phase changes of the link signal. Forecasts of convective events may become much better if these measurements would also be possible using commercial cellular communication links, especially if radar refractivity data are also available.

APPENDIX A

Corrections applied to SOLIDAR radar data

This appendix deals with the corrections that are applied to the radar data used in Chapter 6 before they can be converted to rainfall intensities. This conversion of radar reflectivities is done using a power-law relation (see e.g. *Marshall and Palmer*, 1948). The coefficient and exponent of this power law have been calculated based on drop size data measured by *Wessels* (1972) over more than one year in De Bilt, The Netherlands and Mie series expansions (*van de Hulst*, 1957) for backscattering of spherical particles, using the expression for the refractive index of water given by *Liebe et al.* (1991). The resulting relation is

$$Z = 171R^{1.73}. \tag{A.1}$$

This relation has been obtained through non-linear regression of R on Z.

A.1 Attenuation

The X-band radar data is affected by attenuation due to both rainfall in the radar signal path and wetting of the transmitting and receiving radar antennas. Correction for the latter type of attenuation is not possible as this requires detailed knowledge of the behavior of the SOLIDAR antennas in rain. Attenuation due to rain in the path of the radar beam is corrected using the *Hitschfeld and Bordan* (1954) scheme. The relation between Z and the specific attenuation k (dB km^{-1}) used in this scheme was derived in the same way as the $Z - R$ relation (see Eq. (A.1)), yielding

$$Z = 9.25 \times 10^4 k^{1.25}. \tag{A.2}$$

Because of the inherent instability of this scheme, we have applied it only to a maximum correction level. For X-band radars, *Delrieu et al.* (1999) suggested a value of 10 dB (i.e., a factor of 10).

A.2 Clutter

Clutter from buildings is abundant in the map of radar reflectivities (see also Figure 6.1). This clutter is avoided as much as possible as correction for this phenomenon would alter the spatial structure of analyzed rain events. Therefore, one radial (containing 128 range bins) of the total radar picture has been selected based on the azimuth that is least affected by clutter. This is the radial between 216.6° and 218.4° (i.e., the 20th radial in the radar map counting clockwise from south as indicated by the line in Figure 6.1). Only range bins 9 through 92 (i.e., between 0.96 km and 11.04 km from the radar) are then used to exclude near-field problems close to the radar and clutter areas far away from the radar. However, the entire radial is used to correct for attenuation (see Section A.1), and it is assumed that near-field problems do not play significant roles.

Several range bins are still affected by clutter in the selected radial. The intensities of the clutter in these bins vary with time (both in dry weather and in rain), but are small enough to assume that their effect on attenuation correction (see Section A.1) is negligible. This clutter mostly affects the areas in which there is no rain, but for low rainfall intensity, rainy areas are also affected. Correction for this is carried out using the following considerations:

1. Over long periods of time, rainfall accumulations should be independent of the location in space (if the climatology in the area considered is constant and if high-intensity storms are excluded).

   In order to meet this criterium, a base level for each range bin is subtracted from the attenuation-corrected Z. For this purpose, a mean level is determined by computing the time average of Z for each separate range cell, where only those Z-values are considered where $R < 5$ mm h^{-1} (i.e., high-intensity storms are excluded). The effects of changing this condition to e.g. $R < 10$ mm h^{-1} are negligible. The range-minimum of these means is assumed to be indicative of the mean Z when no clutter is present. Subtracting this minimum from this range profile of means will hence yield the base level as a function of range, thought to represent range dependence resulting from non-meteorological targets. The resulting base level is shown as a function of range in Figure 6.2.

2. There is spatial coherence in rain. Therefore, rain cells (defined as closed areas in space where $R > 0$ mm h^{-1}) should have a minimum spatial extent, exceedind the size of individual radar range pixels.

   As the radar data under consideration is given in dBZ, no dry areas exist, although the minimum recorded dBZ level could be interpreted as

dry weather. However, this interpretation would yield erroneous results because of the clutter present in the radar data. Therefore, to generate intermittency in the rainfall fields, dry weather (i.e., $R = 0$ mm h^{-1}) areas are generated using the criterium that a rain cell must have a size of at least 3 range bins (i.e., 360 m) and 2 azimuth bins (i.e., between 67 m and 719 m for the range bins under consideration), of which each should have a Z value that is above a threshold corresponding to 0.5 mm h^{-1}. This threshold of $Z = 51.4$ mm^6 m^{-3} was selected based on visual inspection of resulting rainfall fields. The minimum extent of rain cells in the azimuth direction of 2 bins was chosen so that the minimum spatial extent in the far range is limited. The minimum number of 3 range bins corresponds approximately to the average of the minimum spatial extent in the azimuth direction. For this processing step, it is necessary that the two neighboring radials of the radial under consideration have also undergone the processing steps described above.

3. Over long periods of time, the zero-rainfall probability should be independent of the location in space.

   The number of zero-rain range bins is made approximately independent of the distance from the radar. This is done by finding a no-rain (higher than or equal to the $Z = 51.4$ mm^6 m^{-3} used above) threshold that is different for each of the range bins. All Z values below these thresholds for the correcponding range cells are set to 0 so that the total number of time intervals with zero-rain is independent of range.

The effect of these correction steps is shown in Figure 6.2, where uncorrected and corrected range profiles are shown in two events. It can be seen that for high rainfall intensities (event on 8 September, 1993), the effect of the corrections is negligible. For this event, the Z-values of the base level are so small that they are indistinguishable from the s_{r}-axis. For low-intensity rainfall (event on 15 May, 1993), the effect is visible, but still small. However, the important aspect of the corrections can be seen in this particular graph for the ranges $s_{\mathrm{r}} < 2$ km and $s_{\mathrm{r}} > 10$ km, where the corrected signal is set to zero.

A.3   Extension of events in time

One of the purposes of Chapter 6 is to investigate the effects of microwave link sampling stratieges, which typically operate on a 15-minute basis (see *Messer et al.*, 2006, and Chapter 4). Therefore the 332 rainfall events are extended to the nearest quarter of an hour by adding zeroes in both directions in time. This is based on the assumption that there is no rain before or after an event, which is justified by the fact that if there would have been rain in this period, radar data would have been stored as part of the event (see Section 6.2.1). This extension of the events with zeroes is done because if 15-minute intervals are taken from the beginning of the event, and not from the nearest quarter of an

hour on the clock, results may be biased in the sense that a sampling period would always start with the onset of rain.

APPENDIX B

Relations between R and A_a

The attenuation caused by a layer of water on a layer of material constituting the antenna cover is computed using (e.g. *Lorrain et al.*, 1988; *Reitz et al.*, 1993)

$$A_a = 10 \log_{10} \left(\left| \frac{x_1 + x_2 + x_3 + x_4}{2 m_{H_2O} \left(y_1 + y_2 \right)} \right|^2 \right), \tag{B.1}$$

with

$$x_1 = \left(m_{air} + m_{H_2O} \right) \left(m_{H_2O} + m_a \right) \times \tag{B.2}$$
$$\left(m_a + m_{air} \right) e^{-j \frac{2 \pi f}{c_1} \left(m_a l_a + m_{H_2O} l \right)}$$

$$x_2 = \left(m_{air} - m_{H_2O} \right) \left(m_{H_2O} - m_a \right) \times \tag{B.3}$$
$$\left(m_a + m_{air} \right) e^{-j \frac{2 \pi f}{c_1} \left(m_a l_a - m_{H_2O} l \right)}$$

$$x_3 = \left(m_{air} + m_{H_2O} \right) \left(m_{H_2O} - m_a \right) \times \tag{B.4}$$
$$\left(m_a - m_{air} \right) e^{j \frac{2 \pi f}{c_1} \left(m_a l_a - m_{H_2O} l \right)}$$

$$x_4 = \left(m_{air} - m_{H_2O} \right) \left(m_{H_2O} + m_a \right) \times \tag{B.5}$$
$$\left(m_a - m_{air} \right) e^{j \frac{2 \pi f}{c_1} \left(m_a l_a + m_{H_2O} l \right)}$$

and

$$y_1 = \left(m_{air} + m_a \right)^2 e^{-j \frac{2 \pi f}{c_1} m_a l_a} \tag{B.6}$$

$$y_2 = - \left(m_{air} - m_a \right)^2 e^{j \frac{2 \pi f}{c_1} m_a l_a}. \tag{B.7}$$

The complex refractive index of water m_{H_2O} is well-known as a function of frequency as given by *Liebe et al.* (1991). The refractive index and thickness of

123

the antenna cover material m_a and l_a, respectively, are assumed to have values of $1.73 + 0.014j$ (i.e., $m_\mathrm{a}^2 = 3.0 + 0.05j$) and 1.0 mm. The velocity of light in vacuum is $c_\mathrm{l} = 2.99 \times 10^8$ m s^{-1} and refractive index of air m_air is 1. Here, $j = \sqrt{-1}$.

Bibliography

Andreas, E. L. (1988), Estimating C_n^2 over snow and sea ice from meteorological data, *J. Opt. Soc. Am.*, *5A*, 481–495.

Andreas, E. L. (1989), Two-wavelength method of measuring path-averaged turbulent surface heat fluxes, *J. Atmos. Oceanic Technol.*, *6*, 280–292.

Andreas, E. L. (2000), Obtaining surface momentum and sensible heat fluxes from crosswind scintillometers, *J. Atmos. Oceanic Technol.*, *17*(1), 3–16.

van Asch, Th. W. J., J. Buma, and L. P. H. van Beek (1999), A view on some hydrological triggering systems in landslides, *Geomorphology*, *30*, 25–32.

Atlas, D. (1964), Advances in radar meteorology, *Adv. Geosci.*, *10*, 317–478.

Atlas, D., and C. W. Ulbrich (1977), Path- and area-integrated rainfall measurement by microwave attenuation in the 1–3 cm band, *J. Appl. Meteorol.*, *16*, 1322–1331.

Bastiaanssen, W. G. M. (2000), SEBAL-based sensible and latent heat fluxes in the irrigated Gediz basin, Turkey, *J. Hydrol.*, *229*, 87–100.

Bastiaanssen, W. G. M., M. U. D. Ahmad, and Y. Chemin (2002), Satellite surveillance of evaporative depletion across the Indus Basin, *Water Resour. Res.*, *38*(12), doi:10.1029/2001WR000386.

Battan, L. J. (1973), *Radar Observation of the Atmosphere*, University of Chicago Press, 324 pp.

Beard, K. V. (1976), Terminal velocity and shape of cloud and precipitation drops aloft, *J. Atmos. Sci.*, *33*, 851–864.

Berne, A., and R. Uijlenhoet (2005), A stochastic model of range profiles of raindrop size distributions: application to radar attenuation correction, *Geophys. Res. Lett.*, *32*(10), L10803, doi:10.1029/2004GL021899.

Berne, A., and R. Uijlenhoet (2007), Path-averaged rainfall estimation using microwave links: Uncertainty due to spatial rainfall variability, *Geophys. Res. Lett.*, *34*, L07403, doi:10.1029/2007GL029409.

Berne, A., G. Delrieu, H. Andrieu, and J.-D. Creutin (2004a), Influence of the vertical profile of reflectivity on radar-estimated rain rates at short time steps, *J. Hydrometeorol.*, *5*(2), 296–310.

Berne, A., G. Delrieu, J.-D. Creutin, and C. Obled (2004b), Temporal and spatial resolution of rainfall measurements required for urban hydrology, *J. Hydrol.*, *299*, 166–179.

Betts, A. K., J. H. Ball, A. C. M. Beljaars, M. J. Miller, and P. A. Viterbo (1996), The land surface-atmosphere interaction: A review based on observational and global modeling perspectives, *J. Geophys. Res.-Atmos.*, *101*(D3), 7209–7225.

Beven, K., and A. Binley (1992), The future of distributed models–model calibration and uncertainty prediction, *Hydrol. Process.*, *6*(3), 279–298.

Bonan, G. B., D. Pollard, and S. L. Thompson (1992), Effects of boreal forest vegetation on global climate, *Nature*, *359*, 716–718.

Bringi, V. N., and V. Chandrasekar (2001), *Polarimetric Doppler Weather Radar: Principles and Applications*, Cambridge University Press.

de Bruin, H. A. R. (2002), Introduction: Renaissance of scintillometry, *Bound.-Lay. Meteorol.*, *105*, 1–4.

Brutsaert, W. (1982), *Evaporation into the Atmosphere*, D. Reidel Publishing Company, 299 pp.

Brutsaert, W. (2005), *Hydrology. An Introduction*, Cambridge University Press, 605 pp.

Businger, J. A., J. C. Wyngaard, Y. Izumi, and E. F. Bradley (1971), Flux-profile relationships in the atmospheric surface layer, *J. Atmos. Sci.*, *28*, 181–189.

Callen, H. B. (1985), *Thermodynamics and an Introduction to Thermostatistics*, 2nd ed., J. Wiley & Sons, Inc., 493 pp.

Chuang, C. C., and K. V. Beard (1990), A numerical model for the equilibrium shape of raindrops, *J. Atmos. Sci.*, *47*(11), 1374–1389.

Crane, R. K. (1971), Propagation phenomena affecting satellite communication systems operating in the centimeter and millimeter wavelength bands, *Proc. IEEE*, *59*, 173–188.

Crewell, S., H. Bloemink, A. Feijt, S. G. García, D. Jolivet, O. A. Krasnov, A. van Lammeren, U. Löhnert, E. van Meijgaard, J. Meywerk, M. Quante, K. Pfeilsticker, S. Schmidt, T. Scholl, C. Simmer, M. Schröder, T. Trautmann, V. Venema, M. Wendisch, and U. Willén (2004), The Baltex bridge campaign: An integrated approach for a better understanding of clouds, *Bull. Am. Meteorol. Soc.*, *85*(10), 1565–1584.

Czekala, H., S. Havemann, K. Schmidt, T. Rother, and C. Simmer (1999), Comparison of microwave radiative transfer calculations obtained with three different approximations of hydrometeor shape, *J. Quant. Spectrosc. Radiat. Transfer*, *63*, 545–558.

Dagan, G. (1984), Solute transport in heterogeneous porous formations, *J. Fluid Mech.*, *145*, 151–177.

Delrieu, G., J.-D. Creutin, and I. Saint-André (1991), Mean $K-R$ relationships: Practical results for typical weather radar wavelengths, *J. Atmos. Oceanic Technol.*, *8*, 467–476.

Delrieu, G., L. Hucke, and J.-D. Creutin (1999), Attenuation in rain for X- and C-band weather radar systems: sensitivity with respect to the drop size distribution, *J. Appl. Meteorol.*, *38*(1), 57–68.

Delrieu, G., V. Ducrocq, E. Gaume, J. Nicol, O. Payrastre, E. Yates, H. Andrieu, P.-A. Ayral, C. Bouvier, J.-D. Creutin, M. Livet, S. Anquetin, M. Lang, L. Neppel, C. Obled, J. Parent-du-Châtelet, G.-M. Saulnier, A. Walpersdorf, and A. Wobrock (2005), The catastrophic flash-flood event of 8-9 September 2002 in the Gard region, France: a first case study for the Cévennes-Vivarais Mediterranean Hydro-meteorological Observatory, *J. Hydrometeorol.*, *6*(1), 34–52.

Entekhabi, D., G. R. Asrar, A. K. Betts, K. J. Beven, R. L. Bras, C. J. Duffy, T. Dunne, R. D. Koster, D. P. Lettenmaier, D. B. McLaughlin, W. J. Shuttleworth, M. T. van Genuchten, M.-Y. Wei, and E. F. Wood (1999), An agenda for land surface hydrology research and a call for the second international hydrological decade, *Bull. Am. Meteorol. Soc.*, *80*(10), 2043–2058.

Fabry, F. (2004), Meteorological value of ground target measurement by radar, *J. Atmos. Oceanic Technol.*, *21*(4), 560–573.

Giuli, D., A. Toccafondi, G. Biffi Gentili, and A. Freni (1991), Tomographic reconstruction of rainfall fields through microwave attenuation measurements, *J. Appl. Meteorol.*, *30*, 1323–1340.

Giuli, D., L. Facheris, and S. Tanelli (1999), Microwave tomographic inversion technique based on stochastic approach for rainfall fields monitoring, *IEEE Trans. Geosci. Remote Sens.*, *37*(5), 2536–2555.

Green, A. E., S. R. Green, M. S. Astill, and H. W. Caspari (2000), Estimating latent heat flux from a vineyard using scintillometry, *Terr. Atmos. Oceanic Sci.*, *11*(2), 525–542.

Green, A. E., M. S. Astill, K. J. McAneney, and J. P. Nieveen (2001), Path-averaged surface fluxes determined from infrared and microwave scintillometry, *Agric. Forest Meteorol.*, *109*, 233–247.

Grum, M., S. Krämer, H.-R. Verworn, and A. Redder (2005), Combined use of point rain gauges, radar, microwave link and level measurements in urban hydrological modelling, *Atmos. Res.*, *77*, 313–321.

Hendrantoro, G., and I. Zawadzki (2003), Derivation of parameters of $Y-Z$ power-law relation from raindrop size distribution measurements and its application in the calculation of rain attenuation from radar reflectivity factor measurements, *IEEE Trans. Anten. Propag.*, *51*(1), 12–22.

Herben, M. H. A. J. (1984), The influence of tropospheric irregularities on the dynamic behaviour of microwave radio systems, Ph.D. thesis, Technische Hogeschool Eindhoven.

Hill, R. J., and S. F. Clifford (1981), Contribution of water vapor monomer resonances to fluctuations of refraction and absorption for submillimeter through centimeter wavelengths, *Radio Sci.*, *16*(1), 77–82.

Hill, R. J., S. F. Clifford, and R. S. Lawrence (1980), Refractive-index and absorption fluctuations in the infrared caused by temperature, humidity and pressure fluctuations, *J. Opt. Soc. Am.*, *70*(10), 1192–1205.

Hill, R. J., R. A. Bohlander, S. F. Clifford, R. W. McMillan, J. T. Priestley, and W. P. Schoenfeld (1988), Turbulence-induced millimeter-wave scintillation compared with micrometeorological measurements, *IEEE Trans. Geosci. Remote Sens.*, *26*(3), 330–342.

Hitschfeld, W., and J. Bordan (1954), Errors inherent in the radar measurement of rainfall at attenuating wavelengths, *J. Meteorol.*, *11*, 58–67.

Hogg, D. C. (1968), Millimeter-wave communication through the atmosphere, *Science*, *159*(3810), 39–46.

Holt, A. R., G. G. Kuznetsov, and A. R. Rahimi (2003), Comparison of the use of dual-frequency and single-frequency attenuation for the measurement of rainfall along a microwave link, *IEE Proc.-Microw. Anten. Propag.*, *150*(5), 315–320.

Horst, T. W. (1999), The footprint for estimation of atmosphere-surface exchange fluxes by profile techniques, *Bound.-Lay. Meteorol.*, *90*, 171–188.

Horst, T. W., and J. C. Weil (1992), Footprint estimation for scalar flux measurements in the atmospheric surface layer, *Bound.-Lay. Meteorol.*, *59*, 279–296.

Horst, T. W., and J. C. Weil (1994), How far is far enough?: The fetch requirements for micrometeorological measurement of surface fluxes, *J. Atmos. Oceanic Technol.*, *11*, 1018–1025.

Howard, A. D., W. E. Dietrich, and M. A. Seidl (1994), Modeling fluvial erosion on regional to continental scales, *J. Geophys. Res.-Solid Earth*, *99*(B7), 13,971–13,986.

van de Hulst, H. C. (1957), *Light Scattering by Small Particles*, John Wiley & Sons, Inc., 470 pp.

Hupet, F., and M. Vanclooster (2004), Sampling strategies to estimate field areal evapotranspiration fluxes with a soil water balance approach, *J. Hydrol.*, *292*, 262–280.

Ibsen, M.-L., and N. Casagli (2004), Rainfall patterns and related landslide incidence in the Porretta-Vergato region, Italy, *Landslides*, *1*(2), 143–150.

Idso, S. B., J. K. Aase, and R. D. Jackson (1975), Net radiation - soil heat flux relations as influenced by soil water content variations, *Bound.-Lay. Meteorol.*, *9*(1), 113–122.

Illingworth, A. J., and C. J. Stevens (1987), An optical disdrometer for the measurement of raindrop size spectra in windy conditions, *J. Atmos. Oceanic Technol.*, *4*(3), 411–421.

ITU-R P.838-3 (2005), Specific attenuation model for rain for use in pre-

diction methods, *Tech. rep.*, International Telecommunication Union–Radiocommunication Recommendations.

Jameson, A. R. (1991), A comparison of microwave techniques for measuring rainfall, *J. Appl. Meteorol.*, *30*, 32–54.

Jameson, A. R., and A. B. Kostinski (2002), When is rain steady?, *J. Appl. Meteorol.*, *41*, 83–90.

Joss, J., and A. Waldvogel (1967), Ein Spectrograph für Niederschlagstropfen mit automatischer Auswertung, *Pure Appl. Geophys.*, *69*, 240–246.

Joss, J., J. C. Thams, and A. Waldvogel (1968), The variation of raindrop size distributions at Locarno, in *Proceedings of the International Conference on Cloud Physics*, pp. 369–373.

Katul, G. G., S. M. Goltz, C.-I. Hsieh, Y. Cheng, F. Mowry, and J. Sigmon (1995), Estimation of surface heat and momentum fluxes using the flux-variance method above uniform and non-uniform terrain, *Bound.-Lay. Meteorol.*, *74*, 237–260.

Kharadly, M. M. Z., and R. Ross (2001), Effect of wet antenna attenuation on propagation data statistics, *IEEE Trans. Anten. Propag.*, *49*(8), 1183–1191.

Kirchner, J. W. (2006), Getting the right answers for the right reasons: Linking maesurements, analyses, and models to advance the science of hydrology, *Water Resour. Res.*, *42*, W03S04, doi:10.1029/2005WR004362.

Kochendorfer, J. P., and J. A. Ramírez (2005), The impact of land surface-atmosphere interactions on the temporal variability of soil moisture at the regional scale, *J. Hydrometeorol.*, *6*, 53–67.

Kohsiek, W., and M. H. A. J. Herben (1983), Evaporation derived from optical and radio-wave scintillation, *Appl. Opt.*, *22*(17), 2566–2570.

Krämer, S., H.-R. Verworn, and A. Redder (2005), Improvement of X-band radar rainfall estimates using a microwave link, *Atmos. Res.*, *77*, 278–299.

Kursinski, A. L., and X. Zeng (2006), Areal estimation of intensity and frequency of summertime precipitation over a midlattitude region, *Geophys. Res. Lett.*, *33*, L22401, doi:10.1029/2006GL027393.

van Lanen, H. A. J., M. Fendeková, A. Kasprzyk, and W. Pokosjki (2004), Flow generating processes, in *Hydrological Drought. Processes and Estimation Methods for Streamflow and Groundwater*, *Developments In Water Science*, vol. 48, edited by L. M. Tallaksen and H. A. J. van Lanen, pp. 53–96, Elsevier Science, B.V.

Laws, J. O., and D. A. Parsons (1943), The relation of raindrop-size to intensity, *Trans. AGU*, *24*, 452–460.

Leijnse, H., J. A. Smith, and M. L. Baeck (2002), The use of radar rainfall estimates for hydrologic modelling of flood response in urban drainage basins, in *Proceedings of the XIV*[th] *International Conference on Computational Methods in Water Resources*, vol. 2, edited by S. M. Hassanizadeh, R. J. Schotting, W. G. Gray, and G. F. Pinder, pp. 1371–1378.

Liebe, H. J., G. A. Hufford, and T. Manabe (1991), A model for the com-

plex permittivity of water at frequencies below 1 THz, *Internat. J. Infrared Mm. Waves*, *12*(7), 659–675.

Ligthart, L. P., and L. R. Nieuwkerk (1990), An X-band solid-state FM-CW weather radar, *IEE Proc.-F Radar Signal Proces.*, *137*(6), 418–426.

Lorrain, P., D. R. Corson, and F. Lorrain (1988), *Electromagnetic Fields and Waves*, 3$^{\mathrm{rd}}$ ed., W. H. Freeman and Company.

Manabe, S., and K. Bryan (1969), Climate calculations with a combined ocean-atmosphere model, *J. Atmos. Sci.*, *26*, 786–789.

Marshall, J. S., and W. M. Palmer (1948), The distribution of raindrops with size, *J. Meteorol.*, *5*, 165–166.

Marshall, J. S., W. Hitschfeld, and K. L. S. Gunn (1955), Advances in radar weather, *Adv. Geophys.*, *2*, 1–56.

McMillan, R. W., R. A. Bohlander, G. R. Ochs, R. J. Hill, and S. F. Clifford (1983), Millimeter wave atmospheric turbulence measurements: preliminary results and instrumentation for future measurements, *Opt. Eng.*, *22*(1), 32–39.

Meijninger, W. M. L., and H. A. R. de Bruin (2000), Sensible heat fluxes over irrigated areas in western Turkey determined with a large aperture scintillometer, *J. Hydrol.*, *229*, 42–49.

Meijninger, W. M. L., A. E. Green, O. K. Hartogensis, W. Kohsiek, J. C. B. Hoedjes, R. M. Zuurbier, and H. A. R. de Bruin (2002a), Determination of area-averaged water vapour fluxes with large aperture and radio wave scintillometers over a heterogeneous surface – Flevoland field experiment, *Bound.-Lay. Meteorol.*, *105*, 63–83.

Meijninger, W. M. L., O. K. Hartogensis, W. Kohsiek, J. C. B. Hoedjes, R. M. Zuurbier, and H. A. R. de Bruin (2002b), Determination of area-averaged sensible heat with a large aperture scintillometer over a heterogeneous surface – Flevoland field experiment, *Bound.-Lay. Meteorol.*, *105*, 37–62.

Meneghini, R., T. Kozu, H. Kumagai, and W. C. Boncyk (1992), A study of rain estimation methods from space using dual-wavelength radar measurements at near-nadir incidence over ocean, *J. Atmos. Oceanic Technol.*, *9*, 364–382.

Mengelkamp, H.-T., F. Beyrich, G. Heinemann, F. Ament, J. Bange, F. Berger, J. Bösenberg, T. Foken, B. Hennemuth, C. Heret, S. Huneke, K.-P. Johnsen, M. Kerschgens, W. Kohsiek, J.-P. Leps, C. Liebethal, H. Lohse, M. Mauder, W. Meijninger, S. Raasch, C. Simmer, T. Spieß, A. Tittebrand, J. Uhlenbrock, and P. Zittel (2006), Evaporation over a heterogeneous land surface, *Bull. Am. Meteorol. Soc.*, *87*(6), 775–786.

Messer, H. A., A. Zinevich, and P. Alpert (2006), Environmental monitoring by wireless communication networks, *Science*, *312*, 713.

Milly, P. C. D., R. T. Weatherald, K. A. Dunne, and T. L. Delworth (2002), Increasing risk of great floods in a changing climate, *Nature*, *415*, 514–517.

Minda, H., and K. Nakamura (2005), High temporal resolution path-average

raingauge with 50-GHz band microwave, *J. Atmos. Oceanic Technol.*, *22*, 165–179.

Mishchenko, M. I. (2000), Calculation of the amplitude matrix for a nonspherical particle in a fixed orientation, *Appl. Opt.*, *39*(6), 1026–1031.

Mishchenko, M. I., and L. D. Travis (1994), T-matrix computations of light scattering by large spheroidal particles, *Opt. Commun.*, *109*, 16–21.

Mishchenko, M. I., L. D. Travis, and D. W. Mackowski (1996), T-matrix computations of light scattering by nonspherical particles: a review, *J. Quant. Spectrosc. Radiat. Transfer*, *55*(5), 535–575.

Oki, T., and S. Kanae (2006), Global hydrological cycles and world water resources, *Science*, *313*, 1068–1072.

Olsen, R. L., D. V. Rogers, and D. B. Hodge (1978), The aR^b relation in the calculation of rain attenuation, *IEEE Trans. Anten. Propag.*, *AP-26*(2), 318–329.

Parlange, M. B., W. E. Eichinger, and J. D. Albertson (1995), Regional scale evaporation and the atmospheric boundary layer, *Rev. Geophys.*, *33*(1), 99–124.

Pope, S. B. (2000), *Turbulent Flows*, Cambridge University Press, 771 pp.

Postel, S. L., G. C. Daily, and P. R. Ehrlich (1996), Human appropriation of renewable fresh water, *Science*, *271*, 785–788.

Pruppacher, H. R., and J. D. Klett (1997), *Microphysics of Clouds and Precipitation*, 2nd ed., Kluwer Academic Publishers, 954 pp.

Rahimi, A. R., A. R. Holt, G. J. G. Upton, and R. J. Cummings (2003), The use of dual-frequency microwave links for measuring path-averaged rainfall, *J. Geophys. Res.-Atmos.*, *108*(D15), art. No. 4467.

Rahimi, A. R., G. J. G. Upton, and A. R. Holt (2004), Dual-frequency links–a complement to gauges and radar for the measurement of rain, *J. Hydrol.*, *288*, 3–12.

Reitz, J. R., F. J. Milford, and R. Christy (1993), *Foundations of Electromagnetic Theory*, 4th ed., Addison-Wesley Publishing Company.

Rincon, R. F., and R. H. Lang (2002), Microwave link dual-wavelength measurements of path-average attenuation for the estimation of drop size distributions and rainfall, *IEEE Trans. Geosci. Remote Sens.*, *40*(4), 760–770.

Ritchie, J. T., and E. Burnett (1971), Dryland evaporative flux in a subhumid climate: II. Plant influences, *Agronomy J.*, *63*, 56–62.

Ruf, C. S., K. Aydin, S. Mathur, and J. P. Bobak (1996), 35-GHz dual-polarization propagation link for rain-rate estimation, *J. Atmos. Oceanic Technol.*, *13*, 419–425.

Russchenberg, H. W. J. (1992), Ground-based remote sensing of precipitation using a multi-polarized FM-CW doppler radar, Ph.D. thesis, Delft University of Tecnology.

Salles, C., J.-D. Creutin, and D. Sempere-Torres (1998), The optical spectro-pluviometer revisited, *J. Atmos. Oceanic Technol.*, *15*(5), 1215–1222.

Schönhuber, M., H. Urban, J. P. V. Poiares Baptista, W. L. Randeu, and W. Riedler (1994), Measurements of precipitation characteristics by a new disdrometer, in *Proceedings of Atmosperic Physics and Dynamics in the Analysis and Prognosis of Precipitation Fields*, Rome, Italy.

Semplak, R. A., and R. H. Turrin (1969), Some measurements of attenuation by rainfall at 18.5 GHz, *Bell Syst. Technol. J.*, *48*, 1767–1787.

Sheppard, B. E. (1990), Measurement of raindrop size distributions using a small Doppler radar, *J. Atmos. Oceanic Technol.*, *7*(2), 255–268.

Shukla, J., and Y. Mintz (1982), Influence of land-surface evpotranspiration on the earth's climate, *Science*, *215*, 1498–1501.

Sieck, L. C., S. J. Burges, and M. Steiner (2007), Challenges in obtaining reliable measurements of point rainfall, *Water Resour. Res.*, *43*, W01,420, doi:10.1029/2005WR004519.

Simmer, C., V. Venema, M. Diederich, S. Crewell, A. Feijt, and J.-L. Brenguier (2004), The BALTEX-BRIDGE campaigns–a quest for continental cloud structures, in *Proceedings of the 14$^{\text{th}}$ Int. Conf. on Clouds and Precipitation*, Bologna, Italy.

Smith, J. A., and W. F. Krajewski (1993), A modeling study of rainfall rate–reflectivity relationships, *Water Resour. Res.*, *29*(8), 2505–2514.

Smith, J. A., M. L. Baeck, M. Steiner, and A. J. Miller (1996), Catastrophic rainfall from an upslope thunderstorm in the central Appalachians: The Rapidan storm of June 27, 1995, *Water Resour. Res.*, *32*(10), 3099–3114.

Smith, J. A., M. L. Baeck, Y. Zhang, and C. A. Doswell Jr. (2001), Extreme rainfall and flooding from supercell thunderstorms, *J. Hydrometeorol.*, *2*(4), 469–489.

Smith, J. A., M. L. Baeck, J. E. Morrison, P. Sturdevant-Rees, D. F. Turner-Gillespie, and P. D. Bates (2002), The regional hydrology of extreme floods in an urbanizing drainage basin, *J. Hydrometeorol.*, *3*(3), 267–282.

Stahl, K., and H. Hisdal (2004), Hydroclimatology, in *Hydrological Drought. Processes and Estimation Methods for Streamflow and Groundwater*, *Developments In Water Science*, vol. 48, edited by L. M. Tallaksen and H. A. J. van Lanen, pp. 19–51, Elsevier Science, B.V.

Steiner, M., T. L. Bell, Y. Zhang, and E. F. Wood (2003), Comparison of two methods for estimating the sampling-related uncertainty of satellite rainfall averages based on a large radar data set, *J. Clim.*, *16*, 3759–3778.

Su, Z. (2002), The Surface Energy Balance System (SEBS) for estimation of turbulent heat fluxes, *Hydrol. Earth Sys. Sci.*, *6*(1), 85–99.

Talebi, A., R. Uijlenhoet, and P. A. Troch (2007), Soil moisture storage and hillslope stability, *Nat. Hazards Earth Syst. Sci.*, *7*, 523–534.

Tatarskii, V. I. (1971), *The Effects of the Turbulent Atmosphere on Wave Propagation*, translated from Russian by Israel Program for Scientific Translations, 472 pp.

Testik, F. Y., and A. P. Barros (2007), Toward elucidating the mi-

crostructure of warm rainfall: A survey, *Rev. Geophys.*, *45*(2), RG2003, doi:10.1029/2005RG000182.

Teuling, A. J., S. I. Seneviratne, C. Williams, and P. A. Troch (2006a), Observed timescales of evapotranspiration response to soil moisture, *Geophys. Res. Lett.*, *33*(23), L23403, doi:10.1029/2006GL028178.

Teuling, A. J., R. Uijlenhoet, F. Hupet, and P. A. Troch (2006b), Impact of plant water uptake strategy on soil moisture and evapotranspiration dynamics during drydown, *Geophys. Res. Lett.*, *33*(3), L03401, doi:10.1029/2005GL025019.

Thurai, M., and V. N. Bringi (2005), Drop axis ratios from a 2D Video Disdrometer, *J. Atmos. Oceanic Technol.*, *22*, 966–978.

Tokay, A., P. G. Bashor, and K. R. Wolff (2005), Error characteristics of rainfall measurements by collocated Joss-Waldvogel disdrometers, *J. Atmos. Oceanic Technol.*, *22*, 513–527.

Uijlenhoet, R. (1999), Parameterization of rainfall microstructure for radar meteorology and hydrology, Ph.D. thesis, Wageningen University.

Uijlenhoet, R., and J. N. M. Stricker (1999), A consistent rainfall parameterization based on the exponential raindrop size distribution, *J. Hydrol.*, *218*, 101–127.

Uijlenhoet, R., H. Andrieu, G. Austin, E. Baltas, M. Borga, M. Brilly, I. Cluckie, J.-D. Creutin, G. Delrieu, P. Deshons, S. Fatorelli, R. P. Griffith, D. Han, M. Mimikou, M. Moani, J. Porrà, D. Sempere-Torres, and D. Spagni (1999), HYDROMET Integrated Radar Experiment (HIRE): experimental setup and first results, in *29*[th] *Int. Conf. on Radar Meteorology*, pp. 926–930, AMS, Montréal, Canada.

Uijlenhoet, R., M. Steiner, and J. A. Smith (2003), Variability of raindrop size distributions in a squall line and implications for radar rainfall estimation, *J. Hydrometeorol.*, *4*(1), 43–61.

Uijlenhoet, R., J. M. Porrà, D. Sempere Torres, and J.-D. Creutin (2006), Analytical solutions to sampling effects in drop size distribution measurements during stationary rainfall: Estimation of bulk rainfall variables, *J. Hydrol.*, *328*, 65–82.

Ulaby, F. T., R. K. Moore, and A. K. Fung (1981), *Microwave Remote Sensing: Active and Passive, Vol. I: Microwave Remote Sensing Fundamentals and Radiometry*, Addison-Wesley.

Upton, G. J. G., A. R. Holt, R. J. Cummings, A. R. Rahimi, and J. W. F. Goddard (2005), Microwave links: The future for urban rainfall measurement?, *Atmos. Res.*, *77*, 300–312.

Waterman, P. C. (1965), Matrix formulation of electromagnetic scattering, *Proc. IEEE*, *53*(8), 805.

Weckwerth, T. M., C. R. Pettet, F. Fabry, S. Park, M. A. LeMone, and J. W. Wilson (2005), Radar refractivity retrieval: Validation and application to short-term forecasting, *J. Appl. Meteorol.*, *44*, 285–300.

Wessels, H. R. A. (1972), Metingen van regendruppels in De Bilt, *Tech. Rep. W. R. 72-6*, R. Neth. Meteorol. Inst., De Bilt, 41 pp. (in Dutch).

Wieringa, J. (1992), Updating the Davenport roughness classification, *J. Wind Eng. Ind. Aerod.*, *41*, 357–368.

Wyngaard, J. C., Y. Izumi, and S. A. Collins, Jr. (1971), Behavior of the refractive-index-structure parameter near the ground, *J. Opt. Soc. Am.*, *61*(12), 1646–1650.

Samenvatting

Hoofdstuk 1. Dit proefschrift gaat over het schatten van verdamping en neerslag met een microgolf straalverbinding. Het meten van deze verticale fluxen van water aan het grensvlak tussen land en atmosfeer op een regionale schaal is van groot belang in disciplines als hydrologie en meteorologie. Omdat de schaal waarop microgolf straalverbindingen werken ongeveer dezelfde schaal is die van belang is voor vele toepassingen, hebben metingen van deze instrumenten een duidelijk voordeel boven punt-schaal metingen. Andere instrumenten hebben weer nadelen die ze minder nauwkeurig maken dan microgolf straalverbindingen. Maar omdat microgolf straalverbindingen zeker niet perfect zijn valt het meeste voordeel te halen als ze gebruikt worden in combinatie met andere instrumenten. Er schuilt veel potentie in het gebruik van microgolf straalverbindingen die deel uitmaken van de bestaande zeer dichte commerciële netwerken (die worden gebruikt voor mobiele telefonie), in het bijzonder voor het meten van regen. Daarom is onderzoek naar deze instrumenten zeer relevant.

Hoofdstuk 2. Er is een methode voorgesteld om verdamping te schatten op regionale schaal met een microgolf straalverbinding (radio golf scintillometer), waarbij als extra voorwaarde wordt gebruikt dat de energiebalans aan het aardoppervlak sluitend moet zijn. Deze "*Radio Wave Scintillometry-Energy Budget Method*" (RWS-EBM) methode is geëvalueerd op basis van de toepasbaarheid onder verschillende meteorologische omstandigheden, en de gevoeligheid voor fouten in verschillende variabelen (de structuur parameter van de brekingsindex van lucht C_n^2, de totale beschikbare energie $R_n - G$, de windsnelheid u, de effectieve gemiddelde gewashoogte h_0 en de correlatiecoefficient tussen temperatuurs- en luchtvochtigheidsfluctuaties r_{TQ}). Er is aangetoond dat de methode het beste geschikt is voor het schatten van verdamping onder relatief vochtige omstandigheden, waarbij de latente warmtestroom minimaal een derde is van de totale beschikbare energie (d.w.z. Bowen ratio ≤ 2). Het is belangrijk om de totale beschikbare energie en de windsnelheid redelijk precies te meten, omdat de gevoeligheid van de methode voor deze variabelen het

grootst is. Het Flevoland Experiment heeft de gegevens gegenereerd die zijn gebruikt voor het testen van de RWS-EBM methode. Deze gegevens zijn metingen met een 27-GHz microgolf straalverbinding (lengte 2.2 km), een optische "*Large Aperture*" Scintillometer (LAS, ook 2.2 km) en vier Eddy Covariantie (EC) systemen. Hierbij zijn 92 overdag gemeten waarden (meetinterval is 30 minuten) gebruikt. Bij vergelijking van verdamping geschat door de RWS-EBM methode met verdamping geschat met andere methodes (EC en twee-golflengte methode) blijkt dat de RWS-EBM methode consistente schattingen levert (coefficient van bepaling $r^2 = 0.85$ onder vochtige omstandigheden.

Hoofdstuk 3. De bruikbaarheid voor het schatten van pad-gemiddelde neerslag van dezelfde 27-GHz microgolf straalverbinding is ook onderzocht. Theoretiche analyses laten zien dat de uitdoving van het electromagnetische signaal bij deze frequentie bijna lineair varieert met de regenintensiteit, hetgeen ideaal is voor lijn-geïntegreerde metingen. Deze relatie is relatief ongevoelig voor variaties in de druppelgrootteverdeling en de temperatuur van de regen, waardoor onzekerheden in deze variabelen geen grote rol zullen spelen bij het schatten van neerslag bij deze frequentie. De gegevens van een experiment met dezelfde 27-GHz microgolf straalverbinding als hierboven (nu met een lengte van 4.89 km) en zeven regenmeters onder het pad van het signaal zijn gebruikt om te bepalen of dit instrument geschikt is voor het meten van pad-gemiddelde regen. Er is aangetoond dat het nat worden van de antennes van de straalverbinding van grote invloed is op de geschatte regenintensiteit. Maar als een correctiefunctie op basis van slechts twee parameters wordt toegepast, laten vergelijkingen met de regenmetergegevens zien dat een microgolf straalverbinding wel dezelijk geschikt is voor het meten van pad-gemiddelde regen.

Hoofdstuk 4. Op bijna alle continenten is er een zeer dicht netwerk van bestaande microgolf straalverbindingen. Deze straalverbindingen maken deel uit van commerciële communicatie netwerken (die worden gebruikt voor mobiele telefonie). Gegevens van twee van zulke straalverbindingen (beide 38 GHz) in de buurt van Wageningen, verzameld in zeven stratiforme buien en één convectieve bui in de periode oktober-november 2003 zijn geanalyseerd. Daarbij zijn de geschatte regenintensiteiten vergeleken met regenintensiteiten gemeten door een dichbij gelegen regenmeter, en door de twee operationele C-band radars van het KNMI. Er is aangetoond door deze analyse dat de dynamiek van de buien redelijk goed wordt weergegeven door de straalverbindingen, maar dat de accumulaties vaak worden overschat. Daaruit volgt dat deze commerciële microgolf straalverbindingen in potentie een zeer waardevolle aanvulling zouden kunnen zijn op bestaande methoden om regen te meten, mits de problemen met onzekerheid in het nulniveau van het signaal, afrondingsfouten door beperkte vermogensresolutie, natte antennes en zeer lange tijd tussen opeenvolgende metingen kunnen worden opgelost.

Hoofdstuk 5. Naast de uitdoving van één signaal kan ook het verschil in uitdoving van twee signalen met verschillende frequenties en/of polarisaties worden gebruikt voor het schatten van pad-gemiddelde neerslag. Machtsrelaties tussen regenintensiteit en specifieke of differentiële uitdoving zijn afgeleid met

136

behulp van gemeten druppelgrootteverdelingen. De optimale configuratie voor een microgolf straalverbinding met één frequentie is horizontaal gepolariseerd bij 35.9 GHz. De invloed van kantelingen van druppels is te verwaarlozen bij gebruik van specifieke uitdoving, en zeer klein (een paar procent) als differentiële uitdoving wordt gebruikt. Het effect van variaties in temperatuur is ook klein als de frequentie en/of combinatie van frequenties goed (d.w.z. niet te laag) is. Er is aangetoond dat de gebruikte machtsrelaties afgeleid zouden moeten zijn voor de locale klimatologie. Signalen van microgolf straalverbindingen zijn gesimuleerd op basis van tijdreeksen van gemeten druppelgrootteverdelingen in combinatie met metingen van de windsnelheid. Fouten en onzekerheden als gevolg van variatie in druppelgrootteverdelingen hebben een minimum bij de (combinatie van) frequenties waarbij de machtsrelaties bijna lineair zijn. Over het algemeen nemen fouten toe naarmate de straalverbindingen langer worden.

Hoofdstuk 6. Problemen met het schatten van regen met microgolf straalverbindingen, zoals de effecten van de variatie van regen in de ruimte en de tijd, de niet-lineariteit van de $R-k$ relaties, lange tijd tussen opeenvolgende metingen, beperkte vermogensresolutie en natte antennes zijn bestudeerd door gebruik te maken van meer dan anderhalf jaar aan hoge resolutie X-band radar gegevens. Met deze gegevens zijn signalen van microgolf straalverbindingen gesimuleerd voor verschillende frequenties en lengtes van de verbindingen. De geschatte regenintensiteiten kunnen op deze manier worden vergeleken met de "echte" pad-gemiddelde regenintensiteiten. Resultaten van deze analyses kunnen worden verklaard met behulp van afgeleide informatie over de ruimte-tijd structuur van de regen. Een frequentie-afhankelijke semi-empirische relatie tussen regenintensiteit en uitdoving veroorzaakt door natte antennes is afgeleid en gecalibreerd door het gebruik van gegevens van het hierboven beschreven experiment met de 27-GHz straalverbinding en de zeven regenmeters. Er is aangetoond dat, mits er een goede strategie voor het opslaan van metingen wordt gebruikt (niet instantaan elk kwartier), de effecten van beperkte vermogensresolutie en uitdoving door natte antennes (als er een correctie hiervoor wordt toegepast) beperkt zijn (d.w.z. absolute waarden van fouten en onzekerheden zijn kleiner dan 20%), voor straalverbindingen langer dan ~ 2 km en met frequenties hoger dan ~ 20 GHz.

Hoofdstuk 7. Er is aangetoond dat microgolf straalverbindingen zeer bruikbaar zijn voor het schatten van verdamping en neerslag. Een aantal problemen bij het schatten van deze groootheden zijn opgemerkt en vervolgens geanalyseerd. Commerciële microgolf straalverbindingen zijn potentieel zeer geschikt om op grote schaal zeer gedetailleerd deze fluxen, in het bijzonde regen, in kaart te brengen. Toekomstige studies zullen gericht zijn op o.a. het testen van microgolf straalverbindingen (met twee frequenties en polarisaties) onder verschillende klimatologische omstandigheden, het onderzoeken of commerciële straalverbindingen gebruikt kunnen worden voor het meten van verdamping, het integreren van gegevens van commerciële straalverbindingen en van operationele weerradar en het onderzoeken of microgolf straalverbindingen kunnen worden gebruikt om pad-gemiddelde luchtvochtigheid te meten.

Curriculum Vitae

Hidde Leijnse, 30 november 1977, Hoogmade

1990–1996
>   VWO, Werkplaats Kindergemeenschap, Kees Boekeschool, Bilthoven

1996–2003
>   Studie Technische Natuurkunde, Universiteit Twente, specialisatie Stromingsleer

2000
>   Studentassistentschap begeleiding natuurkundig practicum

2001–2002
>   Stage bij Water Resources Program, Princeton University, NJ, USA

2002–2003
>   Afstudeeronderzoek bij MARIN, Wageningen

2003–2007
>   Promotieonderzoek bij leerstoelgroep Hydrologie en Kwantitatief Waterbeheer, Wageningen Univesiteit

2007–heden
>   Postdoc hydrometeorologie, leerstoelgroep Hydrologie en Kwantitatief Waterbeheer, Wageningen Universiteit

december 2007
>   Diploma Netherlands Research School for the Socio-Economic and Natural Sciences of the Environment (SENSE), belangrijkste activiteiten:
>
>   deelname aan de cursus *Basic and Avanced Statistics* (Wageningen, 2003-2004)
>
>   deelname aan de cursus *Uncertainty modelling & analysis* (Wageningen, 2004)
>
>   organisatie van de *CAHMDA-II international workshop* (Princeton, 2004)
>
>   deelname aan de cursus *Climate and the hydrological cycle* (Utrecht, 2005)